



HAL
open science

Behaviour of physical vapor deposited nanocomposite coatings under extreme environments

Jingxian Wang

► **To cite this version:**

Jingxian Wang. Behaviour of physical vapor deposited nanocomposite coatings under extreme environments. Other. Université Grenoble Alpes; Nanyang Technological University (Singapour), 2017. English. NNT: 2017GREAI053 . tel-01691064

HAL Id: tel-01691064

<https://theses.hal.science/tel-01691064>

Submitted on 23 Jan 2018

HAL is a multi-disciplinary open access archive for the deposit and dissemination of scientific research documents, whether they are published or not. The documents may come from teaching and research institutions in France or abroad, or from public or private research centers.

L'archive ouverte pluridisciplinaire **HAL**, est destinée au dépôt et à la diffusion de documents scientifiques de niveau recherche, publiés ou non, émanant des établissements d'enseignement et de recherche français ou étrangers, des laboratoires publics ou privés.

THÈSE

Pour obtenir le grade de

**DOCTEUR DE LA COMMUNAUTE UNIVERSITE
GRENOBLE ALPES**

**préparée dans le cadre d'une cotutelle *entre la
Communauté Université Grenoble Alpes***

Spécialité : **MATERIAUX, MECANIQUE, GENIE CIVIL,
ELECTROCHIMIE**

Arrêté ministériel : le 6 janvier 2005 - 7 août 2006

et *Nanyang Technological University*

Présentée par

Jingxian WANG

Thèse dirigée par **Yves WOUTERS** et **ZhiLi DONG**
codirigée par **Céline PASCALE**, **Timothy WHITE** et **Erjia LIU**

préparée au sein des **Laboratoire SIMaP**
dans l'**École Doctorale I-MEP2** de Grenoble
et **Energy Research Institute @ NTU**
dans **Interdisciplinary Graduate School** de Singapour

Comportement de revêtements nanostructures déposés par PVD en condition environnementales sévères

Thèse soutenue publiquement le **18 janvier 2017**,
devant le jury composé de :

M. Lin LI

Professeur associé, Nanyang Technological University, Président

M. Michel PONS

Directeur de Recherche, CNRS SIMaP, Examineur

M. Alex Qingyu YAN

Professeur associé, Nanyang Technological University, Examineur

M. Tupei CHEN

Professeur associé, Nanyang Technological University, Examineur



**BEHAVIOUR OF PHYSICAL VAPOR DEPOSITED
NANOCOMPOSITE COATINGS UNDER
EXTREME ENVIRONMENTS**

WANG JINGXIAN

Interdisciplinary Graduate School
Energy Research Institute @ NTU (ERI@N)

A thesis submitted to the
Nanyang Technological University in fulfilment of the
requirement for the degree of
Doctor of Philosophy

2016

Statement of Originality

I hereby certify that the work embodied in this thesis is the result of original research and has not been submitted for a higher degree to any other University or Institution.

04/04/2017

.....
Date

Wang Jingxian

.....
Wang Jingxian

Abstract

TiN-based nanocomposite coatings were prepared using physical vapor deposition to deliver enhanced mechanical, tribological and thermal characters that can be exploited for superhard cutting tool surfacing. These properties are controlled by tailoring processing methods to tune the microstructure and microchemistry. This thesis examined three coating systems, which are Ti-Al-N, Ti-Al-Y-N and Ti-Si-N, configured variously as multilayer superlattices and nanocomposites to comprehensively correlate hardness, wear resistance and oxidation resistance with deposition parameters. Combining X-ray diffraction and transmission electron microscopy with physical-mechanical testing, over a wide range of coating configurations, enabled construction of a predictive process-performance matrix to guide the fabrication of hardened surfaces.

In multilayer TiN/Ti_xAl_{1-x}N coatings prepared by cathodic arc deposition, the mechanical properties were controlled by the layer period that was adjusted by varying substrate rotation speed. A hardness of 39 ± 4 GPa was achieved for a superlattice period of 13 nm, where the coatings contain columnar <111> textured rock salt – type crystals connected by low-angle grain boundaries. When yttrium was introduced to the multilayers, by adding a Y - metal target powered by DC magnetron sputtering, the morphology changed from columnar to acicular grains with smaller grain size. Specifically, by fixing the period at 5.5 nm and incorporating Y from 0 to 2.4 at% the grain size decreased (from 100-200 nm to 20-30 nm) and hardness increased (from 29 ± 7 GPa to 41 ± 3 GPa). The improved performance was a consequence of solid solution hardening that arises from the misfit strain field introduced by Y (element atomic radii 2.12 Å) substitution for Ti (1.76 Å) or Al (1.18 Å), and a nanosize effect, where finer grains result in a greater volume fraction of grain boundaries that block dislocation movement. Higher Y additions also retard oxidation as high temperature (800 °C) annealing generates Ti₂O₃, rather than TiO₂ as in Y-

free coatings, and also affects Al oxidation. Adhesion and wear resistance were not compromised by higher Y contents demonstrating that TiN/Ti_xAl_{1-x}N coatings can enhance mechanical properties and thermal stability. Notably, this work employed a pure Y target, instead of a Ti-Al-Y alloy target, and substrate holder rotation speed was the critical parameter, where faster substrate rotation leads to smaller periods and more uniform Y distribution. However, an Y-rich layer became progressively thicker at slower rotation with the period increasing from 5.5 nm to 24 nm. These Y-rich regions seeded crystal nucleation that reduced coherency at layer interfaces and grain boundaries to significantly degrade mechanical properties (41 ± 3 GPa to 30 ± 5 GPa). Therefore, the period and Y content work in tandem in multilayered TiN/Ti_xAl_{1-x}N coatings and the optimized Y content was to be 2.4 at% at a period of 5.5 nm.

Nanocrystallite TiN / amorphous (a)-Si₃N₄ nanocomposites were fabricated by high power impulse magnetron sputtering. The introduction of silicon by controlling the Si target current can be used to modify the coating structure, tailor mechanical properties, improve wear resistance and passivate oxidation. Smaller crystal sizes promoted at higher Si content lead to TiN / amorphous (a)-Si₃N₄ nanocomposites, with ~10 at% Si/(Si+Ti) yielding maximum hardness (41 ± 3 GPa). Compared to TiN, Ti_{0.903}Si_{0.097}N showed enhanced resistance to oxidation and wear resistance, however, the TiN crystallites were not completely encapsulated by a-Si₃N₄ intergranular films and further optimization of the structure and property relationship can be realised.

Resumé

Afin d'obtenir des matériaux aux caractéristiques mécaniques, tribologiques et thermiques améliorées, nous avons élaboré des revêtements nanocomposites à base de TiN en utilisant une technique de dépôt physique en phase vapeur. Ces matériaux aux caractéristiques spécifiques peuvent être exploités pour le surfacage d'outils de coupe de très haute dureté. En ajustant les processus d'élaboration dont dépendent la microstructure et la microchimie des revêtements, il est possible de contrôler les propriétés de ces matériaux. Cette thèse présente les résultats obtenus sur les trois systèmes de revêtement que sont Ti-Al-N, Ti-Al-Y-N et Ti-Si-N, configurés soit en réseaux superposés multicouche soit en nanocomposites. L'accent est mis sur l'étude systématique de la dureté et de la résistance à l'usure et à l'oxydation en fonction des paramètres de dépôt. En combinant la diffraction des rayons X et la microscopie électronique à transmission avec des tests physico-mécaniques sur une large gamme de configurations de revêtement, on établit une matrice processus-performance prédictive permettant de guider la fabrication de surfaces durcies.

La technique de dépôt par arc cathodique a permis la réalisation de revêtements multicouche TiN / $Ti_xAl_{1-x}N$. La période de ces dépôts multicouches, dépendant de la vitesse de rotation du substrat, permet le contrôle des propriétés mécaniques des échantillons. Une période de réseau superposé de 13 nm, pour laquelle les revêtements sont constitués de cristaux colonnaires de type « rock-salt » texturés $\langle 111 \rangle$ reliés entre eux par des joints de grains à angle faible, justifie l'obtention d'une dureté de 39 ± 4 GPa. L'ajout d'une cible d'yttrium métallique alimentée par pulvérisation cathodique magnétron DC autorise l'introduction de l'élément Y dans les empilements multicouches. Dans ces conditions, la morphologie colonnaire des dépôts est modifiée en grains aciculaires de plus petite taille cristalline. Plus précisément, en fixant la période

à 5,5 nm et en incorporant l'yttrium de 0 à 2,4 % atomique, la taille des grains diminue (de 100-200 nm à 20-30 nm) et la dureté est accrue (de 29 ± 7 GPa à 41 ± 3 GPa). Cette amélioration des performances est une conséquence du durcissement en solution solide qui intervient à partir d'un champ de déformation inadapté. Celui-ci est introduit par la substitution de Ti et Al (respectivement 1,76 Å et 1,18 Å de rayon atomique) par Y (2,12 Å), mais aussi par un effet de taille nanométrique, où les cristaux plus fins entraînent une plus grande fraction volumique de joints de grains qui bloquent le mouvement de dislocation. Une plus importante quantité de Y retarde également l'oxydation à haute température (800 °C). En effet, le recuit cristallise la structure Ti_2O_3 en présence d'yttrium, alors que la phase TiO_2 est identifiée dans les revêtements sans yttrium. De plus, la présence d'Y ralentit également l'oxydation de l'aluminium. L'adhérence et la résistance à l'usure ne sont pas impactées par des teneurs plus élevées en Y, démontrant la faisabilité des revêtements $TiN / Ti_xAl_{1-x}N$ dans le but d'améliorer les propriétés mécaniques et la stabilité thermique des échantillons. L'utilisation d'une cible de Y métallique pure au lieu d'une cible d'alliage Ti-Al-Y est une spécificité de ce travail où la rotation du porte substrat est un paramètre critique. En effet, un accroissement de la vitesse de rotation conduit à des périodes plus courtes et à une distribution plus uniforme de Y. Cependant, la diminution de la vitesse de rotation implique l'augmentation de l'épaisseur de la couche riche en Y tandis que la période passe de 5,5 nm à 24 nm. Ces régions riches en Y ensemencent la nucléation des cristaux ce qui réduit la cohérence au niveau des interfaces des couches et des joints de grains conduisant à dégrader de manière significative les propriétés mécaniques (41 ± 3 GPa à 30 ± 5 GPa). Par conséquent, la période et la proportion en Y travaillent en tandem dans les revêtements multicouches $TiN / Ti_xAl_{1-x}N$. La proportion optimale en Y est de 2,4 % atomique pour une période de 5,5 nm pour satisfaire aux critères mécaniques et thermochimiques.

Nous avons élaboré des nanocristaux TiN / α -Si₃N₄-nanocomposites amorphes (a) par pulvérisation cathodique magnétron en régime d'impulsions de haute puissance (HIPIMS). L'introduction de silicium est effectuée en contrôlant le courant dissipé à la cible de Si métallique. Cet élément peut être utilisé pour ajuster la structure, adapter les propriétés mécaniques et aussi améliorer la résistance à l'usure et à l'oxydation de passivation des revêtements à base de TiN. De plus petites tailles cristallines dues à de plus fortes teneur en Si conduisent à des nanocristaux TiN / Si₃N₄-nanocomposites amorphes (a) présentant environ 10% atomiques de Si / (Si + Ti) pour obtenir la dureté maximale (41 ± 3 GPa). Les résistances à l'oxydation et à l'usure du matériau Ti_{0.903}Si_{0.097}N sont renforcées par rapport à celles de TiN. Cependant, les cristallites de TiN ne sont pas complètement encapsulées par le film intergranulaire α -Si₃N₄ au sein de la nouvelle microstructure. Une optimisation plus poussée de la relation structure -propriétés peut donc être réalisée pour obtenir de meilleurs résultats.

Acknowledgements

First I would like to thank my supervisor Assoc. Prof. Dong Zhili. It is an honour to be supervised and advised by him with his contribution of ideas, time and kindness. Through my Ph.D, his support and tutoring were motivational and encouraging, and his enlightening instruction enabled me to complete my work.

I would like to thank my co-supervisor Prof. Tim White and Assoc. Prof. Liu Erjia for their patient guidance on material characterization and mechanical property testing. I am grateful to my mentor Prof. Claude Guet for introducing me to the Singapore-France joint Ph.D program and offering me valuable suggestions.

During my Ph.D I spent one year in Laboratoire de Science et Ingénierie des Matériaux et Procédés in Grenoble, France under the supervision of Prof. Yves Wouters and Assoc. Prof Céline Pascal. I express my gratitude for their insight, patience and encouragement. I also thank my advisors, Prof. Alain Billard and Dr. Mohammad Arab Pour Yazdi in Laboratoire d'Etudes et de Recherches sur les Matériaux, les Procédés et les Surfaces for their coaching on physical vapor deposition techniques and guidance on multiple testings. Special thanks are given to Dr. Frédéric Schuster for funding my work in France and his kind concern on my progress, and Dr. Fernando Lomello for his help and suggestions to improve the research.

Finally, I thank The Energy Research Institute @ NTU for funding my Ph.D project and providing this wonderful oversea exchange experience.

Table of Contents

Abstract	i
Resumé	iii
Acknowledgements	vii
Table of Contents	ix
Table Captions	xiii
Figure Captions	xv
Abbreviations	xxi
Chapter 1 Introduction	1
1.1 Problem statement	2
1.2 Objective and scope	3
1.3 Dissertation overview	4
1.4 Findings and Outcomes	7
References:	8
Chapter 2 Literature review	11
2.1 PVD techniques	12
2.2 PVD hard coatings	14
2.2.1 PVD single phase hard coating	17
2.2.2 Nanostructured coatings	20
2.3 TiN-based ternary and quasi-ternary coatings	26
2.3.1 Ti-Al-N and Ti-Al-Y-N	26
2.3.2 Ti-Si-N	28
2.4 Thesis questions arising from the literature review	29
References:	30

Chapter 3	Experimental methodology	35
3.1	Rationale of selected experiment methods	36
3.2	Hard coatings deposited by PVD	37
3.2.1	Cathodic arc deposition	37
3.2.2	High power impulse magnetron sputtering.....	40
3.3	Characterization methods	43
3.3.1	X-ray diffraction	43
3.3.2	Scanning electron microscopy	46
3.3.3	Transmission electron microscopy	47
3.3.4	Residual stress calculation	50
3.3.5	Nanoindentation test	52
3.3.6	Tensile test	55
3.3.7	Ball-on-disc tribometer	57
3.4	Overview of the methodologies	58
References:	59
Chapter 4	Processing, structure and properties of TiN/Ti_xAl_{1-x}N nano-sized multilayer coatings	63
4.1	Introduction.....	64
4.2	Experimental method	65
4.2.1	Coating deposition	65
4.2.2	Coating characterization	66
4.3	Coating overview processed by arc deposition.....	67
4.3.1	Controlled bilayer period Λ	67
4.3.2	Coating morphology	68
4.4	Coating structures and compositions	69
4.4.1	XRD analysis	69
4.4.2	TEM structural analysis	70
4.4.3	Chemical analysis	74
4.5	Coating properties	75
4.5.1	Hardness and Young's modulus	75

4.5.2 Tribology	77
4.6 Conclusion	78
References:.....	79
Chapter 5 The yttrium effect on the structure and properties of nano-multilayered $Ti_{1-x-y}Al_xY_yN$ coatings.....	83
5.1 Introduction.....	84
5.2 Experimental methods	85
5.2.1 Sample deposition.....	85
5.2.2 Coating characterization	86
5.3 Coating structural analysis.....	88
5.3.1 X-ray diffraction	88
5.3.2 TEM	91
5.4 Coating properties.....	98
5.4.1 Hardness and Young's modulus	98
5.4.2 Coating adhesion and wear resistance	101
5.4.3 Coating oxidation resistance	105
5.5 Conclusion	107
References:.....	108
Chapter 6 The deposition, structure and properties of nanocomposite $TiSiN$ coatings	113
6.1 Introduction.....	114
6.2 Experimental methods	115
6.2.1 Sample deposition.....	115
6.2.2 Sample characterization	116
6.3 Composition and structure analysis	118
6.3.1 Coating texture and crystal size	118
6.3.2 Microstructure and morphology	121
6.4 Ti-Si-N properties	124
6.4.1 Hardness and Young's modulus	124

6.4.2 Tribology	127
6.4.3 Oxidation resistance.....	128
6.5 Conclusion	129
References:.....	130
Chapter 7 Conclusions and future work.....	133
7.1 Conclusions and discussion	134
7.1.1 TiN/Ti _x Al _{1-x} N multilayer coatings.....	134
7.1.2 Yttrium incorporated TiN/Ti _x Al _{1-x} N multilayer coatings.....	135
7.1.3 Nanocomposite Ti-Si-N coatings.....	137
7.2 Future work.....	140
7.3 Implications and outstanding questions	142
References:.....	142
List of Publications	145

Table Captions

Table 5.1	Parameters for $Ti_{1-x-y}Al_xY_yN$ coating deposition.....	86
Table 5.2	Coatings composition at various deposition parameters.....	87
Table 5.3	Substrate rotation speed, corresponding Λ and T^* % of $\langle 111 \rangle$ and $\langle 200 \rangle$ in $Ti_{0.976-x}Al_xY_{0.024}$ coatings	91
Table 6.1	TiN/Si ₃ N ₄ nanocomposite coating deposition parameters.....	117

Figure Captions

Figure 2.1	PVD techniques	14
Figure 2.2	Hardness versus grain size	16
Figure 2.3	Nanocomposite coating categories.	17
Figure 2.4	The schematic illustration of 10-1000eV ion bombardment effect during ion-beam assisted deposition.	18
Figure 2.5	Hardness versus the reciprocal square-root of crystal size of nanocrystalline ZrN coatings deposited by DC magnetron sputtering	20
Figure 2.6	XRD patterns of TiN/NbN with various periods around the (002) reflection (Λ from 2.3 nm to 130 nm)	21
Figure 2.7	Schematic illustration of two multilayer composition	22
Figure 2.8	The predicted hardness obtained by combining models of dislocation gliding in and across TiN/NbN layers compared with measured hardness	23
Figure 2.9	Relationship of hardness versus Si content and of the crystallite size versus Si content of nc-Metal Nitride/a-Si ₃ N ₄ nanocomposites deposited under low-energy ion bombardment plasma assisted CVD	25
Figure 2.10	The phase diagram of as-deposited TiN-YN-AlN quasi-ternary film.....	27
Figure 2.11	Gibbs free energy of mixing TiN and Si ₃ N ₄ at a temperature of 873 K in a nitrogen atmosphere as a function of pressures	29
Figure 3.1	CAD system photo and schematic drawing.....	38
Figure 3.2	Target material emissions from cathode spots.....	39
Figure 3.3	Comparison of plasma densities in nature and materials processing	41
Figure 3.4	The HiPIMS power supply device.....	42

Figure 3.5	The deposition device hybridizing HiPIMS and dc magnetron sputtering.	43
Figure 3.6	XRD Bragg-Brentano geometry	44
Figure 3.7	The sample-electron interaction volume and the corresponding depth where the different signals originate.....	47
Figure 3.8	The two operations of TEM imaging system: Imaging mode and diffraction mode.....	48
Figure 3.9	High-resolution images of the lanthanum oxide grown on silicon taken by conventional TEM and aberration-corrected TEM	49
Figure 3.10	Geometry drawing of a Berkovich tip and an indent image by a Berkovitch tip of Zr-Cu-Al metallic glass	52
Figure 3.11	A typical example of compliance curves in a nanointentation experiment	54
Figure 3.12	A schematic drawing of indentation with parameters used for analysis in Figure 3.11.	55
Figure 3.13	Schematic illustration of the tensile test on metal-coating system and the relationship between tensile strain and crack density ...	56
Figure 3.14	The samples for tensile test and the testing device.	56
Figure 3.15	A ball-on-disc tribometer and a tribology testing illustration....	58
Figure 4.1	Schematic drawing of PVD arc deposition chamber	65
Figure 4.2	SEM fracture of the coating on substrate when rotation speed = 1 r.p.m; TEM bright field image and 4 r.p.m coating cross sections; And Λ vs rotation speed plot	68
Figure 4.3	The 2 r.p.m TiN/Ti _x Al _{1-x} N coating rough surface with a number of droplets; High angle annular dark field (HAADF) image of one droplet construction in STEM mode and its EDX element mappings	69
Figure 4.4	XRD patterns from $2\theta = 30^\circ$ to 60° of TiN/Ti _x Al _{1-x} N coatings deposited at 1 to 7 r.p.m; Zoomed XRD patterns from $2\theta = 40^\circ$ to 46° and the calculated TiN powder XRD pattern.....	70

Figure 4.5	SAED of TiN/Ti _x Al _{1-x} N coatings deposited at 1 r.p.m.($\Lambda=45\text{nm}$), 4 r.p.m.($\Lambda=14\text{nm}$) and 7 r.p.m.($\Lambda=8\text{nm}$).....	71
Figure 4.6	Multilayer overview of the coating deposited at 1 r.p.m with SAED pattern; BFTEM and DFTEM of coatings; And bright field STEM and EDX mapping of the sharp interfaces	72
Figure 4.7	HRTEM images of one grain located between grains in 4 r.p.m TiN/Ti _x Al _{1-x} N coating of the squared area in the inset.	72
Figure 4.8	2 r.p.m TiN/Ti _x Al _{1-x} N coating HRTEM image and corresponding FFT showing an obvious epitaxy along [111] and the presence of misfit dislocations.....	73
Figure 4.9	A grain of 4 r.p.m coating and its FFT diffraction patterns.....	74
Figure 4.10	STEM BF image of the 1 r.p.m TiN/Ti _x Al _{1-x} N coating and EDX element maps; Line scan profiles perpendicular to coating surfaces of 1 r.p.m and 4 r.p.m coatings	75
Figure 4.11	Plots of H and E versus Λ of coatings	76
Figure 4.12	1 r.p.m., 4 r.p.m. and 7 r.p.m coatings μ vs sliding distance and the wear scar profiles	78
Figure 5.1	Coating Λ versus the substrate rotation speed in deposition as Y target fixed at 2300 W.	87
Figure 5.2	XRD patterns of 5 r.p.m Ti-Al-Y-N coatings with 0 at%, 1.2 at% and 2.4 at% Y in rock-salt fcc structure with $\langle 111 \rangle$ texture.....	89
Figure 5.3	XRD patterns of 1 - 5 r.p.m Ti _{0.976-x} Al _x Y _{0.024} coatings and random TiN powder (ICSD-644780) pattern.....	90
Figure 5.4	Cross-section DFTEM images of 5 r.p.m Ti _{1-x} Al _x N, Ti _{0.988-x} Al _x Y _{0.012} N and Ti _{0.976-x} Al _x Y _{0.024} N coatings ($\Lambda = 5.5 \text{ nm}$) of different sizes and grain morphologies	92
Figure 5.5	Cross-section SAED of 5 r.p.m Ti _{1-x} Al _x N, Ti _{0.988-x} Al _x Y _{0.012} N and Ti _{0.976-x} Al _x Y _{0.024} N coatings($\Lambda = 5.5 \text{ nm}$)	92
Figure 5.6	Ti _{0.988-x} Al _x Y _{0.012} N ($\Lambda = 5.5 \text{ nm}$) coating at high magnification; Crystallite FFT and low-angle grain boundary FFT.....	93

Figure 5.7	Wurtzite grain indicated in high resolution TEM of $Ti_{0.988-x}Al_xY_{0.012}N$ ($\Lambda = 5.5$ nm).....	94
Figure 5.8	DFTEM images and corresponding SAED of 3 r.p.m coating ($\Lambda = 8$ nm) in acicular grain morphology and 2 r.p.m coating ($\Lambda = 13$ nm) in equiaxed grain morphology.....	96
Figure 5.9	HRTEM image of 1 r.p.m coating squared area in (b); STEM BFTEM image and EDX element maps indicating multilayer structure; The element profile is along the line in (c).....	97
Figure 5.10	The wurtzite phase presence in 1 r.p.m coating proved by HRTEM with FFT diffractions.	98
Figure 5.11	The y value in 5 r.p.m $Ti_{1-x-y}Al_xY_yN$ ($\Lambda = 5.5$ nm) versus hardness, Young's modulus variation and compressive stress ..	99
Figure 5.12	Hardness and Young's modulus and compressive stress of $Ti_{0.976-x}Al_xY_{0.024}N$ coatings in different period	100
Figure 5.13	<i>In-situ</i> SEM BEI of 5 r.p.m $Ti_{1-x-y}Al_xY_yN$ coatings (y = 0, 0.012 and 0.024) at tensile strain $\epsilon = 3\%$, 10% and 27%	103
Figure 5.14	Comparison of crack density change of 5 r.p.m $Ti_{1-x-y}Al_xY_yN$ coatings (y = 0, 0.012 and 0.024) with increasing strains.	103
Figure 5.15	Friction coefficient changes versus sliding distance and wear rate comparison of $Ti_{1-x}Al_xN$, $Ti_{0.988-x}Al_xY_{0.012}N$ and $Ti_{0.976-x}Al_xY_{0.024}N$ 5 r.p.m coatings.	105
Figure 5.16	XRD patterns of 5 r.p.m $Ti_{1-x}Al_xN$, $Ti_{0.988-x}Al_xY_{0.012}N$ and $Ti_{0.976-x}Al_xY_{0.024}N$ ($\Lambda = 5.5$ nm) after 800°C in air for 10 hours.....	106
Figure 6.1	Schematic of the hybrid of DC-pulsed magnetron sputtering and HiPIMS deposition system	117
Figure 6.2	The Si to (Si+Ti) cation ration versus the current applied on Si target	118
Figure 6.3	XRD patterns of $Ti_{1-x}Si_xN$ coatings containing Si content from 0 to 19.72 at%	119
Figure 6.4	The T^* % of $\langle 111 \rangle$ and $\langle 200 \rangle$ texture versus Si content.....	120

Figure 6.5	Ti _{1-x} Si _x N coatings crystal size versus Si content	121
Figure 6.6	SEM Cross sections of TiN and Ti _{0.903} Si _{0.097} N.....	122
Figure 6.7	TEM Cross sections of Ti _{0.994} Si _{0.006} N and Ti _{0.903} Si _{0.097} N with SAED insets	123
Figure 6.8	The HRTEM image in [1-10] zone axis showing boundary of Ti _{0.903} Si _{0.097} N between a pair of twin grains	123
Figure 6.9	Coating hardness and Young's modulus versus Si content	125
Figure 6.10	The strong one-monolayer Si ₃ N ₄ interface between two TiN (111) slabs.....	126
Figure 6.11	Recorded friction coefficient against sliding distance of TiN and Ti _{0.903} Si _{0.097} N; and their scar profiles.....	127
Figure 6.12	XRD of annealed samples of varied Si content (Annealling condition: 700°C for 2 h in air).....	128
Figure 6.13	Coating hardness versus Si content before annealing and after annealing	129
Figure 7.1	The thermodynamically preferred structure of Ti ₄₃ Si ₇ N ₅₀ based on molecular dynamics simulations.....	139

Abbreviations

Λ	Period
μ	Friction coefficient
BFTEM	Bright field transmission electron microscopy
CAD	Cathodic arc deposition
DC	Direct current
DFTEM	Dark field transmission electron microscopy
E	Young's modulus
E*	Effective Young's modulus
EDX	Energy dispersive X-ray spectroscopy
EELS	Electron energy loss spectroscopy
FCC	Face centred cubic
FESEM	Field emission scanning electron microscopy
FFT	Fast Fourier transformation
FIB	Focus ion beam
FWHM	Full width at half maxima
H	Hardness
HiPIMS	High power impulse magnetron sputtering
HAADF	High angle annular dark field
HR	High resolution
HSS	High speed steel
LLD	lower limit of detection
PLAPT	Pulsed laser atom probe tomography
PVD	Physical vapor deposition
R.P.M	Revolution per minute
SAED	Selected area electron diffraction
SCCM	Standard cubic centimeters per minute
SEI	Secondary electron imaging
SEM	Scanning electron microscopy

STEM	Scanning transmission electron microscopy
TEM	Transmission electron microscopy
XPS	X-ray photoelectron spectroscopy
XRD	X-ray diffraction
T*	Texture coefficient
TGA	Thermal gravimetric analysis

Chapter 1

Introduction

This thesis is concerned with the design, fabrication and testing of TiN-based protective coatings prepared by physical vapor deposition techniques for deployment in high wear and elevated temperature environments. The study compared the efficacy of selected deposition systems, evaluated the microstructure and crystallography of the coatings, and investigated their physical characters, particularly mechanical properties. As expected, coating hardness and macroscale responses to extreme temperature and friction correlate with compositional and structural modulations that can be tuned by adjusting the deposition process to optimize performance. This approach informs the research strategy of this thesis which demonstrates that coating performances can be enhanced by taking a principle-based approach to the selection of process parameters in various environments.

1.1 Problem statement

Hard protective coatings are required in industries that exploit high-speed machining, casting and hot-forming. Titanium nitride (TiN) deposited by physical vapor deposition (PVD) has been used to prepare wear and corrosion resistant surfaces since the early 1980s [1]. Many PVD techniques to lay down TiN films have been explored and developed, ranging from evaporation guns [2, 3] to arc sources [4, 5] and sputtering methods [6, 7], that can treat substrates of varied size and shape. A significant challenge is that TiN has poor thermal stability beginning to oxidize from 550°C [8], and requires high deposition temperatures to ensure acceptable substrate-coating adherence. These factors, that have limited the applicability of TiN and added to fabrication costs, are driving research into low temperature deposition methods that yield durable TiN finishes.

Such techniques include PVD, that has been widely studied to obtain coatings that work at extreme conditions while preserving high hardness, thermal stability, low friction and good adherence [9]. Fundamentally, strengthening mechanisms [10, 11] should hinder dislocation movement, and this is typically achieved by introducing atomic substituents, seeding secondary phases, inserting point or line defects, and increasing the prevalence of grain boundaries. Consequently, superhard PVD coatings require design concepts where multiple components and structures are introduced. For example, a solid solution coating for drills incorporates aluminum in TiN to passivate oxidation and enhance cutting performance [12]. Furthermore, TiN-based coatings can have tailored microstructures, including superlattice assemblies such as TiN/CrN [13], TiN/AlN [14], TiN/VN [15], TiN/NbN [16] and dual-phase nanocomposite coatings including TiN/Si₃N₄ [17] TiN/TiB₂ [18], and TiN/BN [19], where intricate deposition parameters, sometimes followed by heat treatment, create coatings of exceptional performance. For complex hard

coatings, knowledge-driven design becomes critical for further advancement. This is especially so for microstructural optimization where performance is not readily explained using topological rationalizations. Therefore, this thesis targets the first-principles design of hard coatings deposited by PVD and correlates structure with process parameters and coating performance under elevated temperatures where plastic deformation, friction and oxidation can be significant.

1.2 Objective and scope

The objectives of this thesis are to:

- Design TiN-based multi-compositional and multi-structural coatings, for high friction and elevated temperature environments;
- Deposit nanocomposite hard coatings by PVD and analyze structural and crystallochemical details by diffraction and microscopy; and
- Realize structure control by varying PVD processing parameters and explore the correlation between coating microstructures and mechanical properties, friction and high temperature performances.

The scope of this work includes:

- Selection of coating composition systems where structural modulation will be used to improve coating mechanical properties and thermal stabilities.
- Deposition of TiN-based coatings by PVD techniques based on:
 - ◆ Cathodic arc deposition (CAD); and
 - ◆ High power impulse magnetron sputtering (HiPIMS).
- Characterize microchemistry and microstructure by:
 - ◆ Examining coating cross-sections by scanning electron microscopy (SEM);
 - ◆ Verifying the coating texture by X-ray diffraction (XRD) conducted in Bragg-Brentano geometry;

- ◆ Measuring the grain and crystal size by a combination of XRD and transmission electron microscopy (TEM);
- ◆ Revealing structural details including grain morphology, grain boundaries and secondary phases by high resolution transmission electron microscopy (HRTEM); and
- ◆ Determining the microchemical composition by energy dispersive X-ray (EDX) analysis coupled with SEM.
- Evaluation of coating performance including:
 - ◆ Mechanical properties, mainly hardness and Young's modulus by nanoindentation;
 - ◆ Wear resistance by checking the friction scar after ball-on-disc tribology tests;
 - ◆ Adherence by *in-situ* tensile testing in an SEM; and
 - ◆ Oxidation resistance through analyzing coating oxide composition by XRD after heat treatment.
- Demonstration of the reproducible control of:
 - ◆ Critical coating processing parameters for the delivery of specific microstructures; and
 - ◆ Film microstructure correlations with coating performances.
- Integration of process parameter selection for the tailoring of overall coating performance.

1.3 Dissertation overview

The Thesis contains 7 Chapters.

Chapter 1 describes the needs and challenges to manage the expanding complexity of hard TiN-based films within a framework of an incomplete fundamental understanding of the correlations among specific processing

methods, structures, composition and properties. These questions define Objective and Scope of the investigation.

Chapter 2 reviews the principle PVD techniques and the origins of hardening initiated by ion bombardment. The compositional and structural design principles of superhard coatings are presented, along with modelling, that underpins the experimental and characterization methodology used in the following Chapters. Particular attention is paid to state-of-the-art nano-scale ternary systems that deliver enhanced mechanical and thermal properties. Finally, open questions regarding the TiN systems are collated as a basis for defining the problem statement of these studies.

Chapter 3 describes the principles and practice of the major experimental methods employed in this thesis, including coating deposition techniques (CAD and HiPIMS), structure characterization techniques (XRD and electron microscopy), and physical property testing (nanoindentation, tribology and tensile tests). These complementary methods are integrated to comprehensively analyse hard coating processing, structure and properties that provide guidance to deploy PVD techniques and optimize materials performance.

Chapter 4 details multilayer TiN/Ti_xAl_{1-x}N coatings deposited by CAD with variable superlattice periods that deliver distinct mechanical and tribological properties. The textures, grain morphology and grain boundaries, were intensely studied by XRD and TEM, including dark field imaging, selected area diffraction, high resolution TEM and EDX analysis. By constraining the periods (Λ) from 8 nm to 45 nm, a hard nanosized multilayer system was obtained (maximum hardness $i= 39 \pm 4$ GPa at a period around 13 nm). Moreover, the correlation between mechanical properties and period-modified microstructure, including superlattice dimension, composition modulation and interface conditions, was established.

Chapter 5 elaborates the modification of CAD multilayer TiN/Ti_xAl_{1-x}N coatings through the addition of 0 – 2.4 at% yttrium (Y) by direct current (DC) magnetron sputtering and the variation of period Λ from 5.5 nm to 24 nm that improves mechanical and tribological properties, adherence and high temperature oxidation resistance (800°C in air). This chapter describes how coating microstructure characterized by XRD and TEM was determined by both Y content and Λ . For example, at fixed Y addition of 2.4 at%, a decreasing period from 24 nm to 5.5 nm lead to improved hardness H, from 30 ± 5 GPa to 41 ± 3 GPa and Young's modulus E, from 424 ± 50 GPa to 490 ± 47 GPa. Conversely, for a fixed period of 5.5nm, an Y addition of 2.4 at% gave higher hardness (41 ± 3 GPa) compared with the Y-free coating (29 ± 7 GPa) and better oxidation resistance without degrading adherence and wear resistance. Overall, properties were determined by texture, grain size and grain morphology evolution that could be controlled by Y doping. These insights can guide the selection of coating processes.

Chapter 6 explores the Ti-Si-N nanocomposite system deposited through the dual use of HiPIMS on a Ti target and DC-pulsed magnetron sputtering of a Si target. The product was a composite of nanocrystalline TiN and amorphous Si₃N₄, with Si / (Si + Ti) = 0 to ~ 20 at%, controlled by the Si target power. The crystallite size decreased to < 10 nm by increasing Si content above 10 at%. The as-deposited and annealed coatings, characterized by nanoindentation reveal that with ~ 10 at% Si the superior hardness was achieved while higher Si content (~ 20 at%) resulted in both better hardness and oxidation resistance when annealed at 700°C in air. The hardening effect in Ti-Si-N composites arises from the nanocomposites structure with the appropriate volume ratio between nanosize crystallite to X-ray amorphous Si₃N₄ at grain boundaries. However, the nanocomposite described in this chapter requires further optimisation to obtain the superior mechanical properties suggested possible through modelling.

Chapter 7 summarizes and discusses the outcomes of the Thesis. This work demonstrates that TiN-based nanocomposite coatings can be well controlled by adjusting processing parameters and show potential for use in the high speed machining industry. However, additional questions have arisen to fully understand the correlation between processing, structure and performance. These questions are concerned with developing better mechanistic understanding of structure and performance variations driven by processing, especially the oxidation and hardening mechanisms. Such optimizations are required to deposit super ($80 \text{ GPa} \geq H \geq 40 \text{ GPa}$) and ultra-hard ($H \geq 80 \text{ GPa}$) Ti-Si-N coatings.

1.4 Findings and Outcomes

The novelty of this thesis arises from correlating advanced coating performance with microstructural and microchemical analyses that allow the definition of parameter design criteria using large-scale PVD techniques. The outcomes include:

- Revealing microstructural details for both superlattice modulation and nanocrystalline/amorphous composite texture using aberration-corrected transmission electron microscopy;
- Deposition of pre-determined TiN-based coating systems with the desired nanostructures through well-controlled single or hybrid PVD techniques;
- Establishing the links among fabrication, microstructure and coating performance and elaborating the decisive processing parameters (multilayer period and reactive element content) on grain morphology, film hardening and thermal stability; and
- Fabricating for the first time Ti-Al-Y-N nano-multilayer architectures by employing a power controlled Y target together with varying

substrate holder rotation speed, rather than through the conventional approach of using a TiAlY alloy target.

References:

- [1] K. Nakamura, K. Inagawa, K. Tsuruoka and S. Komiya, *Thin Solid Films*, **1977**, 40, 155-167.
- [2] S. Komiya, N. Umezu and C. Hayashi, *Thin Solid Films*, **1979**, 63, 341-346.
- [3] R. Buhl, H. K. Pulker and E. Moll, *Thin Solid Films*, **1981**, 80, 265-270.
- [4] F.-H. Lu and H.-Y. Chen, *Surf. Coat. Technol.*, **2000**, 130, 290-296.
- [5] A. J. Perry, J. R. Treglio and A. F. Tian, *Surf. Coat. Technol.*, **1995**, 76-77, Part 2, 815-820.
- [6] H. Z. Wu, T. C. Chou, A. Mishra, D. R. Anderson, J. K. Lampert and S. C. Gujrathi, *Thin Solid Films*, **1990**, 191, 55-67.
- [7] V. Valvoda, *Surf. Coat. Technol.*, **1996**, 80, 61-65.
- [8] M. Wittmer, J. Noser and H. Melchior, *J. Appl. Phys.*, **1981**, 52, 6659-6664.
- [9] I. Petrov, P. B. Barna, L. Hultman and J. E. Greene, *J. Vac. Sci. Technol., A*, **2003**, 21, S117-S128.
- [10] S. Veprek, M. G. J. Veprek-Heijman, P. Karvankova and J. Prochazka, *Thin Solid Films*, **2005**, 476, 1-29.
- [11] J. Musil, *Surf. Coat. Technol.*, **2000**, 125, 322-330.
- [12] W. D. Münz, *J. Vac. Sci. Technol., A*, **1986**, 4, 2717-2725.
- [13] H. C. Barshilia, A. Jain and K. S. Rajam, *Vacuum*, **2003**, 72, 241-248.
- [14] M. A. Auger, R. Gago, M. Fernández, O. Sánchez and J. M. Albella, *Surf. Coat. Technol.*, **2002**, 157, 26-33.
- [15] U. Helmersson, S. Todorova, S. A. Barnett, J. E. Sundgren, L. C. Markert and J. E. Greene, *J. Appl. Phys.*, **1987**, 62, 481-484.
- [16] X. Chu, M. S. Wong, W. D. Sproul, S. L. Rohde and S. A. Barnett, *J. Vac. Sci. Technol., A*, **1992**, 10, 1604-1609.

-
- [17] S. Vepřek, S. Reiprich and L. Shizhi, *Appl. Phys. Lett.*, **1995**, 66, 2640-2642.
- [18] C. Mitterer, P. Losbichler, F. Hofer, P. Warbichler, P. N. Gibson and W. Gissler, *Vacuum*, **1998**, 50, 313-318.
- [19] E. Benko, J. S. Stanisław, B. Królicka, A. Wyczęsany and T. L. Barr, *Diamond Relat. Mater.*, **1999**, 8, 1838-1846.

Chapter 2

Literature review

Hard coating microstructure design concepts implemented via a great variety of physical vapor deposition (PVD) techniques have been widely studied. This Chapter introduces the principle PVD methods and outlines their specific advantages and limitations for hard coating deposition. Of greatest significance is the observation that nanocomposite functionality is determined primarily by the chemical composition and layer modulation. With these two constructs, several structural models are presented that define the key questions and scope of the following Chapters. In addition to examining the principles underpinning these models, particular attention is paid to ternary systems where nanoscale tuning can enhance mechanical and thermal properties. Using this review for guidance, nanomultilayer and nanocrystalline/amorphous composite systems were selected for experimentation on the basis of their current developmental status and potential for performance optimisation.

Protective hard coatings have been applied in the machining industry since the 1970s to improve tool life and productivity. Investigations of processing techniques and film properties for improving performance (i.e. abrasive wear, chemical corrosion and high temperature durability) under extreme conditions are ongoing. Most efforts are towards reducing the synthesis temperature and concomitantly enhancing hardness (H) and oxidation resistance [1-3]. Coatings with H in the range of $20 \text{ GPa} < H < 40 \text{ GPa}$ and $H > 40 \text{ GPa}$ are described as hard and superhard respectively. The reference superhard materials are amorphous carbon nitride, cubic boron nitride, and amorphous diamond-like carbon [4-6]. New hard coating designs will be essential to meet future industrial demands for machining, forming and stamping tools.

Crystal size and grain size determine many materials properties including heat conductivity [7], phase transition temperature [8], elastic modulus [9], electrical conduction [10] and coercive force [11]. In particular, the concept of hardened bi-phasic nanocomposite coatings has drawn the attention of researchers where nanocrystalline and/or amorphous phases are integrated as layered, columnar or equiaxed structures. Physical vapor deposition (PVD) is a well established technique widely used for preparing hardened tool coatings. This Chapter introduces PVD techniques for fabricating hard coatings, reviews the structural and chemical modulation of nanocomposite coatings, and rationalizes the performance of PVD nanocomposite coatings under extreme environments.

2.1 PVD techniques

PVD is a coating method where atoms, plasmas or molecules are physically vaporised from a source before transportation and condensation on a substrate. It can be employed for a wide range of materials, including almost all inorganic and many organic coatings. The PVD methods can be classified as the following types (Figure 2.1) [12]:

- a) *Vacuum evaporation* in which material is thermally evaporated from the source and arrives at the substrate through a vacuum chamber;
- b) *Sputter deposition* where the target is eroded and atoms ejected from a target by an accelerated sputter gas that is typically inert, and deposited on the substrate. A magnetron field is commonly employed on the target surface to enhance collision flux of the sputter gas and target and deliver a higher deposition rate;
- c) *Arc deposition* where material is vaporized by a high-current electric arc from a target that serves as a cathode or anode. The generated plasmas are deposited on the substrate in a low-pressure chamber; and
- d) *Ion plating* in which energetic particles bombard the target to deposit material onto the substrate to control coating composition and realize property modification. The depositing material is mobilized by thermal evaporation, sputtering or an electric arc. Energetic particles can be extracted from the plasma if the deposition occurs in a plasma environment or is generated from a separate ion gun in vacuum. The latter method is known as ion-beam assisted deposition (IBAD).

Each technique has its own advantages and disadvantages. For example, cathodic arc deposition efficiently ionizes atoms, but adversely can generate macro droplets. As for sputter deposition, coatings can maintain target compositions with better adhesion compared to other methods, but the deposition rate is slow. To minimise the drawbacks and optimize coating performance, a hybrid of different methods is necessary, as has been described previously [13-15]. In particular, injecting reactive gas, e.g. N₂ and O₂, induces reactions with target vapor at the substrate surface in a process called reactive PVD [16].

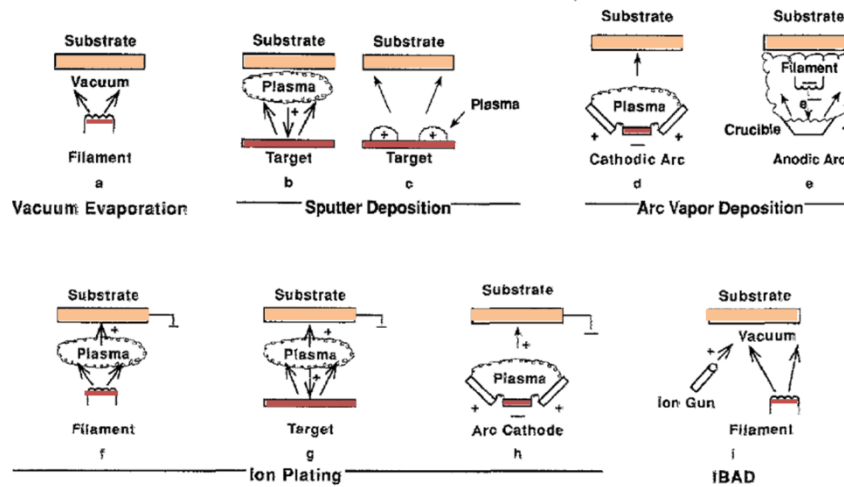


Figure 2.1 PVD techniques: (a) vacuum evaporation; (b) sputter deposition; (c) magnetron sputtering; (d) cathodic arc deposition; (e) anodic arc deposition; (f) ion plating with filament evaporation; (g) ion plating with sputtered target; (h) arc ion plating; (i) ion-beam assisted deposition*.

In general, PVD techniques are suitable for depositing heterogeneous coatings, especially nanosized crystalline and/or amorphous single- or poly- phase assemblages that can enhance hardness, toughness and wear resistance. However, each technique yields distinctive structural and chemical features with respect to phase composition, grain size, coating texture, surface conditions and defects. It appears likely that non-equilibrated coatings by PVD techniques will be integrated into various hardening mechanisms. This will require the examination of coating residual stress, grain size, phase identification and distribution.

2.2 PVD hard coatings

* Reprinted from Metal Finishing, Vol.100, Donald M. Mattox, Physical vapor deposition (PVD) processes, Pages No.396, Copyright (2016), with permission from Elsevier.

Hardness (H) is the resistance of a material to local plastic deformation resulting from atom displacement, dislocation climb and glide, grain boundary sliding and atomic diffusion. Hardness is determined both by the nature of atomic bonding, and structure on a variety of length scales. Theoretically, the hardness can be estimated from yield strength, elastic modulus E and the Poisson ratio γ based on the Marsh-relation [17]:

$$\frac{H}{Y} = 0.28 + 0.60 \times \frac{3}{3-\varphi} \ln \frac{3}{\varphi + 3\mu - \varphi\mu} \quad (2.1)$$

where Y is the material yield strength and maximum $Y = E/10$; $\varphi = (1 - 2\gamma)Y/E$; and $\mu = (1 + \gamma)Y/E$. For TiN, the calculated hardness would be 40-53 GPa, but in reality this is never achieved because of the presence of lattice defects and micro-cracks.

On the other hand, the coating hardness is dependent on crystal size. Nanocrystalline coatings show enhanced mechanical properties because the dislocation density in smaller crystals is reduced, as the stress to initiate dislocation is inversely proportional to the distance between two dislocation pinning centers [18]. The grain size d strengthening effect can be described by the Hall-Petch relation [19, 20]:

$$\sigma_y = \sigma_o + k \frac{1}{\sqrt{d}} \quad (2.2)$$

where σ_y is the yield stress, σ_o is the lattice stress to dislocation movement and k is the Hall-Petch constant that depends on the grain boundary strengthening contribution for a specific material. It has been reported that decreasing grain size from macro-scale to nano-scale enhanced hardness by 5 to 10 times in nanophase metals [21]. However, below a critical grain size d_c the hardness deteriorates as the fraction of grain boundary atoms increases and interface sliding becomes dominant. As reported, the weakened hardness when grain size falls below d_c follows a reverse Hall-Petch relationship with d, expressed by

formula 2.2, but with negative k present [22]. The overall relationship of hardness versus grain size is shown in Figure 2.2 [23].

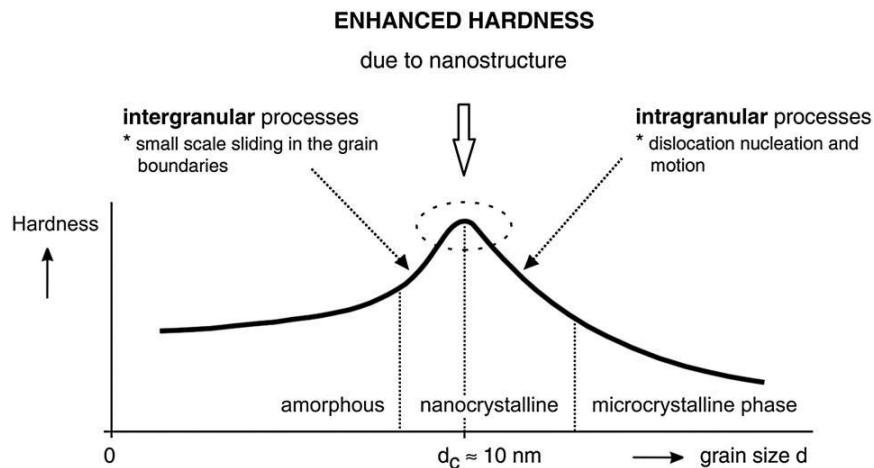


Figure 2.2 Hardness versus grain size*.

Combining the nature of atomic bonding and consideration of grain size effects gives rise to a generalized concept of multi-phase nanocomposite coatings that can be categorized in four types: (1) nanosized multilayer structure; (2) nanocolumnar structure; (3) multi-phase nanograins; and (4) nanocrystallites embedded in an intergranular phase (Figure 2.3). The multilayer and nanocolumnar structure types are particularly sensitive to ion bombardment that is controlled by the substrate and target configuration selected for deposition. The multiple phase nano-grain type and nano-grain and matrix phase type are highly susceptible to thermodynamic phase segregation. The nanocomposite structure is distinguished by a transition zone located between two crystalline phases or a transition from a crystalline to amorphous phase [3].

* Reprinted from Surface and Coatings Technology, Vol.207, J.Musil, Hard nanocomposite coatings: Thermal stability, oxidation resistance and toughness, Pages No.51, Copyright (2016), with permission from Elsevier.

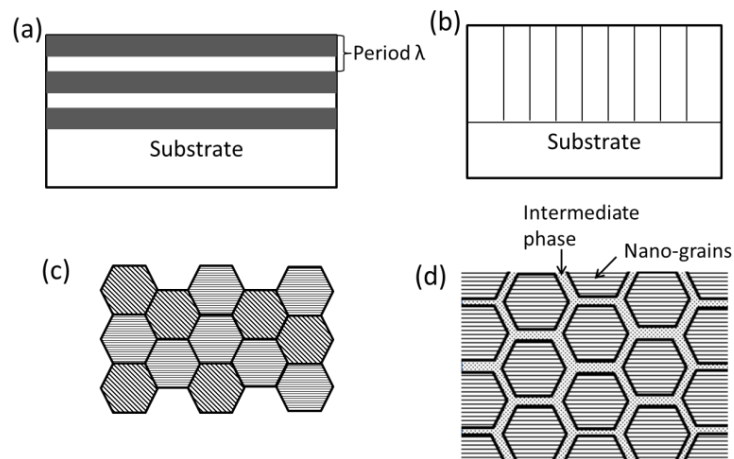


Figure 2.3 Nanocomposite coating categories: (a) Nanosized multilayer structure (cross-section view); (b) Nanocolumnar structure (cross-section view); (c) Bi-phase nanograin structure (plane view); (d) Nanocrystalline encapsulated by secondary phase (plane view) [3].

2.2.1 PVD single phase hard coating

Before addressing the correlation between microstructure and mechanical properties in a multi-phase modulated nanocomposite, the film growth influences on the single phase coatings, such as TiN or CrN, requires review.

During deposition, energetic ion bombardment of the film surface is a key factor modifying coating density and morphology [24]. In PVD the bombardment intensity is determined by the substrate bias and the ion and atom energy evaporated or sputtered from target. Ion bombardment causes a series of structural modifications, including finer grain sizes and insertion of lattice defects, which creates residual stress that has a hardening effect.

Possible lattice defects induced by incident energetic ions are shown in Figure 2.4 [25]. The incident ions displace atoms and may be implanted, or recoil and cause the collision cascades. At higher energies, a proportion of incident ions can channel deep below the surface creating a large number of point defects, i.e.

residual interstitials and vacancies. Deep collision cascades can initiate line, planer and bulk defects. These defects can be characterized by high resolution transmission microscopy (HRTEM).

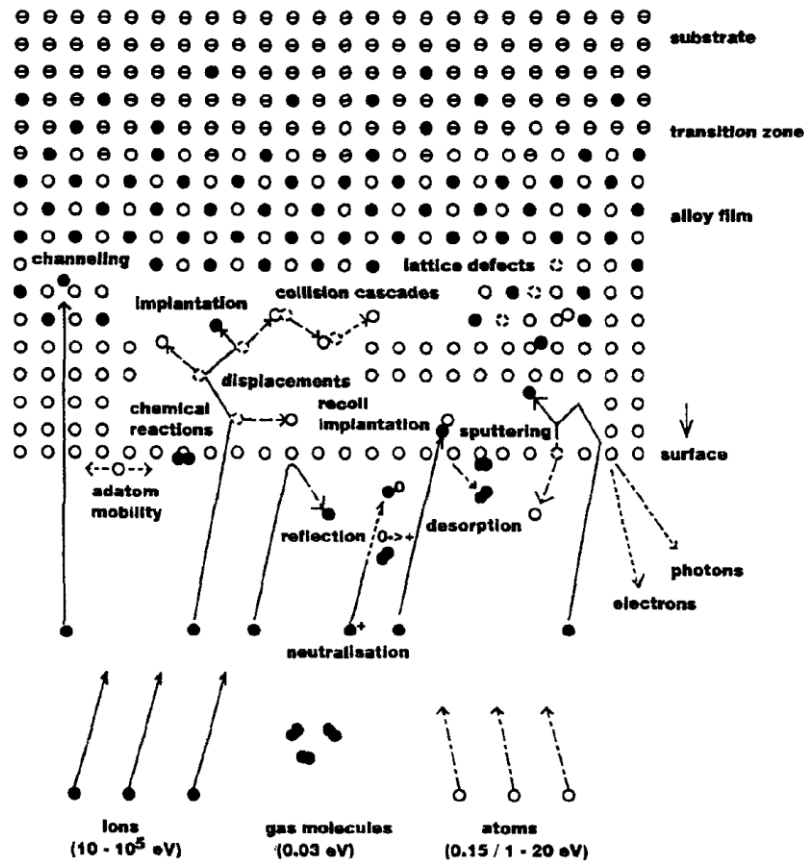


Figure 2.4 The schematic illustration of 10-1000eV ion bombardment effect during ion-beam assisted deposition.*

In general, PVD TiN coatings show columnar structures at a scale of 0.1 – 1 μm [26], connected by low-angle and high-angle grain boundaries [27]. Low-angle grain boundaries result from dislocation alignments that favour specific inter-crystalline orientations. Alternatively, adjacent crystals may have high-angle misorientations generated along coincident crystal lattices.

* Reprinted from Nuclear Instruments and Methods in Physics Research B, Vol.127/128, W. Ensinger, Low energy ion assist during deposition – an effective tool for controlling thin film microstructure, Pages No.799, Copyright (2016), with permission from Elsevier.

Point defects in coating microstructures modify macro-residual stress. As point-defect interstitials arising from collision cascades dilate film volume over the substrate surface, a compressive stress is imparted to the adherent film [28]. During arc deposition, the compressive stress increases when a higher negative bias voltage is applied to the substrate holders [29], while in magnetron sputtering, stress increases linearly with the square root of particle energy [30]. Defects in strained films can effectively hinder dislocation movement, leading to enhanced hardness. A linear relationship of hardness versus residual stress has been reported in many single-phase coatings, such as CrN [31, 32], TiN [16] and ZrN [33].

Furthermore, single-phase coatings are found to harden following the Hall-Petch relationship. For example, Qi et al. [34] found the hardness of ZrN was enhanced from 20 GPa to 34 GPa when crystal size decreased from 45 nm to 19 nm by raising the substrate bias (Figure 2.5). This was attributed to the higher volume fraction of grain boundaries that created: (1) larger stress fields due to dislocations piling up at the boundaries [35], and (2) additional dislocations arising in the grain boundaries [36]. However, hardness decreased when the crystal size fell below 19 nm. This reversal was neither due to artifacts, such as porosity, the presence of secondary phases, compositional variation, texture or compressive stress. Instead, an inverse Hall-Petch effect was proposed, where dislocations are absent in smaller crystals and do not contribute to boundary. This model proved appropriate as the predicted critical crystal size agreed with experimental observations.

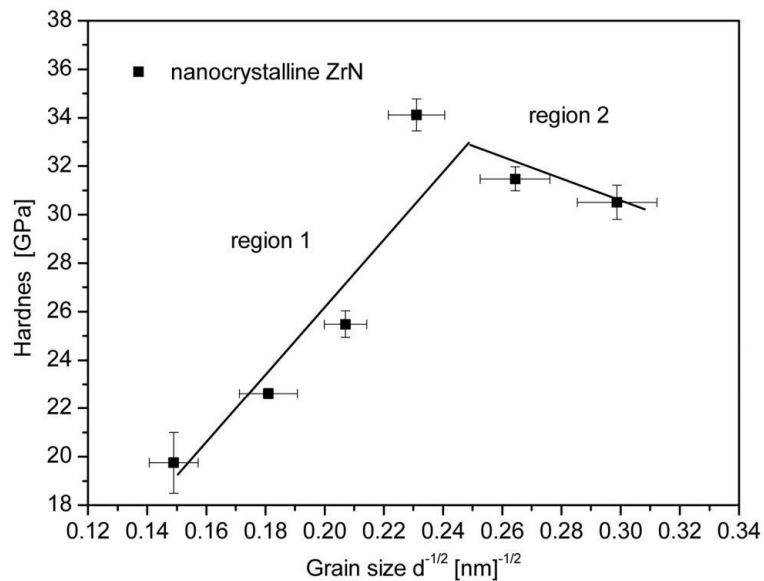


Figure 2.5 Hardness versus the reciprocal square-root of crystal size of nanocrystalline ZrN coatings deposited by DC magnetron sputtering*

2.2.2 Nanostructured coatings

Nanostructured coatings can be classified in four types (Figure 2.3). This section describes the relationship between microstructure and mechanical properties of the widely studied Type 1 nanosized multilayer coatings and Type 4 nanocrystalline/intermediate composite coatings which are explored in this Thesis.

(a) *Nano-scale multilayer coatings*. This type of thin film with enhanced hardness can be characterized by both the chemical composition of the composite layers and the multilayer period Λ . These coatings require multiple source materials to be deposited in nano-scale films. Typically, PVD methods employ a rotating substrate to realize alternate layer modulations that can be characterized directly by TEM or indirectly by

* Reprinted from Surface and Coatings Technology, Vol.205, Z.B. Qi, P. Sun, F.P. Zhu, Z.C. Wang, D.L. Peng, C.H. Wu, The inverse Hall–Petch effect in nanocrystalline ZrN coatings, Pages No.3696, Copyright (2016), with permission from Elsevier.

X-ray diffraction. For multilayer superlattices, a characteristic XRD pattern contains satellite reflections around the Bragg reflections. Figure 2.6 shows a series of XRD patterns of TiN/NbN of various periods deposited on a MgO substrate [37]. Two reflections belonging to NbN and TiN can be resolved when $\Lambda = 130$ nm, while only one Bragg peak appears for $\Lambda = 9.4$ nm surrounded by satellite pairs, whose positions are dictated by the period Λ .

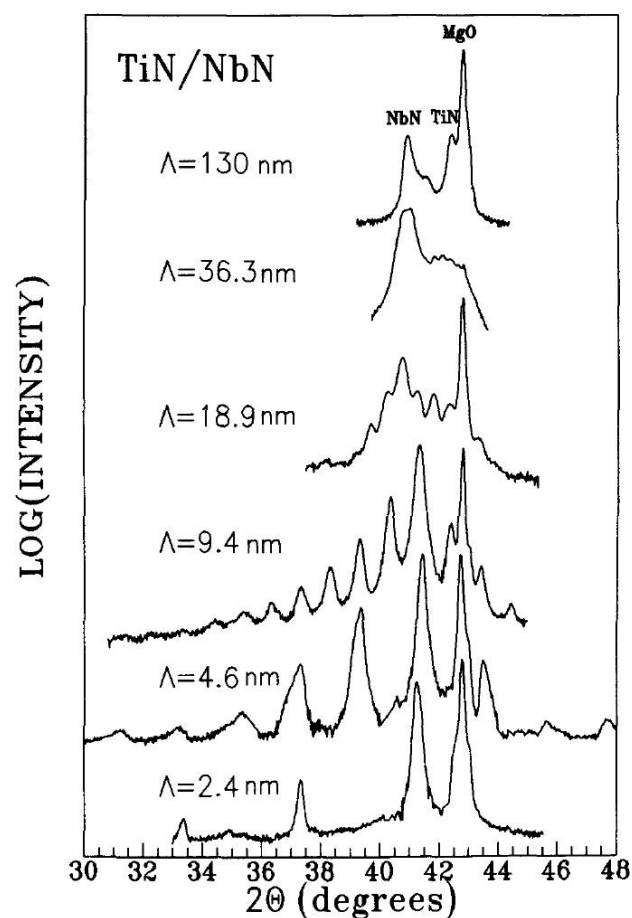


Figure 2.6 XRD patterns of TiN/NbN with various periods around the (002) reflection (Λ from 2.3 nm to 130 nm)*

* M. Shinn, L. Hultman and S.A. Barnett, Growth, structure, and microhardness of epitaxial TiN/NbN superlattices, *Journal of Materials Research*, 7, 04, 903, copyright (2016), reproduced with permission.

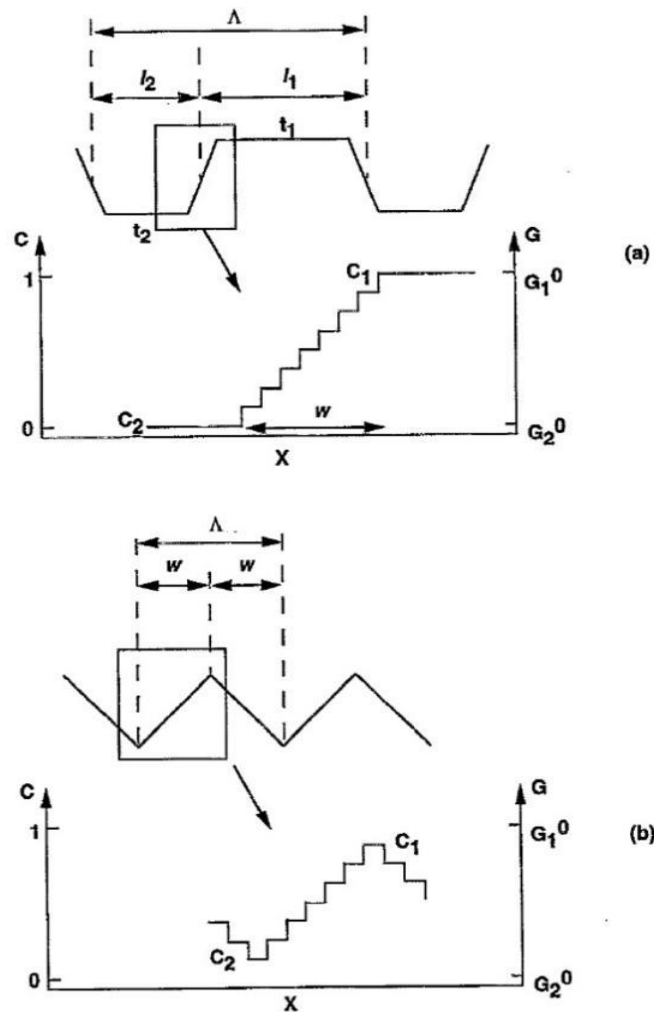


Figure 2.7 Schematic illustration of multilayer modulation used in the Chu and Barnett calculation where the interface composition and modulus gradient vary in a constant stepwise gradient: (a) trapezoidal modulations for large period; (b) sawtooth modulations for small periods.*

In general, hardening mechanism studies are conducted on the isostructural transition-metal nitrides, e.g. TiN, VN, CrN, NbN, and as all layers for a given Λ have the same structure, dislocations can easily cross layers. The multilayer hardening mechanism was studied by

* Reprinted from "X. Chu and S. A. Barnett, J. Appl. Phys., 1995, 77, 4404." with the permission of AIP Publishing. Copyright (2016).

Barnett and his research team, including the supermodulus effect [38], dislocation blocking [39] and the mismatch lattice strain effect [40]. From these studies, it was concluded that the difference in shear modulus of the component layers is the key factor, rather than mismatch of the lattice parameter or supermodulus effect.

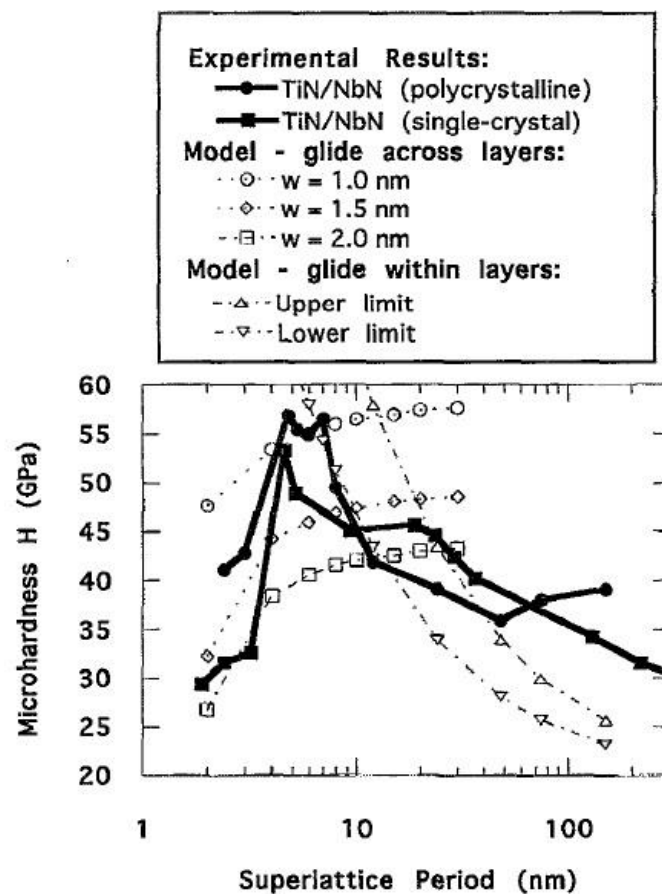


Figure 2.8 The predicted hardness obtained by combining models of dislocation gliding in and across TiN/NbN layers compared with measured hardness*.

The hardness enhancement in multilayers arises when dislocation movement is blocked by a strain field derived from the different line energy in each layer. The line energy difference strongly correlates with

* Reprinted from [39] X. Chu and S. A. Barnett, *J. Appl. Phys.*, **1995**, 77, 4403-4411. with the permission of AIP Publishing. Copyright (2016).

composition modulation [39]. Figure 2.7 shows a sawtooth and a trapezoidal composition modulation. Based on the two models, Chu and Barnett [39] calculated the stress required for dislocation glide across interfaces and found with increasing period Λ the hardness was enhanced to a saturated value (Figure 2.8). The key drivers of hardness enhancement include layer miscibility (interface width) and the shear modulus difference. Moreover, the stress to move a dislocation within individual layers was calculated based on a model built by Sevillano [41]. The dislocation sliding in layers are operative at large period (over 10 nm) and hardness decreases when Λ is further increased. The two dislocation motions were combined in their study and found to agree with experiment. In conclusion, the hardness enhancement in nano-scale multilayer films depends on the shear modulus difference of component layers, the period and the interface width.

(b) *Nanocrystalline / intergranular phase composite coatings.* Nanocomposites with enhanced hardness are characterized as a mixture of one or two nanocrystalline (nc) phases and another X-ray amorphous (a) phase. In fact, the X-ray amorphous phase content could be below the X-ray diffraction lower limit of detection. Therefore, HRTEM is necessary to determine if the second phase is crystalline or amorphous. Various elemental combinations with such structures have been studied, e.g. nc-TiN/a-Si₃N₄ [42, 43], nc-ZrN/a-Cu [44], nc-TiC/a-C [5] and nc-TiC/a-TiB₂ [45]. These coatings were prepared by chemical vapor deposition (CVD) or PVD. The CVD films attain a hardness > 100 GPa, high elasticity (> 10% reversible strain) and high thermal stability ($\geq 1100^\circ\text{C}$). However, the CVD technique is difficult to scale-up, so PVD including vacuum arc evaporation and magnetron sputtering deposition [46, 47] have been employed to deposit industrial nanocomposite coatings, such as Ti-Al-N or Cr-Al-N combined with Si₃N₄.

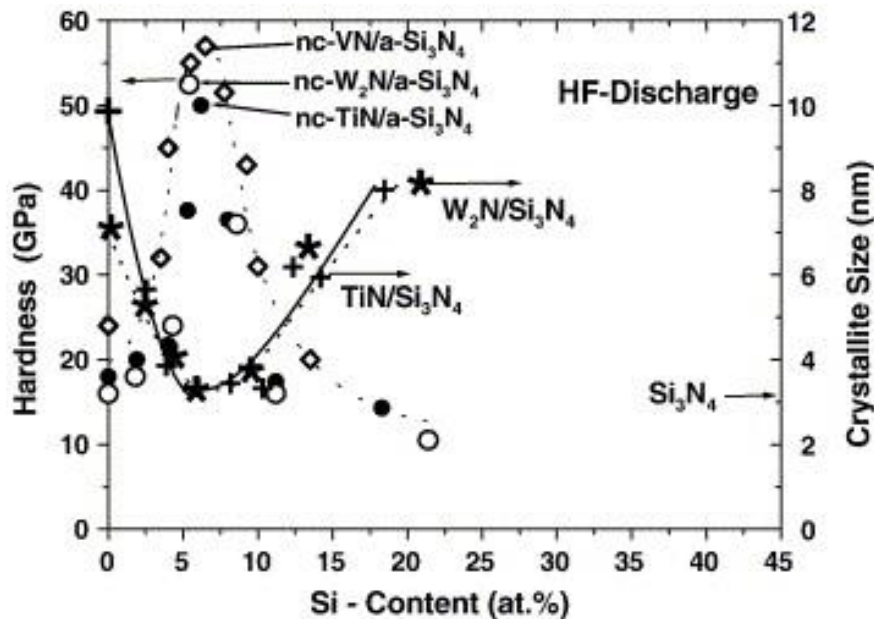


Figure 2.9 Relationship of hardness versus Si content and of the crystallite size versus Si content of nc-Metal Nitride/a-Si₃N₄ nanocomposites deposited under low-energy ion bombardment plasma assisted CVD*.

The hardness and crystal size of several nc-metal nitride/a-Si₃N₄ nanocomposite coatings versus Si-content are shown in Figure 2.9. To a large extent Si content affects the coating microstructure and mechanical properties. Ti-Si-N is the most studied system, and the progressive introduction of Si first increases the hardness and then at higher concentration decreases hardness, such that there is an inverse relationship to crystal size. According to *ab initio* density functional theory [48] the structure of 3 to 4 nm randomly oriented crystallites, connected by a one monolayer thick Si₃N₄ interface, has unique mechanical properties [49]. The hardness enhanced composite structure of small crystallites and sharp interfaces is generated by thermodynamic spinodal decomposition [50]. The fine size of the crystallites can endure

* Reprinted from Surface and Coating technology, Vol.201, Stan Veprek, Maritza G.J. Veprek-Heijman, The formation and role of interfaces in superhard nc-Me_nN/a-Si₃N₄ nanocomposites, Pages No.6065, Copyright (2016), with permission from Elsevier.

elastic deformation, while the random crystal orientation avoids dislocation sliding along the weakest slip planes. The characteristic nanocomposite structure is a 1 monolayer SiN_x interface which blocks dislocations crossing crystals. The rigid nature can be ascribed to the nearby TiN valence charge. Veprek [51] clarified that in hard Ti-Si-N coatings the interface thickness is about 0.3 to 0.5 nm instead of 1 to 2 nm which would result in weak grain boundaries. Therefore, it is advantageous to use HRTEM, especially aberration corrected transmission electron microscopy (TEM) for structure characterization to realize better controlled deposition processes.

2.3 TiN-based ternary and quasi-ternary coatings

This section describes the phase stability of selected ternary and quaternary coating systems, including Ti-Al-N, yttrium incorporated in Ti-Al-N-Y, and Ti-Si-N.

2.3.1 Ti-Al-N and Ti-Al-Y-N

Compared to TiN, Ti-Al-N possesses superior oxidation resistance and improved cutting performance at elevated temperature. However, as AlN adopts the hexagonal wurtzite structure it is only slightly miscible with TiN that possesses the rock-salt face-centred cubic (fcc) structure [52]. Using PVD and CVD the $\text{Ti}_{1-x}\text{Al}_x\text{N}$ metastable rock-salt structure could be realized for $x \leq 0.5-0.8$ [53-55], beyond which the coating consists of the cubic and hexagonal phases. Moreover, Ti-Al-N coating decomposes to fcc Ti-Al-N or TiN and wurtzite AlN above 1000°C [55]. The Ti-Al-N solid solution contributes intrinsic strain due to atomic radius difference between Ti and Al, thus leading to enhanced hardness.

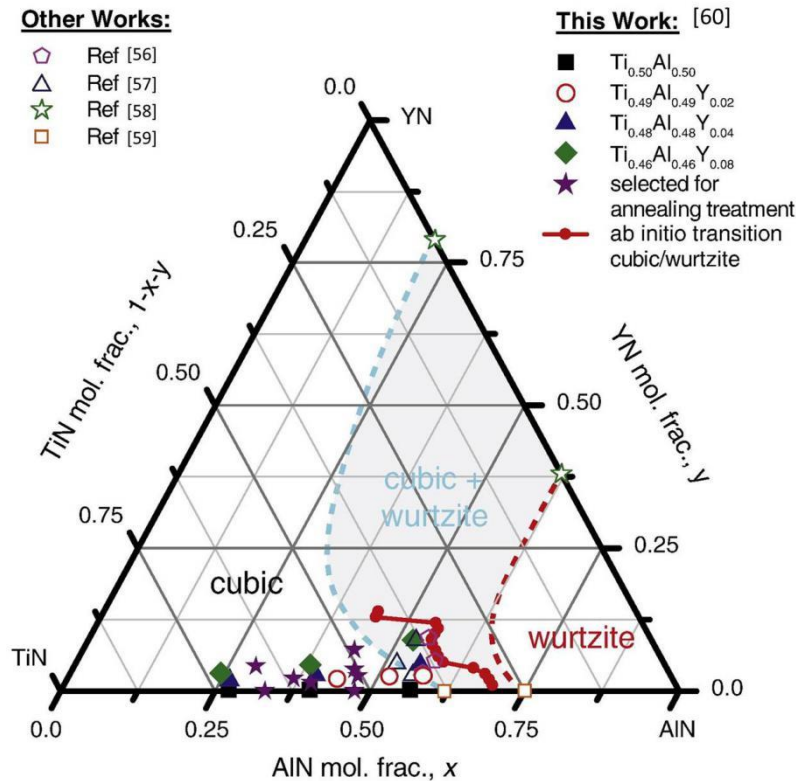


Figure 2.10 The phase diagram of as-deposited TiN-YN-AlN quasi-ternary film*.

Adding yttrium to cubic Ti-Al-N creates an age-hardening effect with improved corrosion and oxidation resistance, because the large size and electronic configuration of Y modify the Ti-Al-N microstructure by introducing misfit lattice strain and changing the bond status in the cubic structure. Generally, PVD Ti-Al-Y-N coatings are deposited using Ti-Al-Y alloy targets, with Y content controlled by the alloy target composition. However, if Y content is high in Ti-Al-Y-N then the AlN wurtzite phase is favoured and mechanical properties deteriorate with wurtzite present, especially for Al atomic fraction > 0.5. Riedl et al. [56] have summarized the experimental and calculated results [57-60] to prepare a quasi-ternary phase diagram of TiN-YN-AlN (Figure 2.10). According to their work, the saturated cubic Ti-Al-Y-N solid solution would be

* Reprinted from Surface and Coating technology, Vol.235 H. Riedl, D. Holec, R. Rachbauer, P. Polcik, R. Hollerweger, J. Paulitsch, Paul H. Mayrhofer, Phase stability, mechanical properties and thermal stability of Y alloyed Ti-Al-N coatings, Pages No.176, Copyright (2016), with permission from Elsevier.

less stable, with the wurzite structure generated, if Y content exceeds a critical value around 2 at% - 9 at% of total cations depending on the Al to Ti ratio. Moreover, Y incorporation in Ti-Al-Y-N could lower the AlN solid solubility in the cubic structure, resulting in wurtzite co-existing with the cubic structure. According to the *ab initio* calculations of Moser and Mayrhofer [58], 12.5 at% Y will reduce AlN solubility in cubic $Ti_{1-x}Al_xN$ by ~23%, from $x=0.69$ to $x=0.56$. Because Y has high affinity to oxygen, it has a tendency to segregate to grain boundaries where oxygen impregnates and form oxides, which blocks oxygen diffusion and prevents oxidation of other cations [61]. It has been reported that adding 1 at% yttrium in $Ti_{0.45}Al_{0.54}Y_{0.01}N$ decreased oxide thickness from 4.9 μm to 3.1 μm after annealing at 900°C for 210 min. Simultaneously, the $Ti_{0.45}Al_{0.54}Y_{0.01}N$ monolayer coating hardness improved by 24% compared to $Ti_{0.45}Al_{0.55}N$ [62].

2.3.2 Ti-Si-N

TiN and Si_3N_4 are immiscible when the nitrides are stoichiometric and free of impurities [63]. The phase segregation of Ti-Si-N into TiN and Si_3N_4 is through spinodal decomposition. Zhang et al. [64] calculated and plotted the Gibbs free energy by mixing TiN and Si_3N_4 under different nitrogen pressures at 873 K (Figure 2.11). TiN is of the rock-salt type while Si_3N_4 is a hexagonal close packed (hcp) structure. It was concluded that the energy to decompose the two phases is very large, especially when the Si_3N_4 fraction is around 15-20 %. Any fluctuation of the Si_3N_4 composition will reduce the Gibbs free energy, indicating that the decomposition of Ti-Si-N will spontaneously form a composite consisting of uniform and randomly distributed TiN crystallites and intergranular Si_3N_4 with sharp interfaces. The tendency of phase segregation in Ti-Si-N with a demixing energy of 300 - 400 kJ / mol is much stronger compared to Ti-Al-N with ~30 kJ / mol [65]. The nitrogen pressure is critical for Ti-Si-N decomposition as higher pressures increase the decomposition

energy, promoting the demixing process. Besides, Zhang et al. [66] pointed out that oxygen would result in Si stabilization in the Ti-Si-N solid solution which enlarges crystal size and modifies crystal orientations, that prove detrimental to formation of the nanocomposite structure.

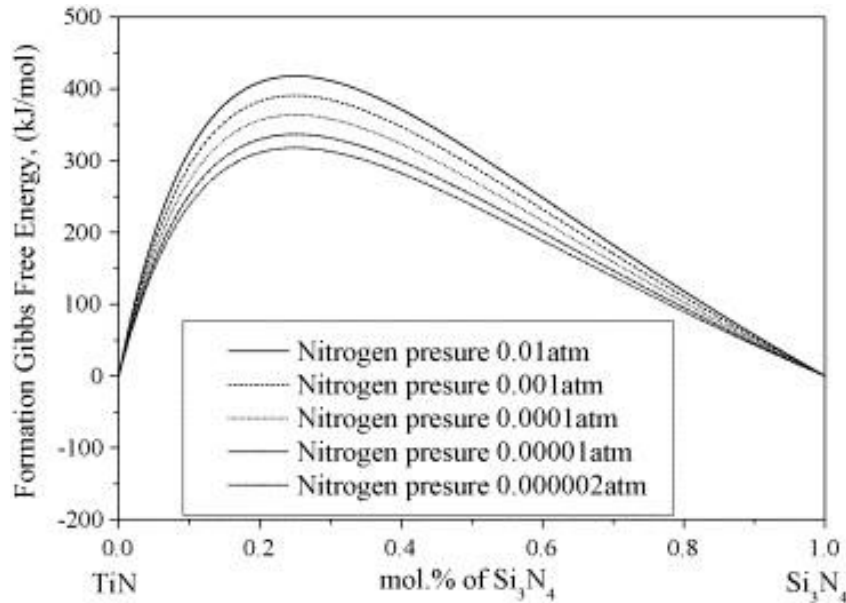


Figure 2.11 Gibbs free energy of mixing in the TiN and Si_3N_4 system at a temperature of 873 K in a nitrogen atmosphere as a function of pressures (stoichiometric TiN and Si_3N_4 as reference state)*

2.4 Thesis questions arising from the literature review

In this thesis, the chemical composition and structure modulation of TiN-based films will be adjusted to fabricate nanocomposite coatings by PVD and study the relationship among processing, structure and properties. Although various nitride coating systems have been widely studied, and applied as protective coatings in industry, many new systems are proposed and this research work is ongoing. Consequently, systematic investigations that include conceptual

* Reprinted from Materials Science and Engineering: A, Vol.424 R.F. Zhang, S. Veprek, On the spinodal nature of the phase segregation and formation of stable nanostructure in the Ti-Si-N system, Pages No.134, Copyright (2016), with permission from Elsevier.

design, process parameter regulation, structural characterization and property analysis are essential to compare and contrast deposition strategies. In such integrative studies, structural and crystallographic understanding is often inadequate. For example, Ti-Si-N is a well studied system, and based on calculation, an optimised structure has been proposed with 3-4 nm nanocrystallites randomly distributed and separated by a single monolayer of Si_3N_4 . However, the deposited coatings could be inconsistent with the model due to the lack of interface characterization. Another example is Ti-Al-N where according to various calculations, the interface width and the layer composition modulation are the principle hardening factors, but this is yet to be confirmed through experiments. Furthermore, for industrial applications the coatings should work efficiently under high speed friction and display good mechanical properties at both room temperature and high temperature. Finally, a comprehensive approach should also improve oxidation resistance in addition to hardness and wear resistance. This can be achieved by adding a reactive element, yttrium, to the nanolayered structure due to its segregation tendency to grain boundaries and high affinity to oxygen, which block the oxygen diffusions. Such films can be fabricated from the pure Y target in a rotating substrate system to incorporate Y in Ti-Al-N multilayers, rather than using Ti-Al-Y alloy as commonly employed [60, 62, 67]. This approach offers greater flexibility to control Y distribution and lowers cost. Ti-Si-N properties will be also examined at high temperature. In subsequent Chapters, structure and behaviour will be correlated with processing parameters using either single or hybrid deposition methods. This thesis systematically links processing and fabrication to microstructure and microchemistry, that jointly dictate properties. Finally, further avenues for modifying coating design concepts will be considered.

References:

- [1] H. E. Rebenne and D. G. Bhat, *Surf. Coat. Technol.*, **1994**, 63, 1-13.

- [2] S. PalDey and S. C. Deevi, *Materials Science and Engineering: A*, **2003**, 342, 58-79.
- [3] A. D. Pogrebnyak, A. P. Shpak, N. A. Azarenkov and V. M. Beresnev, *Physics-Uspekhi*, **2009**, 52, 29-54.
- [4] H. Holleck, *J. Vac. Sci. Technol., A*, **1986**, 4, 2661-2669.
- [5] A. A. Voevodin and J. S. Zabinski, *Diamond Relat. Mater.*, **1998**, 7, 463-467.
- [6] S. V. Hainsworth, H. Sjöström, T. F. Page and J.-E. Sundgren, *MRS Online Proceedings Library Archive*, **1996**, 436, 275.
- [7] S. Chol, *ASME-Publications-Fed*, **1995**, 231, 99-106.
- [8] S. B. Qadri, E. F. Skelton, D. Hsu, A. D. Dinsmore, J. Yang, H. F. Gray and B. R. Ratna, *Physical Review B*, **1999**, 60, 9191-9193.
- [9] J. Schiotz, F. D. Di Tolla and K. W. Jacobsen, *Nature*, **1998**, 391, 561-563.
- [10] A. Tschöpe, *Solid State Ionics*, **2001**, 139, 267-280.
- [11] G. Herzer, *IEEE Transactions on Magnetics*, **1990**, 26, 1397-1402.
- [12] D. M. Mattox, *Metal Finishing*, **2002**, 100, 394-408.
- [13] M. Nordin, M. Larsson and S. Hogmark, *Surf. Coat. Technol.*, **1998**, 106, 234-241.
- [14] J. H. Park, W. S. Chung, Y.-R. Cho and K. H. Kim, *Surf. Coat. Technol.*, **2004**, 188, 425-430.
- [15] D.-Y. Wang and K.-W. Weng, *Surf. Coat. Technol.*, **2002**, 156, 195-200.
- [16] P. H. Mayrhofer, F. Kunc, J. Musil and C. Mitterer, *Thin Solid Films*, **2002**, 415, 151-159.
- [17] D. M. Marsh, *Proceedings of the Royal Society of London. Series A, Mathematical and Physical Sciences*, **1964**, 282, 33-43.
- [18] T. A. Parthasarathy, S. I. Rao, D. M. Dimiduk, M. D. Uchic and D. R. Trinkle, *Scripta Mater.*, **2007**, 56, 313-316.
- [19] E. Hall, *Proceedings of the Physical Society. Section B*, **1951**, 64, 747.
- [20] N. Petch, *J. Iron Steel Inst.*, **1953**, 174, 25-28.

- [21] R. W. Siegel and G. E. Fougere, *Nanostruct. Mater.*, **1995**, 6, 205-216.
- [22] E. Arzt, *Acta Mater.*, **1998**, 46, 5611-5626.
- [23] J. Musil, *Surf. Coat. Technol.*, **2012**, 207, 50-65.
- [24] D. Mattox, *J. Vac. Sci. Technol., A*, **1989**, 7, 1105-1114.
- [25] W. Ensinger, *Nuclear Instruments and Methods in Physics Research Section B: Beam Interactions with Materials and Atoms*, **1997**, 127, 796-808.
- [26] I. Petrov, L. Hultman, U. Helmersson, J. E. Sundgren and J. E. Greene, *Thin Solid Films*, **1989**, 169, 299-314.
- [27] L. Hultman, G. Håkansson, U. Wahlström, J. E. Sundgren, I. Petrov, F. Adibi and J. E. Greene, *Thin Solid Films*, **1991**, 205, 153-164.
- [28] F. d'Heurle, *Metallurgical and Materials Transactions B*, **1970**, 1, 725-732.
- [29] F. Lomello, F. Sanchette, F. Schuster, M. Tabarant and A. Billard, *Surf. Coat. Technol.*, **2013**, 224, 77-81.
- [30] H. Windischmann, *Critical Reviews in Solid State and Material Sciences*, **1992**, 17, 547-596.
- [31] X. Wan, S. Zhao, Y. Yang, J. Gong and C. Sun, *Surf. Coat. Technol.*, **2010**, 204, 1800-1810.
- [32] P. Mayrhofer, G. Tischler and C. Mitterer, *Surf. Coat. Technol.*, **2001**, 142, 78-84.
- [33] H.-M. Tung, J.-H. Huang, D.-G. Tsai, C.-F. Ai and G.-P. Yu, *Materials Science and Engineering: A*, **2009**, 500, 104-108.
- [34] Z. B. Qi, P. Sun, F. P. Zhu, Z. C. Wang, D. L. Peng and C. H. Wu, *Surf. Coat. Technol.*, **2011**, 205, 3692-3697.
- [35] J. Eshelby, F. Frank and F. Nabarro, *The London, Edinburgh, and Dublin Philosophical Magazine and Journal of Science*, **1951**, 42, 351-364.
- [36] J. C. Li, *Transactions of the Metallurgical Society of AIME*, **1963**, 227, 239-&.

- [37] M. Shinn, L. Hultman and S. A. Barnett, *J. Mater. Res.*, **1992**, 7, 901-911.
- [38] P. B. Mirkarimi, M. Shinn, S. A. Barnett, S. Kumar and M. Grimsditch, *J. Appl. Phys.*, **1992**, 71, 4955-4958.
- [39] X. Chu and S. A. Barnett, *J. Appl. Phys.*, **1995**, 77, 4403-4411.
- [40] P. Mirkarimi, S. Barnett, K. M. Hubbard, T. Jervis and L. Hultman, *J. Mater. Res.*, **1994**, 9, 1456-1467.
- [41] J. Gil Sevillano, P. van Houtte and E. Aernoudt, *Prog. Mater Sci.*, **1980**, 25, 69-134.
- [42] L. Shizhi, S. Yulong and P. Hongrui, *Plasma Chem. Plasma Process.*, **1992**, 12, 287-297.
- [43] S. Vepřek, S. Reiprich and L. Shizhi, *Appl. Phys. Lett.*, **1995**, 66, 2640-2642.
- [44] J. Musil, P. Zeman, H. Hrubý and P. H. Mayrhofer, *Surf. Coat. Technol.*, **1999**, 120–121, 179-183.
- [45] C. Mitterer, P. H. Mayrhofer, M. Beschliesser, P. Losbichler, P. Warbichler, F. Hofer, P. N. Gibson, W. Gissler, H. Hruby, J. Musil and J. Vlček, *Surf. Coat. Technol.*, **1999**, 120–121, 405-411.
- [46] M. Jilek, T. Cselle, P. Holubar, M. Morstein, M. G. J. Veprek-Heijman and S. Veprek, *Plasma Chem. Plasma Process.*, **2004**, 24, 493-510.
- [47] S. Veprek and M. J. G. Veprek-Heijman, *Surf. Coat. Technol.*, **2008**, 202, 5063-5073.
- [48] X. Hu, H. Zhang, J. Dai, G. Li and M. Gu, *J. Vac. Sci. Technol., A*, **2005**, 23, 114-117.
- [49] S. Vepřek and S. Reiprich, *Thin Solid Films*, **1995**, 268, 64-71.
- [50] R. Zhang and S. Veprek, *Thin Solid Films*, **2008**, 516, 2264-2275.
- [51] S. Veprek, *Journal of nanoscience and nanotechnology*, **2011**, 11, 14-35.
- [52] J. C. Schuster and J. Bauer, *J. Solid State Chem.*, **1984**, 53, 260-265.
- [53] T. Ikeda and H. Satoh, *Thin Solid Films*, **1991**, 195, 99-110.

- [54] Y. Tanaka, T. M. Gür, M. Kelly, S. B. Hagstrom and T. Ikeda, *Thin Solid Films*, **1993**, 228, 238-241.
- [55] S. H. Lee, B. J. Kim, H. H. Kim and J. J. Lee, *J. Appl. Phys.*, **1996**, 80, 1469-1473.
- [56] H. Riedl, D. Holec, R. Rachbauer, P. Polcik, R. Hollerweger, J. Paulitsch and P. H. Mayrhofer, *Surf. Coat. Technol.*, **2013**, 235, 174-180.
- [57] R. Rachbauer, D. Holec, M. Lattemann, L. Hultman and P. H. Mayrhofer, *International Journal of Materials Research*, **2011**, 102, 735-742.
- [58] M. Moser and P. H. Mayrhofer, *Scripta Mater.*, **2007**, 57, 357-360.
- [59] L. Wang, *Influence of Al on structure and mechanical properties of YN and HfN*, na, 2011.
- [60] M. Moser, D. Kiener, C. Scheu and P. H. Mayrhofer, *Materials*, **2010**, 3, 1573.
- [61] H. M. Tawancy, N. M. Abbas and A. Bennett, *Surf. Coat. Technol.*, **1994**, 68, 10-16.
- [62] L. Zhu, Y. Zhang, W. Ni and Y. Liu, *Surf. Coat. Technol.*, **2013**, 214, 53-58.
- [63] P. Rogl and J. C. Schuster, *Phase diagrams of ternary boron nitride and silicon nitride systems*, Asm Intl, 1992.
- [64] R. Zhang and S. Veprek, *Materials Science and Engineering: A*, **2006**, 424, 128-137.
- [65] R. Zhang and S. Veprek, *Materials Science and Engineering: A*, **2007**, 448, 111-119.
- [66] R. F. Zhang and S. Veprek, *Physical Review B*, **2007**, 76, 174105.
- [67] M. Moser and P. Mayrhofer, *Scripta Mater.*, **2007**, 57, 357-360.

Chapter 3

Experimental methodology

Establishing the correlation among processing, structure and properties of nanocomposite hard coatings requires careful design of experimental protocols. This chapter summarizes the principles and methodology of physical vapor deposition techniques, including cathodic arc deposition and high power impulse magnetron sputtering, to rationally select the most appropriate processing for a specific coating system. Through comprehensive characterization, the nature of the nanocomposite is more completely described, which facilitates deeper understanding of the structural and crystallochemical influences on coating performance. Through experimental integration, the evaluation of films is less ambiguous and can guide superior fabrication control for enhanced functionality.

3.1 Rationale of selected experiment methods

The objective of this research is to deposit and analyze physical vapor deposition (PVD) nanocomposite coatings used in extreme conditions, including high temperature and high speed friction. PVD techniques allow vapor condensation on substrates at low temperature and are employed for sample synthesis. On one hand, for nanomultilayer Ti-Al-N and Ti-Al-Y-N coatings with superlattice structures, the depositions are completed in an instrument equipped with three cathodic arc powered targets and one direct current (DC) - magnetron sputtering target which can be used to dope non-conductive or brittle materials. This instrument is coupled with a rotating substrate holder on which bias is applied to enhance ion bombardment. The holder also controls the multi-layer period, a key parameter to modulate the structure and composition of the coatings. On the other hand, high power impulse magnetron sputtering (HiPIMS) suitable for depositing dense coatings, is employed for the fabrication of Ti-Si-N composites in a nanocrystallite/amorphous structure. HiPIMS can uniquely yield Ti-Si-N nanocomposites with a dense isotropic morphology instead of the familiar columnar structure. In this manner, coating toughness is improved and large scale defects are reduced.

The coating analysis is divided into structural and crystallochemical characterizations and property examinations. For structural interrogation, X-ray diffraction (XRD) and transmission electron microscopy (TEM) were the principle tools. XRD can efficiently evaluate coating texture from a large area while TEM allows direct observation of crystal growth, grain boundaries and interfaces. Moreover, the cross-sectional structures can be observed using TEM, which is highly informative for examining columnar grains that are common in PVD coatings. Coating property analysis related to industrial demands is preferred. The coatings will be deposited on high-speed machining tools and

thus the hardness, wear resistance and oxidation resistance are key features for examination. The coatings are deposited on high speed steel with a thickness below 5 micron. Nanoindentation is used to measure the hardness and Young's modulus by penetrating several hundred nanometers. Care is required to exclude substrate hardness from affecting the results. As for wear resistance, ball-on-disk tests are employed to represent the tribological behaviours during cutting. Together with post-examination of wear scars by a profilometer the wear rate can be calculated. The oxidation resistance is characterized by heating the samples in air to at least 800°C which is close to the extreme conditions in industrial applications. The structure evolution at elevated temperature can be revealed by XRD of the annealed samples.

3.2 Hard coatings deposited by PVD

3.2.1 Cathodic arc deposition (CAD)

CAD is widely used in industry to produce coatings with good adherence and controlled composition modulation and performance. It utilizes an electric discharge to vaporize source materials from the cathode in a low pressure (around 10^{-3} Pa) chamber and the vapor is deposited on the substrates with or without a bias.

The cathode source is called the target and during deposition no carrier gas is needed. The general layout of a CAD system comprises the vacuum chamber containing targets and substrate holders. The chamber is evacuated to 10^{-4} Pa before deposition. The targets are supplied with a low voltage and high current power supply and equipped with a cooling system. A high DC or pulsed voltage supply is applied to the substrate holders as shown schematically in Figure 3.1. In the image, a three-fold rotation substrate holder is used to coat entirely substrates with complex shapes.

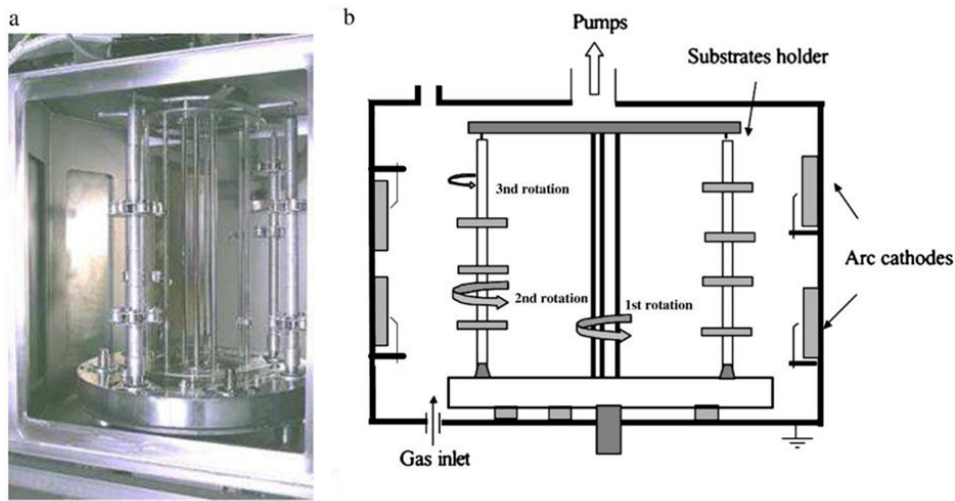


Figure 3.1 CAD system photo (a) and schematic drawing (b).*

The arc is started by disconnecting the trigger and the target which has a negative potential of around several tens of volts. Theoretically, electron emission resulting from field emission and thermionic effects, is discrete on the cathode. Intense emitted electrons from these discrete spots collide with the target atoms inelastically and induce positive metallic ions. These cathode spots are about 10 to 100 μm in diameter as determined by a speed camera [1, 2]. The current densities of these spots are related to cathode current and target materials, which are between 10^8 to 10^{11} A / m^2 . Carrying high energy and intense electron emission these cathode spots move across the target surface under the control of a magnetic field [3]. The ions from inelastic collisions aggregate around the target surface as electrons under magnetic force drift more quickly and generate a relative positive potential barrier slowing down electrons and accelerating ions. Around 10 % of the ions are accelerated back to cathode and initiate new cathode spots. The remaining ions move towards the substrate by bombardment. The arc evaporation process is shown in Figure 3.2.

*Reprinted from Surface and Coating technology, Vol.205, F. Sanchettec, C. Ducros, T. Schmitt, P. Steyer, A. Billard, Nanostructured hard coatings deposited by cathodic arc deposition: From concepts to applications, Pages No.5445, Copyright (2016), with permission from Elsevier.

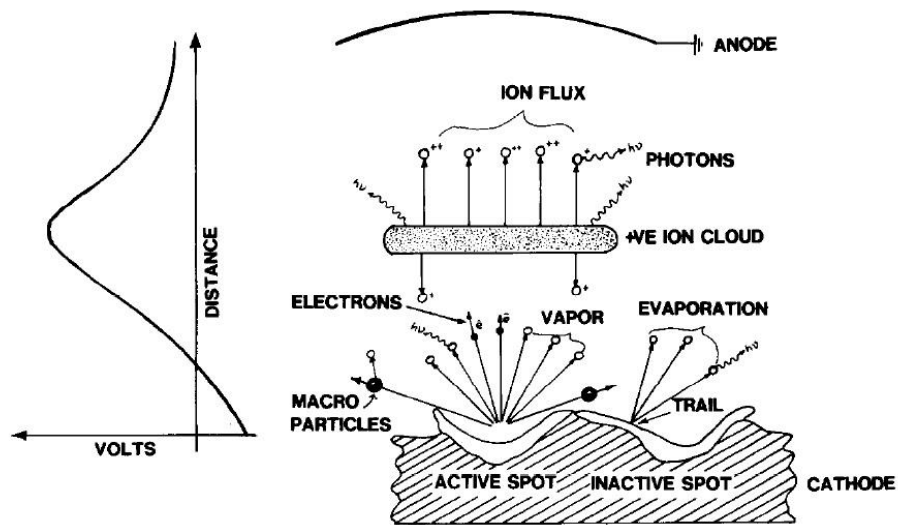


Figure 3.2 Target material emissions from cathode spots.*

The vapor from the cathode is a mixture of ions, electrons, neutral particles and metallic microdroplets. Reportedly over 95% of evaporated particles are ionized. The ejection speed is between 10^3 to 10^4 m/s and the particle density around the target ranges from 10^{17} to 10^{19} / cm^{-3} [4, 5]. Thus, the ion speed is of the order of 10^4 m/s and carrying energy around 20-200 eV which is highly dependant on the target material melting point. In general, the ion energy from arc evaporation is higher than produced during magnetron sputtering and electron beam evaporation.

The main limitation of the CAD technique is the creation of metal droplets (0.1 - 10 μm) during evaporation that are generated by the arc collision with the target or by ejection under the high pressure plasma [6-8]. These droplets are coating defects but can be reduced by increasing the bias voltage [9], strengthening the magnetic field leading to cathode spots moving more rapidly [10], or employing a filter to separate microdroplets from the ion flux [11, 12].

* Reprinted from Thin Solid Films, Vol.153, P.J. Martin, D.R. McKenzie, R.P. Netterfield, P. Swift, S.W. Filipczuk, K.H. Müller, C.G. Pacey, B. James, Characteristics of titanium arc evaporation processes, Pages No.92, Copyright (2016), with permission from Elsevier.

In this work, CAD was used to deposit multilayer transition metal nitrides, with pure metal targets providing the metallic ions and nitrogen injected into the chamber simultaneously. Higher bias voltage, e.g. -800 V, was applied to the substrate holders to allow ion etching before deposition. The bias voltage is a principle parameter to control ion bombardment on the substrate, which in turn, controls the mechanical properties of the coatings. When layering two nitrides, the key parameter affecting coating performance is the substrate holder rotation speed which controls the multilayer period. The adjustment of those parameters will be discussed further in the following Chapters.

3.2.2 High power impulse magnetron sputtering

HiPIMS is another PVD deposition method that differs from CAD through the use of magnetron sputtering where an inert gas is ionized and accelerated in an electrical field to sputter source material from the targets. Sputtered ions are partially magnetically trapped on the target surface to enhance ionization efficiency, while the remainder bombard and condensate on the biased substrates. Normally, the film growth is non-equilibrium so the coating structure, electrical properties and mechanical characteristics are closely related to the deposition parameters, especially the plasma energy and flux. In conventional magnetron sputtering, the ionization degree and deposition rate are relatively low. To improve deposition efficiency requires high bias on the substrate to increase plasma energy, but drawbacks include inert gas ion implantation, high residual stress and poor adhesion. Nonetheless, increasing the flux of sputtered ions significantly improves film quality. During the 1990s, target power supplies changed from conventional DC sputtering to the high power impulse mode that substantially increased the plasma density. For example, in a copper target ion flux increased by 2 orders of magnitude to 10^{18} m^{-3} and the ionization yield reached 70% of the total sputtered species [13]. The plasma charge density for a variety of processes is summarized in Figure 3.3.

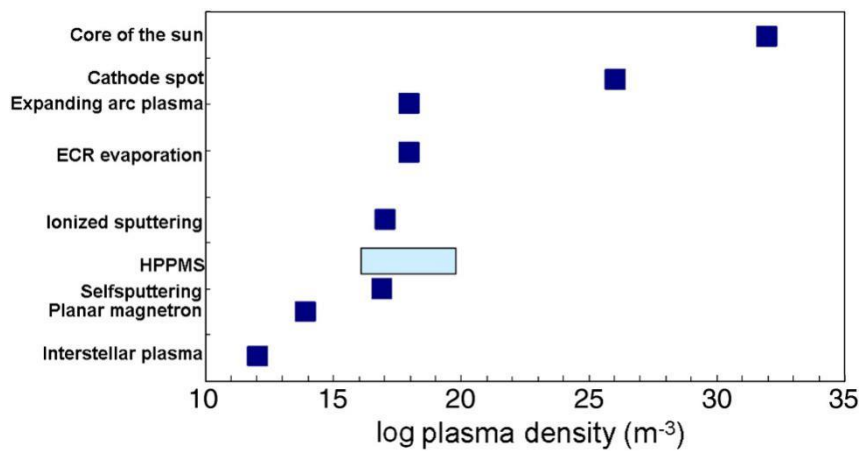


Figure 3.3 Comparison of plasma densities in nature and materials processing (HPPMS is HiPIMS; the abbreviation ECR is Electron Cyclotron Resonance).*

The implementation of HiPIMS requires the application of a high power density pulse on the targets and simultaneously keeping the average power density low to avoid overheating targets and magnets. The power supply device is illustrated in Figure 3.4. A capacitor in the pulsing unit linked to a DC power supply stores several hundreds to several thousands of charging volts, that is pulsed with defined width and frequency in the micron second range. In HiPIMS, the pulse of power-on time can range from 5 to 5000 μ s and the frequency from 10 Hz to 10 kHz. In each pulse there are four stages including electrical breakdown, the formation of gas plasma, generation of metal plasma, and a steady state where the metal plasma is dominant rather than the gas plasma. Simultaneously, electrons are accelerated and escape from the area close to the cathode only a few microseconds after the pulse starts [14], indicating efficient electron heating in the HiPIMS mode.

* Reprinted from Surface and Coatings Technology, Vol.204, K. Sarakinos, , J. Alami, S. Konstantinidis, High power pulsed magnetron sputtering: A review on scientific and engineering state of the art, Pages No.1665, Copyright (2016), with permission from Elsevier.

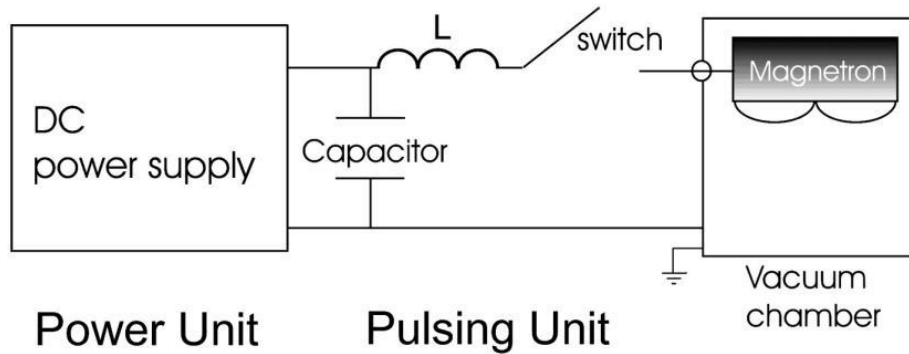


Figure 3.4 The HiPIMS power supply device.*

In HiPIMS, the plasma properties are related to the power pulse on/off time, average target current and target peak current. For example, maintaining the average power and increasing the power on time from 5 to 20 μs , the dominant plasma changed from an inert gas plasma to metal plasma [15], indicating that longer power on time results in a higher ionization rate. Moreover, maintaining the average power and increasing the power off time enhanced the peak target current, leading to ionized metal being the primary sputtered species [16]. However, the arc of a sputtering process is more pronounced as HiPIMS adopts a high frequency and high power pulse. To moderate this problem a short power-on time of 5 – 20 μs can be employed as the discharge is still in a transient region before transferring to the arc [17]. By coordinating these parameters plasma properties can be tailored to optimize film quantity.

Controlling the plasma permits interface engineering. First, metal ions can be used for etching the substrate to enhance adhesion between the film and substrate. Subsequent HiPIMS deposition can facilitate coating densification, and surface smoothing due to the higher plasma ionization and metal ion density. Moreover, HiPIMS can induce renucleation and generate nanosized equiaxed grains. In this thesis, a system combining DC-pulsed magnetron

* Reprinted from Surface and Coatings Technology, Vol.204, K. Sarakinos, , J. Alami, S. Konstantinidis, High power pulsed magnetron sputtering: A review on scientific and engineering state of the art, Pages No.1663, Copyright (2016), with permission from Elsevier.

sputtering and HiPIMS was employed to deposit Ti-Si-N monolayers as nanocrystalline/amorphous composites (Figure 3.5). The Ti target is sputtered in HiPIMS mode to fabricate TiN nanocrystallites, while a Si target powered by conventional DC-pulsed magnetron sputtering controlled Si content to optimize TiN crystal size. The substrate was operated in the one-fold rotation mode.

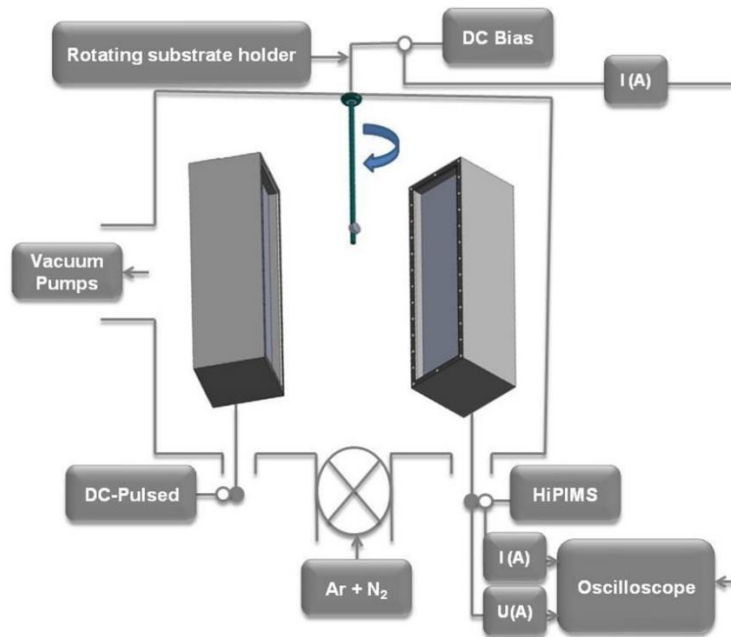


Figure 3.5 The deposition device hybridizing HiPIMS and dc magnetron sputtering.*

3.3 Characterization methods

3.3.1 X-ray diffraction (XRD)

X-ray diffraction was employed to characterize coating crystallography before and after high temperature oxidation. Diffraction only occurs at specific X-ray incident angles with respect to crystal orientation as described by Bragg's Law:

* Reprinted from Vacuum, Vol.109, M. Arab Pour Yazdi, F. Lomello, J. Wang, F. Sanchette, Z. Dong, T. White, Y. Wouters, F. Schuster, A. Billard, Properties of TiSiN coatings deposited by hybrid HiPIMS and pulsed-DC magnetron co-sputtering, Pages No.44, Copyright (2016), with permission from Elsevier.

$$\lambda = 2d \sin \theta \quad (3.1)$$

where θ , the incident angle is related to λ (Å), the X-ray wavelength, and d (Å), the interplanar spacing.

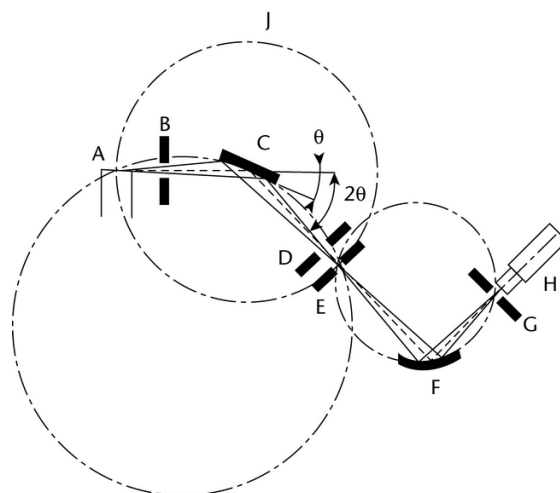


Figure 3.6 XRD Bragg-Brentano geometry. (A: X-ray source; B: divergence slit; C: sample stage; D: anti-diffusion slit; E: receiving slit; F: monochromator; G: detector receiving slit; H: detector; J: focusing circle) [18].

In randomly distributed polycrystals only those in appropriate orientations can satisfy the Bragg condition. In laboratory X-ray diffractometers accelerated electrons strike a metal target, usually copper and cobalt, to generate characteristic X-rays. The incident characteristic X-ray (typically only the K-family are used) are scattered from crystal planes with a small fraction satisfying Bragg's Law and the diffracted portion is detected by scintillation detectors as a function of angle. The width of the diffraction peaks is controlled to varying extents by crystal size, crystal strain, instrument broadening, and $K\alpha_1/K\alpha_2$ convolution. The diffracted beam intensity is influenced by the symmetry chemical composition, reflection multiplicity, crystal size and preferred orientation. In a powder diffractometer with Bragg-Brentano geometry the incident angle is defined between the X-ray source and the sample, while the diffracted angle is defined between the incident beam and the detector

angle (Figure 3.6). The incident angle is always half the detector angle 2θ . In the θ - θ mode the sample is fixed and both tube and detector rotates at same rate, while in the θ - 2θ mode the X-ray source is fixed and the detector rotates at twice the speed of sample tilt. Both modes were applied in this work and details are described in the following Chapters.

With Bragg-Brentano geometry the diffraction vector that bisects the angle between the incident and scattered beams is always perpendicular to the sample surface. For thin films, lattice planes parallel to the substrate surface show a higher possibility of detection. The predominance of particular lattice planes is referred to as preferred orientation or texture, and the intensity of textured reflection will differ from those observed in randomly oriented powders. In the following chapters, the coating texture is determined according to the Harris's inverse pole figure technique [19, 20] by a texture coefficient T^* calculated as:

$$T^*(hkl) = \frac{I(hkl)/R(hkl)}{(1/n) \sum_0^n I(hkl)/R(hkl)} \quad (3.2)$$

where $I(hkl)$ is the (hkl) reflection intensity, while $R(hkl)$ is the (hkl) intensity in a random powder specimen and n is the number of reflections evaluated. Higher $T^*(hkl)$ percentage suggest the coating is $\langle hkl \rangle$ textured.

The crystal size can be estimated by XRD. Smaller crystals result in peak broadening as there is less perfect destructive interference. The average crystallite size can be determined by the Scherrer equation:

$$D = \frac{0.9\lambda}{B \cos\theta} \quad (3.3)$$

where D (\AA) is the average crystal thickness normal to diffraction planes, λ (\AA) is the X-ray wavelength, B is the angle full width at half maxima (FWHM) in radians and θ is the Bragg angle in degree.

Finally, Bragg-Brentano geometry can be used to determine the superlattice multilayer period (Λ) because the reflection intensity is a convolution consisting of the atomic lattice spacing and the scattering factor from composition modulation. Therefore, the patterns include Bragg peaks and satellite peaks, that are equally spaced around the Bragg peak, with the Λ determined following the equation:

$$\sin\theta_{\pm} = \sin\theta_B \pm m_{th}\lambda/(2\Lambda) \quad (3.4)$$

where θ_B is the Bragg reflection in degree, θ_{\pm} is the position in degree of m_{th} order positive or negative satellite peaks around θ_B , λ (\AA) is X-ray wavelength, and Λ (\AA) is the multilayer period. The period estimated by this equation should be consistent with direct observations by transmission electron microscopy (TEM).

3.3.2 Scanning electron microscopy (SEM)

In SEM a focused electron probe is rastered over the material and a variety of signals detected and reconstructed to produce images. The signals include secondary electrons (SEs), backscattered electrons (BEs) and characteristic X-rays each with a unique electron-sample interaction volume (Figure 3.7). SEs are produced through inelastic scattering within a few nanometers from the specimen surface and possess energies from 2-50 eV and give information concerning sample surface morphology and topology. BEs are elastically reflected incident electrons whose intensity is proportional to the average atomic number of the probed volume. Such images contain composition information, but to be meaningful topological contributions have to be eliminated by fine polishing. Characteristic X-rays have discrete energies because they are emitted to conserve energy during the transition of quantised electrons to lower energy levels. As the quantised energy is element specific, energy dispersive X-ray spectroscopy (EDX) can examine sample composition qualitatively and quantitatively. In practice, a significant overvoltage is needed

to induce a high probability of X-ray emission and mirror polished samples are required for reliable quantitation. The quantitative analysis needs to correct detected X-ray intensity with respect to atomic number effects, X-ray absorption and secondary characteristic fluorescence. This technique has a lower limit of detection (LLD) of 1-5 wt% depending on characteristic X-ray energy.

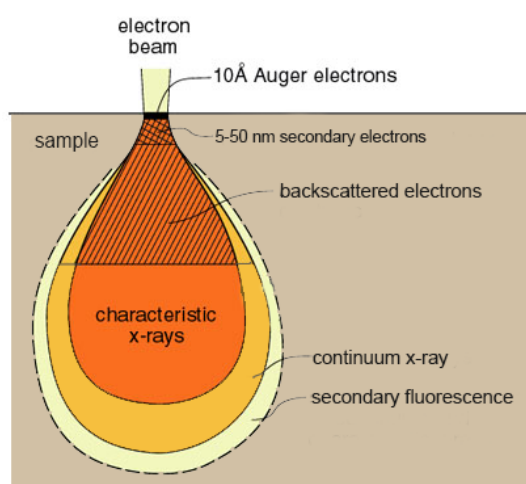


Figure 3.7 The sample-electron interaction volume and the corresponding depth where the different signals originate [21].

3.3.3 Transmission electron microscopy (TEM)

TEM produces images from the transmitted electrons. TEM is not simply a magnifying microscopy, but specifically uses subsets of diffracted electrons to produce images. Compared to X-rays (0.5-2.5 Å), electrons have much shorter wavelengths (0.0251 Å at 200 kV accelerating voltage). With small chromatic spread and low aberration optics highly coherent electron beams can be generated which allows direct observation of grain morphology, lattice spacings, grain boundaries and defects to a resolution down to 1 Å in certain imaging modes. TEM is based on the information extracted from the electron waves transmitted through samples, including electron beam amplitude and phase contrasts. For higher resolution imaging thinner samples and higher incident electron energies are required to reduce electron absorption.

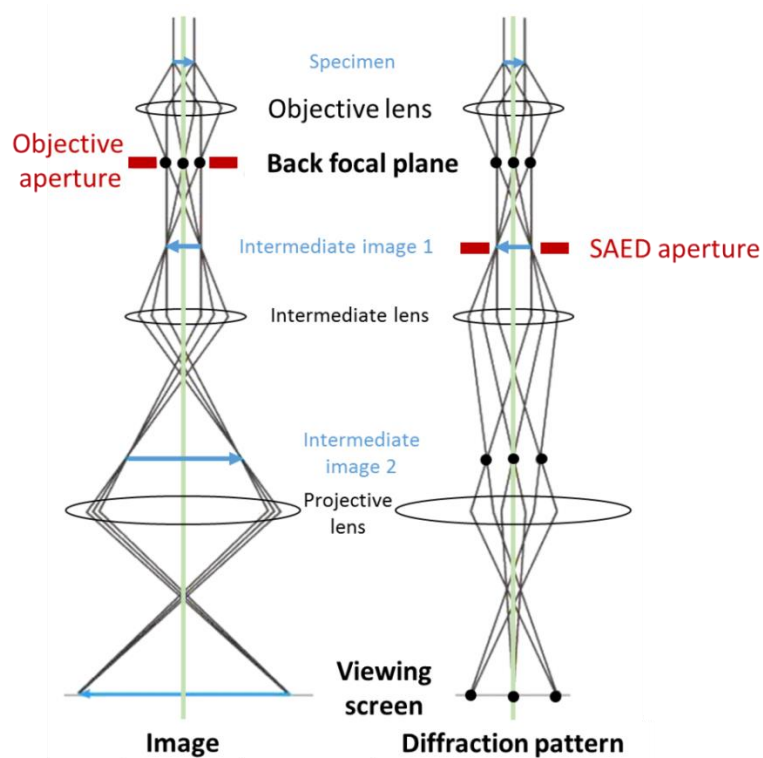


Figure 3.8 The two operations of a TEM imaging system: Imaging mode and diffraction mode [22].

Figure 3.8 shows the two principle modes of TEM operation. Scattered electrons from specimen pass through the objective lens, and generate a diffraction pattern in reciprocal space in the back focal plane that is combined in the image plane (Intermediate image 1). The imaging mode (real space image) can be selected by adjusting the strength of the intermediate lens to select the diffraction pattern or image to appear in the intermediate image 2 plane. In imaging mode, an objective aperture can be inserted in back focal plane to generate bright field (BF) or dark field (DF) image. BF imaging is a common operation mode in conventional TEM, where a small number of diffracted beams are allowed to pass through the objective aperture so that thinner regions, or areas of lower atomic number appear with bright contrast. DF imaging is based on the diffraction contrast usually from a single beam passing through the objective aperture, to give contrast arising from thickness or atomic number.

DF imaging is employed for grain size, grain morphology and defect examinations including defect type and location identification as the diffraction contrast information is sensitive to crystal lattice distortion caused by strain, defects and bending. Selected area electron diffraction (SAED) patterns are generated by using parallel electron probe according to Bragg's law. If the beam is along specific zone axis, the lattice spacing of crystal planes parallel to the zone axis will be shown in SAED in reciprocal space. For the coatings, cross-section samples are required for TEM observation, and can be employed to confirm the grain growth orientation. If the selected area is large, the averaged textural information is gathered which should be comparable to XRD analyses.

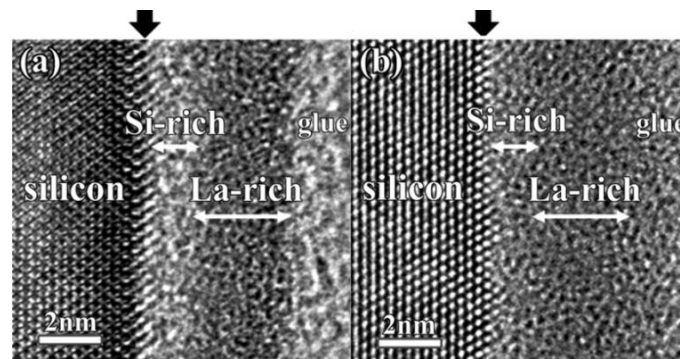


Figure 3.9 High-resolution images of the lanthanum oxide grown on silicon taken by (a) conventional TEM and (b) aberration-corrected TEM. (a) shows contrast artifacts due to electron delocalization effects at interfaces that are removed in (b) [23].*

In high resolution transmission microscopy (HRTEM) many transmitted electron beams are allowed to pass through a large objective aperture that are reconstructed to yield a phase contrast interference pattern that can be directly related to the projected potential of the atomic structure. In thin films, HRTEM is often used to identify secondary phases, defects and grain boundaries.

* Reprinted from [23] S. Inamoto, J. Yamasaki, E. Okunishi, K. Kakushima, H. Iwai and N. Tanaka, *J. Appl. Phys.*, **2010**, 107, 124510. with the permission of AIP Publishing.

However, the imperfection of electron lenses, including spherical and chromatic aberrations, limits the microscope resolution. For very thin interfaces between crystallites or multilayers, aberration corrected TEM is advantageous due to its higher resolution (0.5 – 0.8 Å) compared to conventional TEM (2 Å) (Figure 3.9). To summarise, throughout this thesis grain shape and grain size were examined by DFTEM as commonly several beams were selected by the objective aperture, while HRTEM was used to observe crystallites at atomic scale and XRD was used to determine the average crystal size.

For scanning transmission electron microscopy (STEM) the electron beam is rastered across sample and the transmitted electrons detected by a bright field detector or a high angle annular dark field (HAADF) detector. HAADF imaging delivers Z-contrast images, where the detected electron intensity is approximately proportional to the square of scanned sample atomic number. For multilayer coating observations, HADDF STEM can differentiate layers with higher atomic numbers as these show darker contrast due to the scattering of electrons to larger angles. Together with EDX analysis, the layer compositions can be analysed both qualitatively and quantitatively.

3.3.4 Residual stress calculation

Physical vapor deposition coatings become stressed as a consequence of ion bombardment during deposition. This intrinsic stress, tensile or compressive, will affect coating properties. Tensile stress may cause cracking; while to some extent, compressive stress is desirable for hardening, but when excessive, may promote spalling. Therefore, measuring residual stress is necessary, and in this thesis the deflection method, widely used in engineering applications, was used to assess macrostresses.

In the deflection method a single-side coating is used. For example, if the coating is under compressive stress, the foil will bend convexly from the coated

side. By assuming homogeneous film stress on a stress-less substrate, the mechanical equilibrium can be calculated from Stoney's equation [24, 25]:

$$\sigma_c = \frac{E_s d_s^2}{6(1-\nu_s)rd_c} \quad (3.5)$$

where σ_c (GPa) is the stress, d_c (μm) is the coating thickness, d_s (mm) is the substrate thickness, E_s (GPa) and ν_s (GPa) are substrate Young's modulus and Poisson's ratio respectively. r ($\mu\text{m}^2 / \text{mm}$) is the radius of foil curvature.

$$r \cong \frac{l^2}{8z} \quad (3.6)$$

where l is the foil length (mm) and z is the deflection at foil center (μm). The equation assumes two equilibrium conditions. First, the internal compressive force is regarded as equal to the internal tensile force, and second, the foil bending moment is taken as zero on each axis. For Stoney's equation to be valid the film should be much thinner than the substrate ($d_c \ll d_s \ll r$).

The steel foil substrate was $30 \text{ mm} \times 5 \text{ mm} \times 0.4 \text{ mm}$. Before deposition, the steel foils were annealed to eliminate the intrinsic stress and electrolytically polished to remove heterogeneous matters. After single-sided deposition, the curvature was measured in a mechanical profilometer.

Because Stoney's equation is built on simplified conditions and it does not require complex measurement techniques. The assumptions include: (1) thin film thickness compared to the substrate; (2) small deflections; (3) homogeneous, isotropic substrate and film material; (4) uniform and equiaxial curvature of substrate; and (5) constant stress over the entire substrate. Consequently, the stress variation at different regions on the sample cannot be described and the stress results cannot be trusted if the coating to substrate thickness ratio is > 0.1 . While these assumptions limit its application, this

method is nonetheless widely applied. Meanwhile, many studies to improve the accuracy of Stoney's equation have been reported [26-28].

3.3.5 Nanoindentation test

Nanoindentation was used to gather load-displacement measurements in loading-unloading cycles to extract the elastic modulus and hardness. The indentation hardness H is defined as the mean contact pressure under the completely developed plastic deformation; while the indentation modulus E^* is defined as the load-displacement slope during unloading. Generally, the load on the indenter and the penetration depths are recorded so that for a known indenter geometry the contact area can be determined.

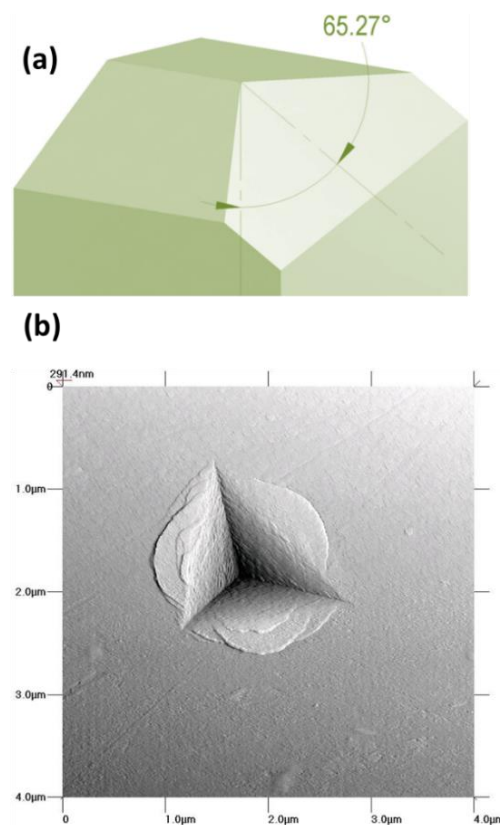


Figure 3.10 A geometry drawing of a Berkovich tip (a) and an indent image by a Berkovich tip from nanoindentation test on a Zr-Cu-Al metallic glass (b) [29].

The Berkovich indenter [30], a three-sided pyramid with a face angle of 65.27° , is a popular tip for small-scale studies (Figure 3.10). Compared to the four-sided pyramid it has sharper point and can be controlled more precisely. During indentation the contact projected area A is calculated as:

$$A=3\sqrt{3}h_c^2 \tan^2 \theta \quad (3.7)$$

where h_c (nm) is penetration depth. For $\theta = 65.27^\circ$, there is:

$$A=24.5h_c^2 \quad (3.8)$$

In an indentation test, the force (mN) and penetration depth (nm) are recorded with the applied load increasing from zero to the maximum, i.e. the loading process, and decreasing from the maximum to zero, i.e. the unloading process. A typical compliance curve is shown in Figure 3.11 [31] and the quantities are explained in Figure 3.12 [32]. After removing the load, the sample tends to recover the original shape elastically, but not fully due to the plastic deformation. Actually, a material with substantial elastic recovery during loading deforms both elastically and plastically. Hence, during measurement the maximum depth, force and contact area between the indenter and sample are not based on true resistance to plastic deformation. The true hardness is required to be differentiated using a sophisticated calculation method that excludes elastic deformation. Moreover, the curves include thousands of data points that must be analysed to calculate H and E^* . To solve these problems, the nonlinear curve fitting method of Oliver and Pharr's [32] is employed to calculate the elastic modulus from unloading curves. Hence, H and E^* can be determined by:

$$H=\frac{P_{\max}}{A} \quad (3.9)$$

$$E^*=\frac{\sqrt{\pi}}{2\sqrt{A}} \frac{dP}{dh} \quad (3.10)$$

where P_{\max} is the maximum load, A is the indenter contact area derived from the penetration depth h_c (Figure 3.11). The Young's modulus E is derived by

$E^* = E/(1 - \nu^2)$, where ν is the Poisson ratio. According to Oliver and Pharr’s method using a Berkovich indenter, P and A have the relationship:

$$P=A(h-h_r)^m \tag{3.11}$$

where A , m and h_r are determined by a least squares fitting procedure.

To measure coating hardness the nanoindentation test avoids removing the coating from the substrate. However, to avoid substrate hardness invalidating the results, penetration depths should not exceed 10% of the entire coating thickness [33].

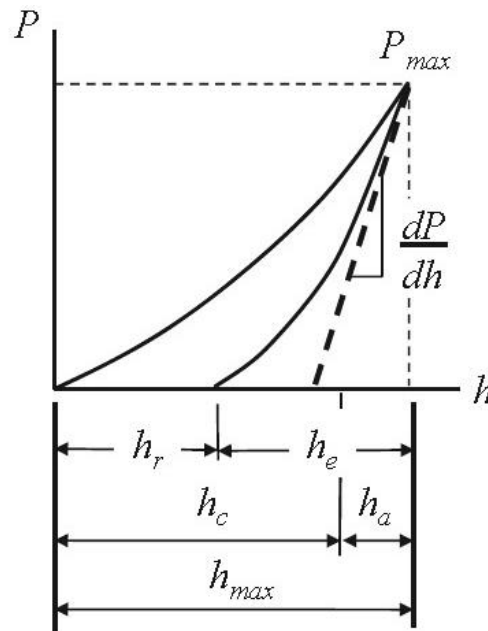


Figure 3.11 A typical example of compliance curves in a nanoindentation experiment. (P_{max} : the maximum load; h_{max} : the maximum penetration depth beneath the sample surface; h_r : the residual impression depth, h_e : the displacement associated with elastic recovery; h_c : the penetration depth of the contact area)*

* Reprinted from Springer Book “Nanoindentation, Nanoindentation testing, 2011, Page No.30, A. C. Fischer-Cripps”, with permission of Springer.

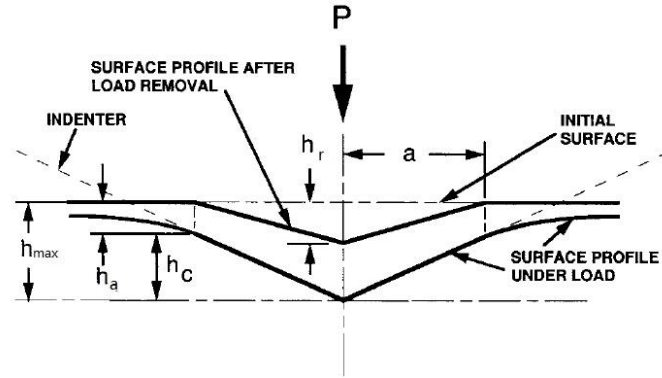


Figure 3.12 A schematic drawing of indentation with parameters used for analysis in Figure 3.11.*

3.3.6 Tensile test

Tensile testing can evaluate ceramic thin film adhesion on ductile metal substrates by determining the interfacial shear strength during cracking. According to the Agrawl-Raj mode [34], when tensile force is applied, the plastically stretched substrate will crack ceramic films normal to the tensile direction. With higher tensile strain the crack density increases until a constant value is reached and the crack is saturated (Figure 3.13). The metal-ceramic interfacial shear strength is estimated from the following equation:

$$\tau = \frac{\pi \delta \sigma}{\lambda} \quad (3.12)$$

where τ (GPa) is the shear strength and σ (GPa) is the coating tensile strength determined by $\sigma = E \varepsilon_f$, (E (GPa) is the coating Young's modulus and ε_f is the strain value when the cracking starts) and δ (μm) is the thickness of the coatings. Finally λ (μm) is the maximum crack spacing when the crack density stabilized. The Agrawl-Raj mode shows the maximum crack spacing is twice the minimum crack spacing. Thus crack distribution can judge whether

* Reprinted from "W.C.Oliver, G.M.Pharr, An improved technique for determining hardness and elastic modulus using load and displacement sensing indentation experiments, Journal of Materials Research, 7, 06, 1573," reproduced with permission.

cracking under tensile strain is following the Agrawl-Raj mode, and if interfacial shear strength can be calculated by equation (3.12).

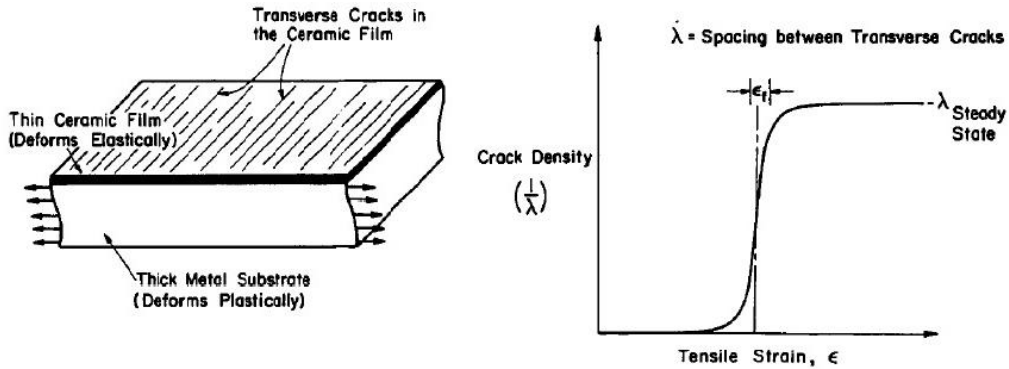


Figure 3.13 Schematic illustration of the tensile test on metal-coating system (left) and the relationship between tensile strain and crack density (right).*

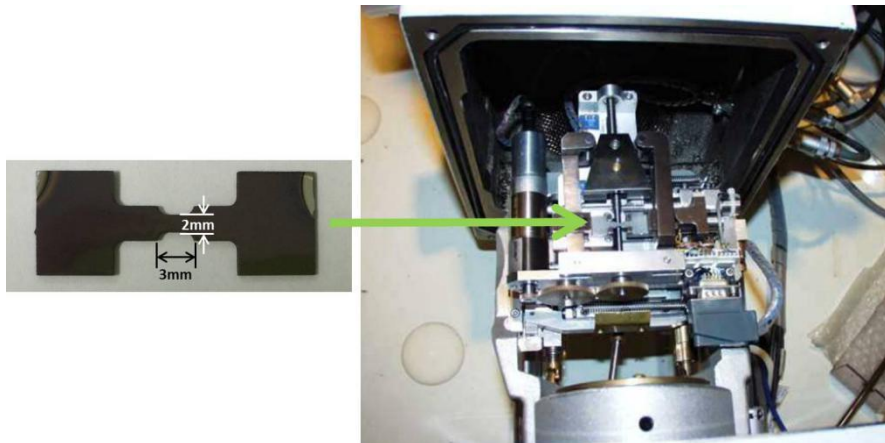


Figure 3.14 The samples for tensile test and the testing device.

In this thesis, *in-situ* tensile testing in a SEM chamber was used to directly observe cracking processes. The ductile substrate was a stainless steel “dog-bone” configuration (Figure 3.14). The samples were placed on the tensile arms in the SEM chamber with the same strain rate used for all tests. However, it was found that the recorded strain was inaccurate because of contributions from the

* Reprinted from Acta Metallurgica, Vol 37, D.C. Agrawal, R. Raj, Measurement of the ultimate shear strength of a metal-ceramic interface, Pages No.1266, Copyright (2016), with permission from Elsevier

sample holder or pulling arms. Therefore, the strain values required correction as follows:

$$\varepsilon = \varepsilon_{\text{exp}} - \left[\sigma \left(\frac{1}{E_{\text{exp}}} - \frac{1}{E} \right) \right] \quad (3.13)$$

where ε is the real strain on sample, ε_{exp} is the experimental strain, σ (MPa) is the stress employed on the system, E_{exp} (MPa) is the experimental Young's modulus, i.e. the slope of σ - ε plot, and E (MPa) is the real metal Young's modulus.

3.3.7 Ball-on-disc tribometer

A tribometer is a device to perform simulated wear to measure the friction coefficient and wear volume. A ball-on-disc tribometer consists of a stationary ball under a constant load and a rotating disc which is in contact with the ball (Figure 3.15). During the tribology test, friction occurs continuously between the ball and sample surface with a wear track of a certain diameter. The friction force F is recorded and the coefficient μ directly calculated as the ratio of the friction force F (unit: N) to the loading force N (unit: N) according to the general equation:

$$F = \mu N \quad (3.14)$$

The final result is a plot of the friction coefficient versus the sliding distance (m). The coating wear volume (mm^3) is determined by examining the surface using a profilometer after the test. The wear rate of each coating is calculated as:

$$V = kNs \quad (3.15)$$

where V (mm^3) is the wear volume, N (N) is the load and s (m) is the sliding distance. k is the specific wear rate coefficient and its unit is mm^3/Nm . Higher wear rates mean material was removed more rapidly, indicating poorer wear resistance in the case of protective coatings. The results should be treated critically however, as the operation environment will influence wear rate and

the comparison of coating wear performance should be made under identical experimental parameters. Therefore, this test is a simple simulation of wear and is appropriate for comparative examination of similar materials. Such circumspection is needed because during testing high local pressure during two-body contact may change due to plastic deformation, which is influential on wear mechanism and change the friction mode [35].

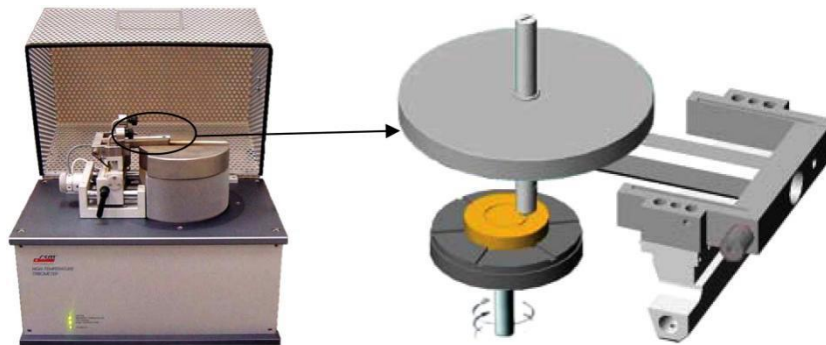


Figure 3.15 A ball-on-disc tribometer (a) and a tribology testing illustration.*

3.4 Overview of the methodologies

In conclusion, coatings were fabricated by PVD techniques, including Ti-Al-N multilayer coatings deposited by CAD, and Ti-Si-N nanocomposite coatings deposited by a hybrid of HiPIMS and DC-pulse magnetron sputtering. The principle processing parameters are different for each of the multi-phase nanocomposite structures. Extensive characterisation by XRD, SEM and TEM are required to optimize the characteristics of the surface, topography and nanostructure including crystal size, grain size, grain boundaries and interfaces. The structure variation determined by the combination of processing parameters will affect coating performances, including hardness, wear and oxidation

* Reprinted from Tribology International, Vol 56, Liliang Wang , Jie Zhou, Jurek Duszczuk, Laurens Katgerman, Friction in aluminium extrusion—Part 1: A review of friction testing techniques for aluminium extrusion, Pages No.94, Copyright (2016), with permission from Elsevier

resistance. Hardness and Young's modulus are calculated from loading-unloading curves by nanoindentation testing, while the coating adhesion is evaluated through crack density by *in-situ* tensile testing. Oxidation resistance of various coatings are evaluated by comparing weight gain and phase transitions after high temperature annealing in air. The tribology test and heat treatment is a simple simulation of the machining environment, that are used to examine the coating performance at high friction and high temperatures. Based on the systematic characterization of coatings, correlations among the processing, structure and properties of hard coatings can be established.

References:

- [1] G. A. Lyubimov and V. I. Rakhovskii, *Soviet Physics Uspekhi*, **1978**, 21, 693.
- [2] V. I. Rakhovskii, *IEEE Transactions on Plasma Science*, **1976**, 4, 81-102.
- [3] P. Swift, D. McKenzie, I. Falconer and P. Martin, *J. Appl. Phys.*, **1989**, 66, 505-512.
- [4] D. M. Sanders and A. Anders, *Surf. Coat. Technol.*, **2000**, 133, 78-90.
- [5] H. Randhawa and P. Johnson, *Surf. Coat. Technol.*, **1987**, 31, 303-318.
- [6] I. G. Brown, *Annu. Rev. Mater. Sci.*, **1998**, 28, 243-269.
- [7] P. J. Martin and A. Bendavid, *Thin Solid Films*, **2001**, 394, 1-14.
- [8] R. Boxman and S. Goldsmith, *Surf. Coat. Technol.*, **1992**, 52, 39-50.
- [9] B. Warcholinski, A. Gilewicz, J. Ratajski, Z. Kuklinski and J. Rochowicz, *Vacuum*, **2012**, 86, 1235-1239.
- [10] H. Randhawa, *Thin Solid Films*, **1988**, 167, 175-186.
- [11] A. Anders, *Surf. Coat. Technol.*, **1999**, 120-121, 319-330.
- [12] H. Takikawa and H. Tanoue, *Plasma Science, IEEE Transactions on*, **2007**, 35, 992-999.
- [13] V. Kouznetsov, K. Macák, J. M. Schneider, U. Helmersson and I. Petrov, *Surf. Coat. Technol.*, **1999**, 122, 290-293.

- [14] J. T. Gudmundsson, J. Alami and U. Helmersson, *Surf. Coat. Technol.*, **2002**, 161, 249-256.
- [15] S. Konstantinidis, J. P. Dauchot, M. Ganciu, A. Ricard and M. Hecq, *J. Appl. Phys.*, **2006**, 99, 013307.
- [16] J. Alami, K. Sarakinos, G. Mark and M. Wuttig, *Appl. Phys. Lett.*, **2006**, 89, 154104.
- [17] M. Ganciu, S. Konstantinidis, Y. Paint, J. P. Dauchot, M. Hecq, L. De Poucques, P. Vasina, M. Mesko, J.-C. Imbert and J. Bretagne, *Journal of Optoelectronics and Advanced Materials*, **2005**, 7, 2481-2484.
- [18] P. Scardi, L. Lutterotti and P. Maistrelli, *Powder Diffr.*, **1994**, 9, 180-186.
- [19] G. Harris, *The London, Edinburgh, and Dublin Philosophical Magazine and Journal of Science*, **1952**, 43, 113-123.
- [20] D. Rickerby, A. Jones and B. Bellamy, *Surf. Coat. Technol.*, **1989**, 37, 111-137.
- [21] J. I. Goldstein, D. E. Newbury, P. Echlin, D. C. Joy, C. Fiori and E. Lifshin, in *Scanning Electron Microscopy and X-Ray Microanalysis: A Text for Biologist, Materials Scientist, and Geologists*, Springer US, Boston, MA, 1981, DOI: 10.1007/978-1-4613-3273-2_3, pp. 53-122.
- [22] D. B. Williams and C. B. Carter, in *Transmission Electron Microscopy: A Textbook for Materials Science*, Springer US, Boston, MA, 2009, DOI: 10.1007/978-0-387-76501-3_9, pp. 141-171.
- [23] S. Inamoto, J. Yamasaki, E. Okunishi, K. Kakushima, H. Iwai and N. Tanaka, *J. Appl. Phys.*, **2010**, 107, 124510.
- [24] R. Hoffman, *Physics of thin films*, **1966**, 3, 211-273.
- [25] G. G. Stoney, *Proceedings of the Royal Society of London. Series A, Containing Papers of a Mathematical and Physical Character*, **1909**, 82, 172-175.
- [26] G. Janssen, M. Abdalla, F. Van Keulen, B. Pujada and B. Van Venrooy, *Thin Solid Films*, **2009**, 517, 1858-1867.

- [27] C. A. Klein, *J. Appl. Phys.*, **2000**, 88, 5487-5489.
- [28] F. Von Preissig, *J. Appl. Phys.*, **1989**, 66, 4262-4268.
- [29] J. B. Puthoff, D. S. Stone, H. Cao and P. M. Voyles, 2008.
- [30] E. Berkovich, *Ind. Diamond Rev*, **1951**, 11, 129-133.
- [31] A. C. Fischer-Cripps, in *Nanoindentation*, Springer New York, New York, NY, 2011, DOI: 10.1007/978-1-4419-9872-9_2, pp. 21-37.
- [32] W. C. Oliver and G. M. Pharr, *J. Mater. Res.*, **1992**, 7, 1564-1583.
- [33] F. Cleymand, O. Ferry, R. Kouitat, A. Billard and J. Von Stebut, *Surf. Coat. Technol.*, **2005**, 200, 890-893.
- [34] D. C. Agrawal and R. Raj, *Acta Metall.*, **1989**, 37, 1265-1270.
- [35] L. Wang, B. Yu, P. M. Asbeck, Y. Taur and M. Rodwell, *Int J High Speed Electron Syst*, **2011**, 19, 15-22.

Chapter 4

Processing, structure and properties of TiN/Ti_xAl_{1-x}N nano-sized multilayer coatings*

TiN/Ti_xAl_{1-x}N coatings were deposited by cathodic arc deposition with superlattice periods ranging from 8 to 45 nm controlled by the substrate holder rotation speed. The microstructures were studied by X-ray diffraction, scanning electron microscopy and transmission electron microscopy and correlated to the mechanical properties and wear resistance. Nanolayered coatings consist of columnar grains with preferred orientation <111>, which are connected by low-angle grain boundaries. Variation of superlattice period plays a significant role in controlling coating properties. A superlattice structure appears as the period decreases from 45 nm to 13 nm and delivers the highest hardness 39 ± 4 GPa and Young's modulus 503 ± 40 GPa. Further reduction of period to 8 nm reduces both hardness and Young's modulus. However, wear resistance continues to improve along with the smaller period as a higher concentration of interfaces blocks crack extension.

* This Chapter is substantially submitted for publication as J Wang et al., Microstructure influences on mechanical properties and tribology behaviours of TiN/Ti_xAl_{1-x}N multilayer coatings, SURFCOAT-D-16-02119.

4.1 Introduction

TiN fabricated by physical vapour deposition (PVD) has been widely employed as a protective coating for high speed machining due to its superb hardness and wear resistance [1-3]. However, TiN begins to oxidize at 500 °C and can be fully oxidized to titania at 800°C, leading to a deterioration in performance in extreme cutting environments at elevated temperature [4]. To fulfil the higher demands of precision cutting, (Ti, Al)N is a promising replacement of TiN as it has improved oxidation resistance, and superior hardness and tribological performance [5]. At high temperatures, Al oxidizes to form a protective alumina layer that attenuates oxygen inward diffusion and cation outward diffusion, which delays the degradation of mechanical properties [6, 7]. In this thesis, TiN and (Ti, Al)N was hybridized as multilayer nano-scale structures as it was reported nanolayered coatings consisting of two components, could achieve hardness greater than the rule-of-mixture value [8, 9]. Several theories were proposed to explain the hardening effect including the image force effect by different shear moduli [10], the coherency strain effect induced by misfit lattice parameters [11] and the supermodulus effect [12]. Meanwhile, these hardening mechanisms are influenced significantly by superlattice period (Λ) which determines the relative layer and interface volumes [13]. Nevertheless, systematic microstructural characterization of TiN/Ti_xAl_{1-x}N nanolayers is lacking, as is the optimization of mechanical and tribological performance as a function of Λ .

This chapter describes the fabrication of TiN/Ti_xAl_{1-x}N coatings by cathodic arc deposition (CAD) [14] with Λ controlled by substrate holder rotation speed and tests that the decreased Λ and increased interface concentration enhance coating properties to a saturated value. In order to reveal the relationship between structure and performance, coatings of different Λ were examined by electron microscopy and powder X-ray diffraction (XRD); while hardness and wear

resistance were measured by nanoindentation and ball-on-disc tests respectively. In this manner, it was demonstrated that optimized mechanical and tribological properties of TiN/Ti_xAl_{1-x}N coatings can be achieved by controlling substrate holder speed.

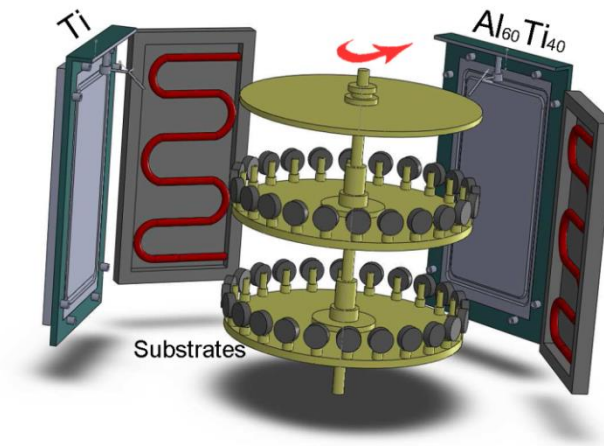


Figure 4.1 Schematic drawing of PVD arc deposition chamber

4.2 Experimental method

4.2.1 Coating deposition

For this multilayer system a planar deposition device (PLATIT) was used with 2 arc powered targets, pure titanium (99.99%) and Al_{0.6}Ti_{0.4}. After polishing and degreasing, AISI M2 HSS substrates were mounted on rotating substrate holders (Figure 4.1). During fabrication the chamber was first evacuated and heated to ~ 400° C, and a high bias voltage was applied to the substrate holders to etch substrates. Argon plasma etching (bias ≈ -800 V) for 2 min at 0.3 Pa and Ti etching (I_{Ti} = 100 A, bias ≈ -700 V) for 10 min at 1 Pa were performed sequentially. For coating, the deposition bias was decreased to -100 V while a 110 sccm flow of nitrogen was injected into the chamber where the pressure was kept at ~ 2 Pa. Both targets were powered on the whole time and the arc current set to 100 A. First, a buffer layer consisting of Ti and TiN was

deposited for 25 min and then the TiN/Ti_xAl_{1-x}N multilayer deposition time was 50 min. Overall, the coating thickness was 4.1 μm, including 0.6 μm Ti and 0.4 μm TiN buffer layers. The rotation speed was adjusted from 1 to 7 revolutions per minute (r.p.m) in order to obtain multilayers of different Λ while the whole coating thickness remained unchanged.

4.2.2 Coating characterization

Scanning electron microscopy (SEM), X-ray diffraction (XRD) and transmission electron microscopy (TEM) were the main techniques for characterizing crystalline phases and microstructures. Field emission SEM (FESEM) (JEOL 7800F) operated in secondary electron imaging (SEI) mode was used to observe coating surfaces and cross-section fracture morphology. XRD patterns were gathered in the θ -2 θ scan mode with a Brucker D8 instrument using CoK α 1 radiation ($\lambda=1.788970\text{\AA}$) in Bragg-Brentano geometry. Microstructural details were revealed by TEM and scanning transmission electron microscopy (STEM) (JEOL JEM-2100F) at a 200 kV accelerating voltage and with a C_s-corrected high resolution TEM (FEI Titan) operated at 300 kV. TEM samples were prepared to a thickness of ~100 nm by depositing coatings on copper foils that were glued face-to-face and cut in cross section. These cross sections were mechanically polished to ~30 μm then argon ion milled to electron transparency (Precision Ion Polishing System, Gatan). The chemical composition of the layers was analyzed by energy dispersive X-ray spectroscopy (EDX) in STEM mode.

Coating mechanical properties were quantified by nanoindentation testing (NHT CSM Instrument). Hardness (H) and the effective Young's modulus (E*) were calculated using the Oliver and Pharr method [15] after each indentation during which a Berkovich diamond tip was imposed on the coating surface. The penetration depths were kept less than 250 nm, which is < 10% of the

multilayer thickness to avoid substrate and buffer layers affecting the test results [16]. Meanwhile ball-on-disc tests (CSM tribometer) in air at room temperature (20 – 30 °C) were employed to compare the wear resistance of coatings with different Λ . The relative humidity of the test environment was 50% - 55%. The M2 steel cylinders with multilayer coatings were fixed on a flat stage. Samples were rotated with a 9 mm radius wear track resulting during the tests. A 10 N constant load was applied on the WC/Co counter ball and the sliding velocity was 100 mm/s. The sliding distance was 565 m in 10,000 laps. After tribology testing a white-light profilometer (ALTISURF500) with 10 nm height resolution was used to examine wear scars. The scar was scanned at a speed of 15 $\mu\text{m/s}$ in 2D mode.

4.3 Coating overview processed by arc deposition

4.3.1 Controlled bilayer period Λ

Coatings of various Λ were deposited by controlling the substrate holder rotation speed. The multilayers appear in alternate contrast deposited above the TiN and Ti buffer layers on the substrate (Figure 4.2(a)). The Λ consisted of bright Ti_xAl_{1-x}N and dark TiN layers (Figure 4.2(b) and (c)) and the values of Λ were measured directly by TEM and confirmed by the XRD satellite peak spacing. Λ varies inversely with rotation speed (Figure 4.2(d)), consistent with Ducros et al. [17]. Besides the substrate rotation speed, the component material deposition rate and substrate rotation configuration (one-fold or two-fold rotation) also affect the elementary layer thickness. Higher rotation speed or two-fold instead of one-fold rotation mode (a three-fold rotation example in Figure 3.1) decreases the time that substrates face each target resulting in thinner layers. In this work, the substrate rotation speed was the only parameter changed in different deposition batches and thus discrete Λ values were obtained. Moreover, according to the different objects, Λ can be tailored by

appropriate coordination of substrate rotation speed, multilayer composition and the arc current applied on each target.

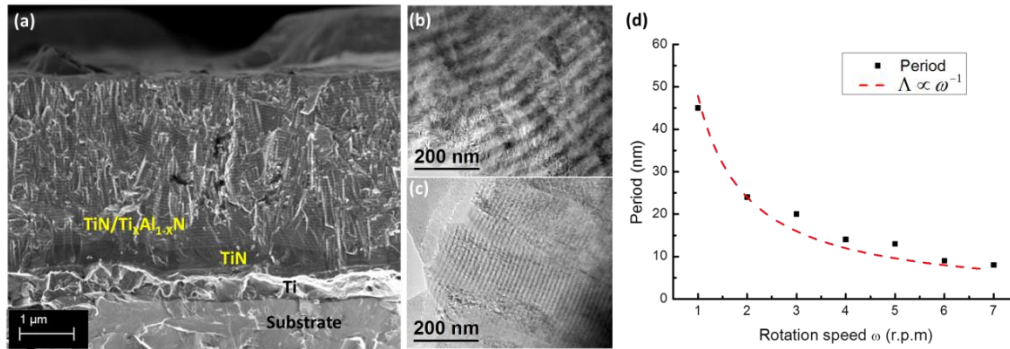


Figure 4.2 SEM fracture of the coating on substrate when rotation speed = 1 r.p.m, which consists of Ti, TiN layers and TiN/Ti_xAl_{1-x}N multilayers(a); TEM bright field image of 1 r.p.m (b) and 4 r.p.m (c) coating cross sections; And Λ vs rotation speed plot (d).

4.3.2 Coating morphology

Figure 4.3 (a) shows a typical coating surface with rough morphology over which 0.1 μm to 10 μm diameter droplets are distributed. This is a common phenomenon in arc deposition, arising either from the intense interaction between the high-energy arc and the cathodic target directly at the emission spot, or the injection of high pressure plasma imposed on the target material [18-20]. The architecture of a typical droplet 1 μm in diameter comprises a core of Ti and an outer shell of alternating Ti and Al, supposed to be TiN/Ti_xAl_{1-x}N (Figure 4.3 (b)). It is probable that the original droplet (0.7 μm in diameter) was injected from the target and reached the substrate. Multilayers were then deposited over it and an enlarged sphere generated. This sphere is separated from the flat coating surface by voids (indicated by arrow in Figure 4.3 (b)) which are caused by a “shadowing effect” where the protruding droplet blocked the evaporated material depositing in the interspace between the sphere and coating surface. The void around the droplets could initiate cracks under load,

leading to mechanical failure. Therefore the presence of droplets may harm coating performances.

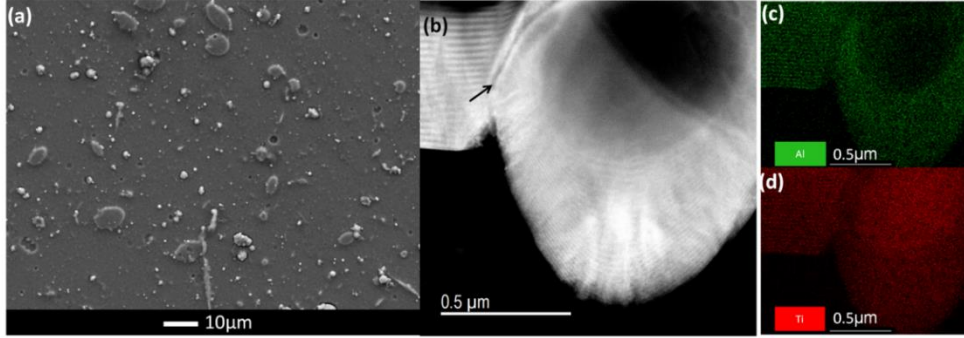


Figure 4.3 The 2 r.p.m TiN/Ti_xAl_{1-x}N coating rough surface with a number of droplets (a); A high angle annular dark field (HAADF) image of one droplet construction in STEM mode (b) and its EDX element mappings ((c) and (d)), (c) showing the Al and (d) the Ti distributions.

4.4 Coating structures and compositions

4.4.1 XRD analysis

The multilayer coatings consisted of a rock-salt face centered cubic (fcc) structure (Figure 4.4) and were highly <111> textured (Figure 4.4(c)). However, the position of the (111) reflection was dependent on Λ . At 1 r.p.m ($\Lambda = 45$ nm) two discrete (111) reflections belonging to TiN and Ti_xAl_{1-x}N were present, but at faster substrate rotation these merge to one pronounced peak surrounded by a pair of equally spaced satellites. Satellites arise from a superlattice with a lattice parameter intermediate to TiN and Ti_xAl_{1-x}N. In this work, satellites appear when the rotation speed > 4 r.p.m ($\Lambda \leq 14$ nm). The primary reflection and satellite peak spacings can be related to Λ as [21]:

$$\sin \theta_{\pm} = \sin \theta_B \pm m_{th} \lambda / (2\Lambda) \quad (4.1)$$

where θ_{\pm} is the position of m_{th} positive or negative satellite peaks, θ_B is the primary Bragg reflection, λ is X-ray wavelength, and Λ is the superlattice

period. To calculate Λ , XRD patterns from 40° to 46° were recorded with a lower scan speed of $0.004^\circ \text{ s}^{-1}$ (Figure 4.4 (b)). The two (111) reflections of the 1 r.p.m coating after fitting yield the lattice parameter of TiN: $a = 4.27(0) \text{ \AA}$; and Ti_xAl_{1-x}N: $a = 4.19(0) \text{ \AA}$ while Λ of coatings deposited at higher rotation speed were calculated using formula 4.1. The calculated Λ are consistent with the direct measurements by TEM.

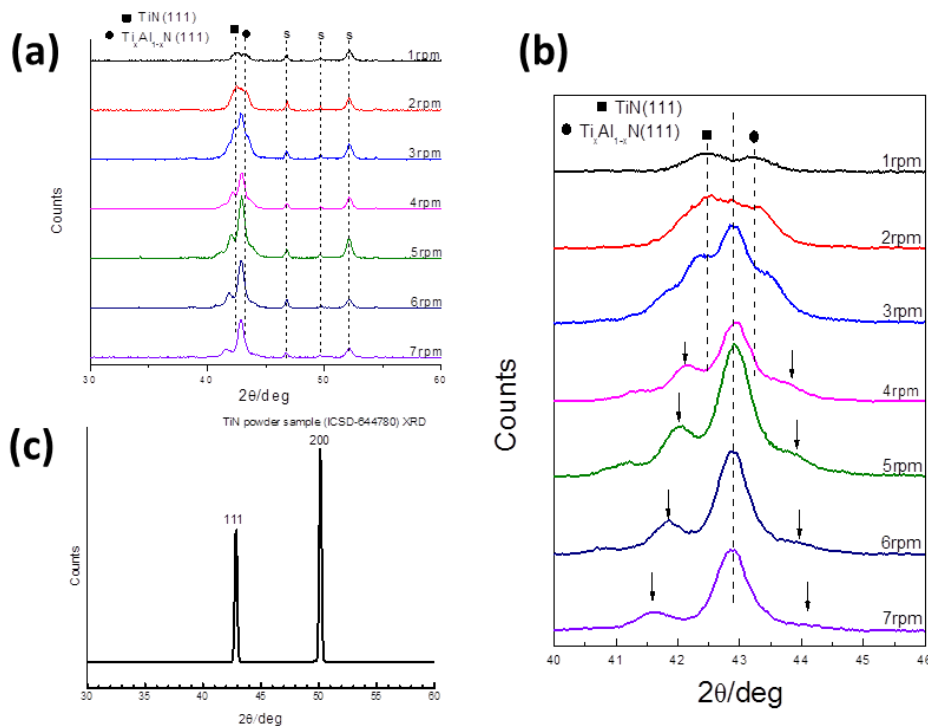


Figure 4.4 XRD patterns from $2\theta = 30^\circ$ to $2\theta = 60^\circ$ of TiN/Ti_xAl_{1-x}N coatings deposited at 1 to 7 r.p.m.(a); Zoomed in XRD patterns from $2\theta = 40^\circ$ to $2\theta = 46^\circ$ and satellites indicated by arrows for lattice parameter and Λ calculation (b); (c) is the calculated TiN powder XRD pattern for comparison with highly textured coatings in (a).

4.4.2 TEM structural analysis

Coatings deposited at different substrate rotation speeds were examined by TEM. Using the same field limiting aperture the selected area electron diffraction (SAED) patterns were obtained for 1 r.p.m ($\Lambda = 45 \text{ nm}$), 4 r.p.m (Λ

= 14 nm) and 7 r.p.m ($\Lambda = 8$ nm) coatings (Figure 4.5). The 1 r.p.m ($\Lambda = 45$ nm) coating presents (111) and (200) reflections along the grain growth direction suggesting crystals preferably develop along $\langle 111 \rangle$ and $\langle 200 \rangle$; while $\langle 111 \rangle$ texture was dominant for coatings deposited faster than 1 r.p.m.

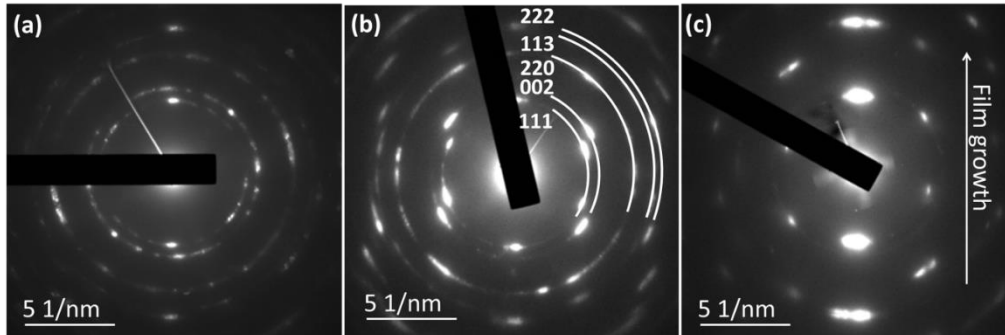


Figure 4.5 SAED of TiN/Ti_xAl_{1-x}N coatings deposited at: (a) 1 r.p.m. ($\Lambda=45$ nm), (b) 4 r.p.m. ($\Lambda=14$ nm) and (c) 7 r.p.m. ($\Lambda=8$ nm) showing the coatings deposited faster than 1 r.p.m. are textured at $\langle 111 \rangle$.

In detail, the SAED of the 1.r.p.m coating shows two sets of patterns arrowed in Figure 4.6 (a), consistent with XRD result that found isostructural TiN and Ti_xAl_{1-x}N. Shifting to the image mode, columnar grains 50 - 100 nm in diameter grew perpendicularly to the coating surface and layers continuously crossed these grains. Comparing the bright field (BF) (Figure 4.6 (c)) and dark field (DF) (Figure 4.6(d)) images reveals the columns originate in the TiN buffer layers and expand in multilayers with preferred orientation following a competitive grain growth mechanism [22] that favors multilayer coating adhesion to the substrates. The STEM and EDX mapping of the multilayers (Figure 4.6 (e) and (f)) show sharp compositional interfaces both among alternating layers and between the multilayer and buffer layer part, indicating limited elemental diffusion. The grains were connected by low-angle grain boundaries with a mis-orientation smaller than 15° , which is probably caused by the initial substrate roughness that also results in the layer curvature [23]. For clarification, the high resolution TEM (HRTEM) image of the 4 r.p.m

coating shows that grains consisting of multilayers were connected by coherent grain boundaries without amorphous content or void space (Figure 4.7).

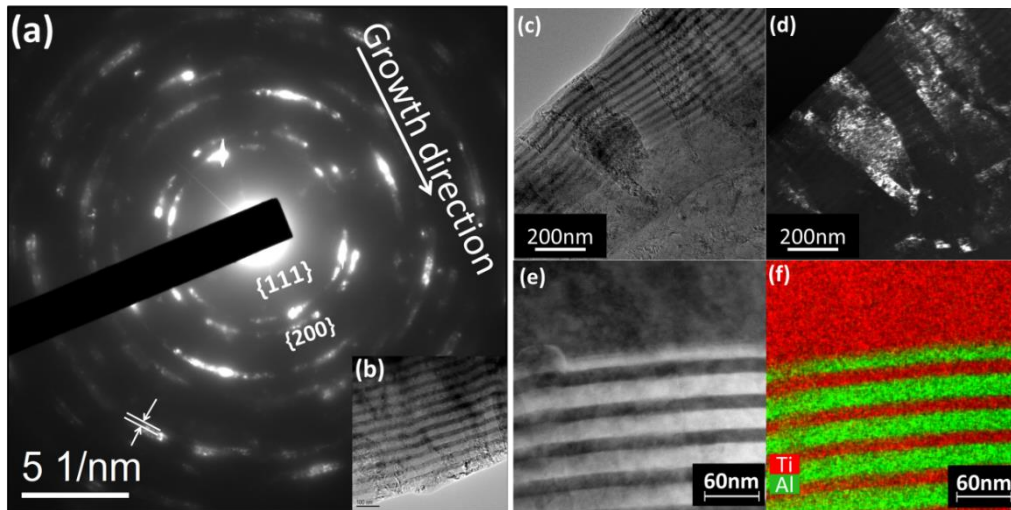


Figure 4.6 Multilayer overview of the coating deposited at 1 r.p.m (b) and corresponding SAED pattern (a) which indicates two discrete reflection sets belong to TiN and Ti_xAl_{1-x}N; BFTEM (c) and DFTEM (d) of coatings consisting of columnar grains originated in buffer layer; And corresponding bright field STEM (e) and EDX mapping (f) showing the sharp interfaces.

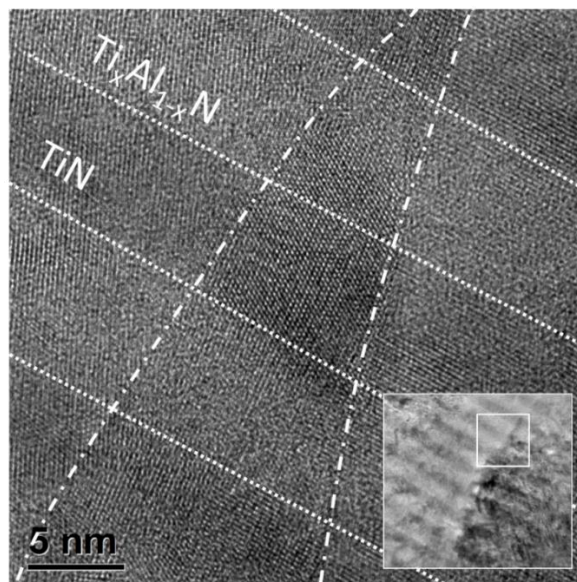


Figure 4.7 HRTEM images of one grain located between two bigger grains in TiN/Ti_xAl_{1-x}N coating deposited at 4 r.p.m by zooming in squared area in the inset.

TiN and Ti_xAl_{1-x}N layers were epitaxially stacked with accompanying mismatch dislocations caused by the lattice parameter variation from TiN ($a = 4.27(0) \text{ \AA}$) to Ti_xAl_{1-x}N ($a = 4.19(0) \text{ \AA}$). For example, mismatch dislocations were demonstrated in the 2 r.p.m coating by fast Fourier transformation (FFT) of the HRTEM image (Figure 4.8). The diffraction pattern, inset in Figure 4.8 (a), corresponds to the squared area at the interface of TiN and Ti_xAl_{1-x}N, proving the grain grew along [111] and the image was aligned to the [110] zone axis. By applying a mask on the 1 and 1' reflections representing the grain preferred orientation [111] and calculating the inverse FFT, (111) planes were extracted with no sign of mismatch dislocation (Figure 4.8 (b)). Counterwise, performing FFT inversion on the (200) reflections (2 and 2') revealed several mismatch dislocations. This suggests that the epitaxy along [111] between TiN and Ti_xAl_{1-x}N penetrates the interface with lattice mismatch dislocations present.

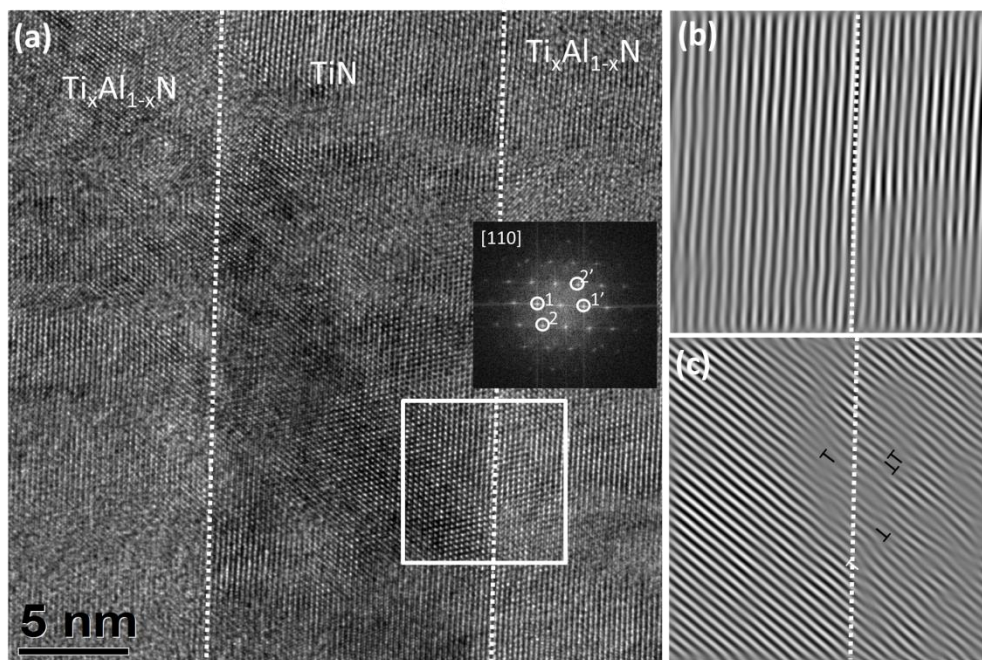


Figure 4.8 2 r.p.m TiN/Ti_xAl_{1-x}N coating. (a) HRTEM image and corresponding FFT showing an obvious epitaxy along [111]; (b) Inverse FFT images of 1 and 1' dots, (c) 2 and 2' present misfit dislocations arisen from the lattice parameter difference.

Moreover, the lattice parameter mismatch could induce sub-grains in a singular grain as reported by other researchers [24] and supported in this work by the misorientation of FFT diffraction patterns in the 4 r.p.m coating (Figure 4.9).

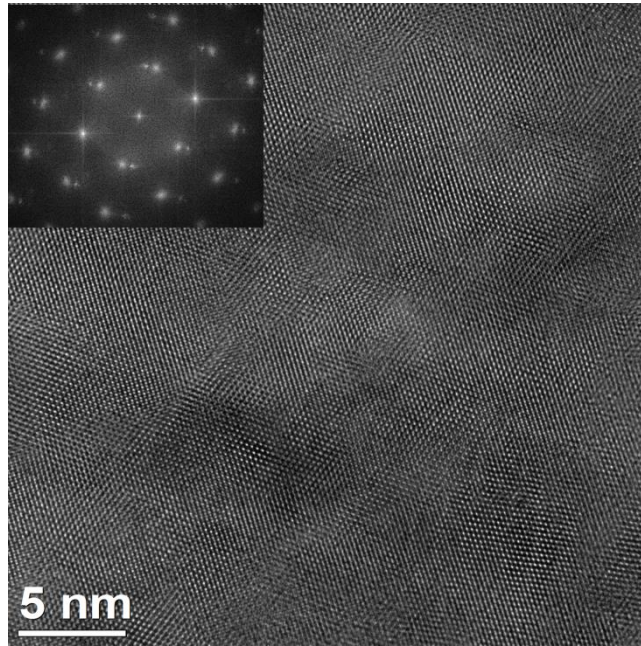


Figure 4.9 A grain of 4 r.p.m coating and its FFT diffraction patterns.

4.4.3 Chemical analysis

STEM images with EDX mapping of the 1 r.p.m coating present the compositional alternation between TiN and Ti_xAl_{1-x}N with sharp interfaces (Figure 4.10 (a)). In general, Ti_xAl_{1-x}N layers are wider than TiN layers with the thickness ratio Ti_xAl_{1-x}N : TiN \approx 4 : 3 arising because the melting point of Ti_{0.4}Al_{0.6} alloy is lower than Ti leading to a higher deposition rate [25]. The EDX line profiles of the 1 r.p.m coating present a trapezoidal modulation [26], namely, the interface width is less than the component layer thickness; while the interface width of the 4 r.p.m coating contributes a larger proportion of the entire Λ thickness (Figure 4.10 (b) and (c)). Here the interface width is defined as the distance from the position of maximum to minimum Al content. Furthermore, in the 1 r.p.m coating Al-rich layers consist of 57 at% Al and 43

at% Ti, in agreement with target alloy composition Al_{0.6}Ti_{0.4} while in the 4 r.p.m coating the Al-rich layer contains ~ 52 at% Al and ~ 48 at% Ti indicating a less sharp compositional contrast. It is concluded that as Λ decreased the interface width to Λ ratio increased and the chemical contrast from Ti-rich layers to Al-rich layers decreased. The less distinct compositional difference may affect coating mechanical properties.

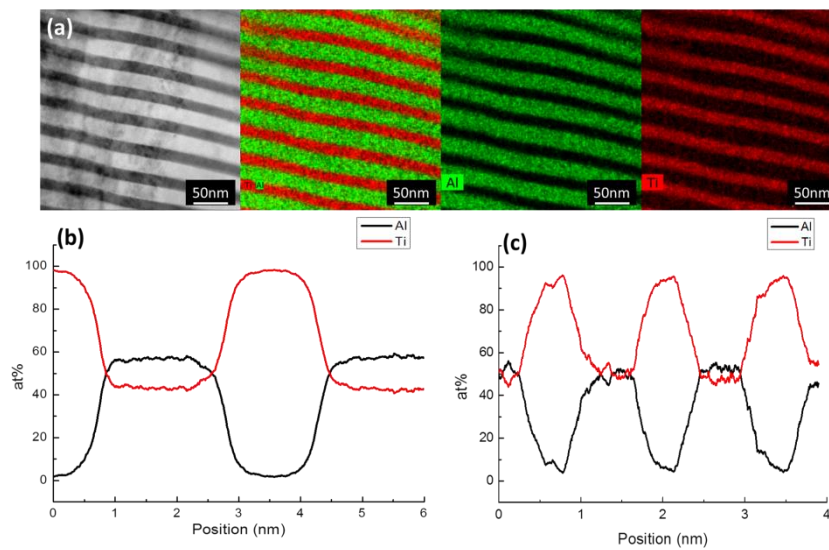


Figure 4.10 (a) STEM BF image of the 1 r.p.m TiN/Ti_xAl_{1-x}N coating and corresponding EDX element maps showing sharp interfaces; Line scan profiles perpendicular to coating surfaces of 1 r.p.m (b) with trapezoidal compositional modulation and 4 r.p.m (c) with sawtooth modulation.

4.5 Coating properties

4.5.1 Hardness and Young's modulus

The hardness and Young's modulus derived from nanoindentation tests are plotted as a function of Λ (Figure 4.11). With Λ decreasing from 45 nm to 13 nm hardness it is found that Young's modulus increases and reaches a maximum $H = 39 \pm 4$ GPa and $E = 503 \pm 40$ GPa. However, as Λ decreased further from 13 nm to 8 nm, H and E both deteriorated. The hardness of the

TiN/Ti_xAl_{1-x}N multilayer with $\Lambda = 13$ nm was enhanced compared to the bulk TiN ($H = 28.3 \pm 2.9$ GPa) and Ti_{0.4}Al_{0.6}N ($H = 32.58 \pm 2.42$ GPa) coatings deposited at the same conditions by CAD.

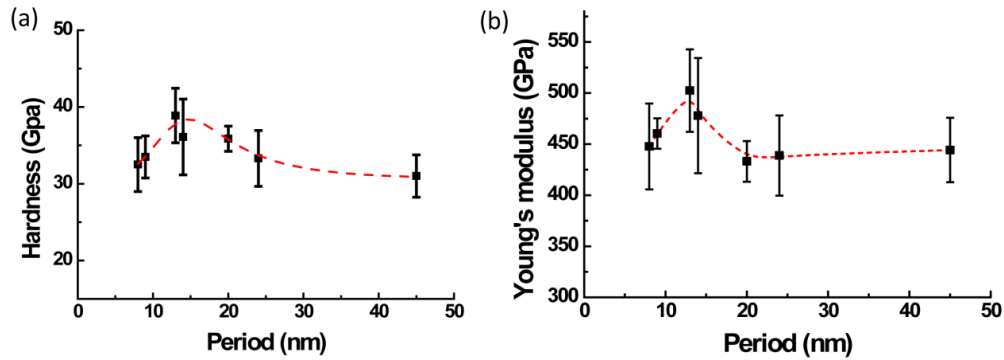


Figure 4.11 Plots of H (a) and E (b) versus Λ of coatings and the corresponding fitted peak curves in red dashed lines.

The hardness enhancement beyond the mix-rule-value is attributed to the superlattice structure. One theory claims the lattice parameter mismatch between two phases results in coherency strain fields which obstruct dislocation movement [11, 27]. However, the TiN/(Ti, Al)N system has a lattice mismatch of only 2% according to XRD and would not be primarily affected by the coherency strain [28]. Another theory considers that an image force exists between multilayers of different shear modulus that confines dislocations in the low shear modulus region and inhibits movement to the high modulus region [8, 29]. This means that interfaces act as barriers when dislocations pass across multilayer interfaces, resulting in a higher macroscopic hardness. According to the model of Chu and Barnett [30], the image force effect restraining dislocations across layers is more efficient as Λ increases. However, with larger Λ , dislocations move within single layers more easily, possibly leading to mechanical failure. Therefore, Λ plays a role on hardness enhancement of multilayered coatings, and generally, as Λ becomes smaller the hardness increases first then decreases. In this work, the hardness and Young's modulus

varied as a function of Λ . Stress enabled dislocation movement within layers was lower than across layers when Λ was 45 nm. On one hand, as Λ decreased the chance to form dislocations within layers was reduced and there was less dislocation gliding. Moreover, the increased frequency of interfaces created more obstacles for dislocation movement. This hardening mechanism as Λ decreased can be described by the following relationship: $(H - H_0) \propto \Lambda^{-p}$, where H_0 is the hardness of the bulk material of same composition as the multilayered coating, and p relates to the component layer thickness to period ratio and shear modulus. However, with decreasing Λ a maximum value is achieved, beyond which the hardness decreases because a weakened image force field resulted from interface multiplication that makes dislocation gliding across layers easier. In addition, the diffuse composition modulation can lower the two-phase shear modulus difference and impair the image force effect. In this work, the composition difference decreased with Λ (Figure 4.10), implying a less effective image force and a higher mobility of dislocation across interfaces. Overall the combined effects of blocking dislocation movement in layers at low Λ , and across layers at high Λ , contributed to a peak in hardness and Young's modulus of the coating with $\Lambda = 13\text{nm}$.

4.5.2 Tribology

Figure 4.12 shows the friction coefficient (μ) in ball-on-disk tests versus sliding distance. The counter balls did not wear through coatings to reach the substrate. Abrasive wear occurred at a rate determined by ball material and coating hardness [31]. The stabilized μ was $\sim 0.8-0.9$ for 1, 4 and 7 r.p.m coatings and did not vary among coatings with different Λ (Figure 4.12 (a)). The profilometer examined the wear scar, with profiles revealing a shallower depth on the sample deposited at higher substrate rotation speed, suggesting smaller Λ resulted in decreased wear rate and improved wear resistance (Figure 4.12 (b)).

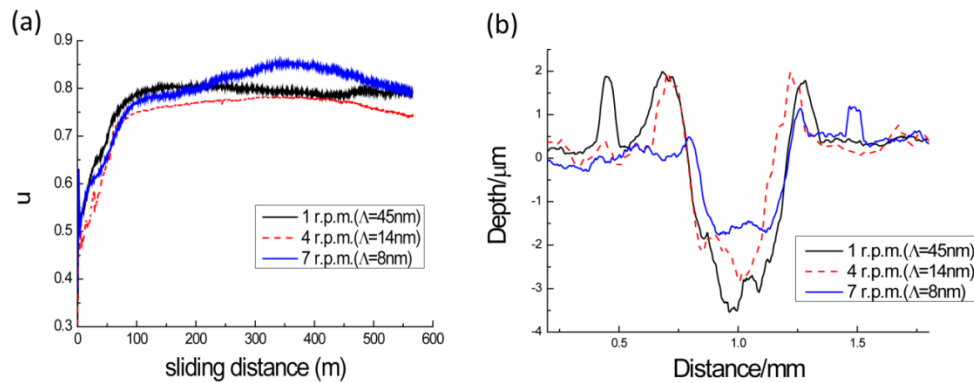


Figure 4.12 1 r.p.m., 4 r.p.m. and 7 r.p.m coatings μ vs sliding distance (a) and the wear scar profiles (b).

The tendency towards improved wear resistance at lower period is discordant with the hardness variation, indicating that coatings with superior hardness do not necessarily possess high wear resistance. It was reported that the elastic modulus and the H/E ratio was a reasonable indicator of tribology performance [32, 33]. In this work, H/E for all periods were similar, suggesting that mechanical properties were not the principle cause for the different wear resistance. A more reasonable explanation is that the increased interface population of shorter period multilayers suppressed crack propagation. The alternating stress field model of nano-scaled multilayers proposed by Mendibide et al. [34] treated the interfaces as obstacles that scatter crack energy and induce crack extension transversally instead of longitudinally. Furthermore, tribo-oxidation might occur during sliding which would compromise the coating properties. However, coatings with smaller Λ have a more uniform Al distribution that would form a protective alumina layer to prevent destructive oxidation.

4.6 Conclusion

The cathodic arc deposition technique was used to synthesize TiN/Ti_xAl_{1-x}N multilayer coatings. Often droplets with a core-shell structure spreading over

the coatings were observed leading to rough surfaces. Λ varied inversely with substrate holder rotation speed and was a key factor in structure evolution and property optimization. By decreasing Λ from 45 nm to 14 nm, two compositionally distinct rock-salt fcc phases were consolidated into a superlattice. Moreover, the coatings contain columnar grains with $\langle 111 \rangle$ preferred orientation, connected by low-angle grain boundaries, that became more pronounced at shorter Λ .

Mechanical properties also varied with Λ . The optimized hardness and Young's modulus, $H = 39 \pm 4$ GPa and $E = 503 \pm 40$ GPa, were obtained when $\Lambda = 13$ nm, and are higher than single phase TiN and Ti-Al-N coatings and other Λ multilayer coatings. The critical factors for hardness enhancement were the nanolayered structure, interface width and compositional contrast that were all influenced by Λ . Moreover, coating wear resistance was improved by decreasing Λ due to the increased concentration of multilayer interfaces serving as crack propagation barriers.

References:

- [1] R. Buhl, H. K. Pulker and E. Moll, *Thin Solid Films*, **1981**, 80, 265-270.
- [2] S. Zhang and W. Zhu, *J. Mater. Process. Technol.*, **1993**, 39, 165-177.
- [3] W. Olbrich, J. Fessmann, G. Kampschulte and J. Ebberink, *Surf. Coat. Technol.*, **1991**, 49, 258-262.
- [4] M. Wittmer, J. Noser and H. Melchior, *J. Appl. Phys.*, **1981**, 52, 6659-6664.
- [5] W. D. Münz, *J. Vac. Sci. Technol., A*, **1986**, 4, 2717-2725.
- [6] Y. C. Chim, X. Z. Ding, X. T. Zeng and S. Zhang, *Thin Solid Films*, **2009**, 517, 4845-4849.
- [7] H. Ichimura and A. Kawana, *J. Mater. Res.*, **1993**, 8, 1093-1100.
- [8] P. C. Yashar and W. D. Sproul, *Vacuum*, **1999**, 55, 179-190.
- [9] J. Musil, *Surf. Coat. Technol.*, **2000**, 125, 322-330.

- [10] M. Shinn and S. A. Barnett, *Appl. Phys. Lett.*, **1994**, 64, 61-63.
- [11] M. Kato, T. Mori and L. H. Schwartz, *Acta Metall.*, **1980**, 28, 285-290.
- [12] R. C. Cammarata, *Scripta Metallurgica*, **1986**, 20, 479-486.
- [13] M. Shinn, L. Hultman and S. A. Barnett, *J. Mater. Res.*, **1992**, 7, 901-911.
- [14] F. Sanchette, C. Ducros, T. Schmitt, P. Steyer and A. Billard, *Surf. Coat. Technol.*, **2011**, 205, 5444-5453.
- [15] W. C. Oliver and G. M. Pharr, *J. Mater. Res.*, **1992**, 7, 1564-1583.
- [16] H. Bückle, *Metallurgical Reviews*, **1959**, 4, 49-100.
- [17] C. Ducros, C. Cayron and F. Sanchette, *Surf. Coat. Technol.*, **2006**, 201, 136-142.
- [18] H. Ljungcrantz, L. Hultman, J. E. Sundgren, G. Håkansson and L. Karlsson, *Surf. Coat. Technol.*, **1994**, 63, 123-128.
- [19] M.-H. Shiao and F.-S. Shieu, *J. Vac. Sci. Technol., A*, **2001**, 19, 703-705.
- [20] M. Pohler, R. Franz, J. Ramm, P. Polcik and C. Mitterer, *Surf. Coat. Technol.*, **2011**, 206, 1454-1460.
- [21] A. H. Eltoukhy and J. E. Greene, *J. Appl. Phys.*, **1979**, 50, 505-517.
- [22] P. B. Barna and M. Adamik, *Thin Solid Films*, **1998**, 317, 27-33.
- [23] H. C. Barshilia, K. S. Rajam and D. V. Sridhara Rao, *Surf. Coat. Technol.*, **2006**, 200, 4586-4593.
- [24] M. K. Samani, X. Z. Ding, N. Khosravian, B. Amin-Ahmadi, Y. Yi, G. Chen, E. C. Neyts, A. Bogaerts and B. K. Tay, *Thin Solid Films*, **2015**, 578, 133-138.
- [25] J. L. Murray, *Metall. Trans. A*, 19, 243-247.
- [26] A. Madan, P. Yashar, M. Shinn and S. A. Barnett, *Thin Solid Films*, **1997**, 302, 147-154.
- [27] K. Yoshii, H. Takagi, M. Umeno and H. Kawabe, *Metall. Trans. A*, 15, 1273-1280.
- [28] P. B. Mirkarimi, S. A. Barnett, K. M. Hubbard, T. R. Jarvis and L. Hultman, *J. Mater. Res.*, **1994**, 9, 1456-1467.

- [29] J. S. Koehler, *Physical Review B*, **1970**, 2, 547-551.
- [30] X. Chu and S. A. Barnett, *J. Appl. Phys.*, **1995**, 77, 4403-4411.
- [31] F. Lomello, F. Sanchette, F. Schuster, M. Tabarant and A. Billard, *Surf. Coat. Technol.*, **2013**, 224, 77-81.
- [32] A. Leyland and A. Matthews, *Wear*, **2000**, 246, 1-11.
- [33] H. Holleck and V. Schier, *Surf. Coat. Technol.*, **1995**, 76-77, Part 1, 328-336.
- [34] C. Mendibide, P. Steyer, J. Fontaine and P. Goudeau, *Surf. Coat. Technol.*, **2006**, 201, 4119-4124.

Chapter 5

The yttrium effect on the structure and properties of nano-multilayered $Ti_{1-x-y}Al_xY_yN$ coatings

Yttrium was alloyed in Ti-Al-N multilayer coatings by cathodic arc deposition. The yttrium distribution, affecting grain nucleation and secondary phase formation, is dependent on the multilayer period (Λ) and Y content. When the Y concentration was set at 2.4 at% and Λ varied from 5.5 nm to 24 nm, the microstructure evolved from crossed acicular grains to highly $\langle 200 \rangle$ textured equiaxial grains, with the longer periods showing degraded hardness and Young's modulus. For fixed Λ , the Y content was varied from 0 to 2.4 at%. In this case, $Ti_{1-x}Al_xN$ coatings present $\langle 111 \rangle$ textured columnar grains in contrast to the acicular morphology of $Ti_{0.976-x}Al_xY_{0.024}N$, where Y not only replaced Ti and Al in rock-salt grains, but promoted the formation of a wurzite phase. The hardness was enhanced at higher content Y, while adhesion and wear resistance initially were reduced at 1.2 at% Y and then rose at 2.4 at% Y. At all compositions, Y retarded oxidation effectively at 800 ° C in air because at high temperature Y is sequestered from the rock-salt lattice to grain boundaries, to effectively attenuate oxygen diffusion pathways.

5.1 Introduction

In order to satisfy more stringent requirements from the machining industry, there is considerable interest in fabricating protective Ti-Al-N coatings by physical vapour deposition (PVD) to deliver superior mechanical properties, wear resistance and thermal stability [1-4]. From a structural perspective, nano-scale multilayered TiN/(Ti, Al)N coatings produced by various PVD techniques have shown promise [5, 6], as presented in Chapter 4. The primary objective is to generate superlattices of alternating lattice-mismatched rock-salt TiN and (Ti, Al)N layers to enhance mechanical properties beyond single-phase bulk coatings. From a chemical perspective, numerous elements, such as Si [7, 8], Cr [9] and Y [10], can be alloyed with Ti-Al-N coatings to improve thermal stability and oxidation resistance, while with vanadium wear resistance can be improved [11]. Yttrium has a high affinity with oxygen and forms dense oxides [12]. This can be exploited by chemically incorporating Y into TiN coating grain boundaries to getter oxygen, and block Ti and Al diffusion paths with yttrium oxide leading to oxidation resistance [13]. Meanwhile, Y alters the Ti-Al-N coating microstructure by accelerating renucleation and generating wurtzite as a secondary phase in Al-rich coatings, which particularly effects mechanical properties [14, 15]. The deposition configuration and processing parameters significantly affect Y content and distribution, and understanding how these influence the Ti-Al-Y-N coating is a pre-requisite to developing reliable deposition processes and delivering superior coating performances.

In this chapter, structure and chemistry were systematically varied by adding Y into nanolayered TiN/(Ti,Al)N with concurrent adjustment of deposition processes, and coating properties monitored to find the optimum fabrication parameters. In this way, it is demonstrated that Y content adjustment and multilayer period (Λ) are key factors controlling $Ti_{1-x-y}Al_xY_yN$ coating performance. Both Ti-Al-Y-N coatings deposited by a combination of cathodic

arc deposition (CAD) and magnetron sputtering (MS) were prepared. CAD was used to generate Ti and Ti-Al plasmas while Y was ionized by magnetron sputtering. The mechanical properties, adhesion, wear resistance and oxidation resistance were analysed as a function of Y content and Λ , together with the evolution of microstructure.

5.2 Experimental methods

5.2.1 Sample deposition

The depositions were performed in a PLATIT planar device equipped with three targets and a two-fold rotary substrate holder. The Ti and $\text{Al}_{0.6}\text{Ti}_{0.4}$ alloy targets were arc evaporated and DC magnetron sputtering used for the pure Y target. For mechanical and tribology tests depositions were made on AISI M2 HSS substrates, while for tensile and oxidation studies the substrate was 304L stainless steel. These substrates were polished to a mirror finish with 1 μm alumina, then cleaned by alcohol and degreased with soap. Substrates were etched in the deposition chamber with an argon plasma (time = 2 min / pressure ≈ 0.3 Pa / bias $\approx -800\text{V}$) and Ti plasma (10 min / ~ 1 Pa / -700V) consecutively. This was followed by deposition of Ti (~ 0.5 μm) and TiN layers (~ 0.5 μm) to improve adherence. The multilayer deposition parameters are listed in Table 5.1. Initially, the Y target power supply was set to 0 W, 1500 W and 2300 W when the substrate rotation speed was fixed at 5 revolutions per minute (r.p.m). Subsequently, the rotation speed was varied from 1 r.p.m to 5 r.p.m with the Y target power fixed to 2300 W.

Table 5.1 Parameters for $Ti_{1-x-y}Al_xY_yN$ coating deposition

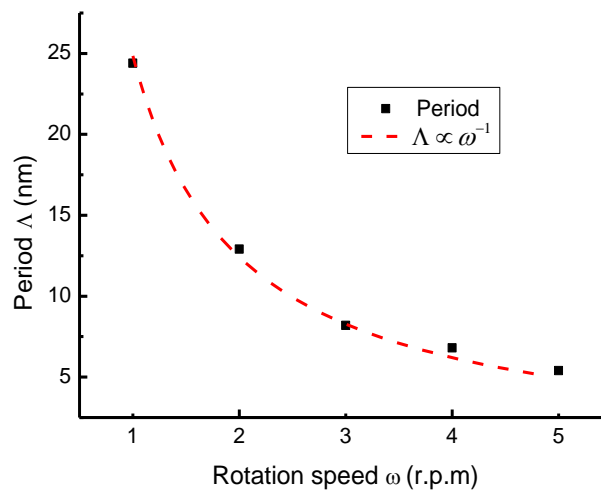
Arc target current	Ti target: 55 A Al ₆₀ Ti ₄₀ target: 55 A
DC power	Ytarget: 0 W, 1500 W & 2300 W
Substrate rotation speed	1 - 5 r.p.m
Bias voltage	- 100 V
Nitrogen flow	110 sccm
Pressure	~ 3 Pa
Deposition time	5600 s
Deposition temperature	~ 400 °C
Multilayer thickness	2 ~ 3 μm

5.2.2 Coating characterization

Scanning electron microscopy (SEM) (FE-SEM JEOL 7800F) was employed to observe surface and cross-section morphology. The coating composition measured by energy dispersive X-ray analysis (EDX) (Bruker) (Table 5.2), suggests Y content was determined by target power, but not influenced by substrate rotation speed. The coatings were doped with 0 at%, 1.2 at% and 2.4 at% Y (hereafter referred as $Ti_{1-x}Al_xN$, $Ti_{0.988-x}Al_xY_{0.012}N$ and $Ti_{0.976-x}Al_xY_{0.024}$, $x \sim 0.4$) by powering the Y target to 0 W, 1500 W and 2300 W respectively. A Bruker D8 powder X-ray diffractometer (XRD) with Bragg-Brentano geometry was used to record coating patterns in θ - 2θ mode (CoK α 1 radiation, $\lambda=1.788970\text{\AA}$). The microstructures were observed by transmission electron microscopy (TEM) (JEOL JEM-2100F) equipped with scanning transmission (STEM) capability and EDX at an accelerating voltage of 200 kV. To obtain electron transparent samples, coatings were deposited on copper foils, glued face to face and cross-sectioned with a precision saw. These samples were thinned to electron beam transparency by mechanical polishing and ion milling (Precision Ion Polishing System, Gatan). The period Λ was controlled directly by adjusting the substrate rotation speed (Table 5.3), as illustrated in Figure 5.1, consistent with earlier results [16] and Chapter 4.

Table 5.2 Coatings composition at various deposition parameters

Y target Power (W)	Substrate rotation speed (r.p.m)	x (Al)	1-x-y (Ti)	y (Y)
2300	1	0.393(8)	0.582(9)	0.026(1)
2300	2	0.389(3)	0.586(3)	0.025(1)
2300	3	0.379(2)	0.598(2)	0.023(0)
2300	4	0.381(5)	0.595(5)	0.024(0)
2300	5	0.381(3)	0.595(3)	0.024(0)
1500	5	0.385(6)	0.603(6)	0.012(0)
0	5	0.398(4)	0.602(4)	0

**Figure 5.1** Coating Λ versus the substrate rotation speed in deposition as Y target fixed at 2300 W.

The coating hardness and Young's modulus were measured and derived from nanoindentation (NHT-CSM). A Berkovich diamond tip was employed and the calculations based on the Oliver and Pharr method [17] by averaging 10 indentations. As discussed in Chapter 3, the indentation depth was set to 200 nm so that the substrate would not influence the hardness result if the penetration did not exceed 10 % of the coating thickness [18].

Tensile tests, coupled with *in-situ* SEM were used to evaluate coating adhesion deposited on stainless steel substrates. Samples were loaded on the tensile unit

inside the SEM chamber [19], and force applied at a stain rate of 0.05 mm / min, with the test stopped when the strain reached 30%. *In-situ* SEM images were recorded at 200 \times magnification and the strain versus stress curve correlated with cracking images.

Coating wear resistance was evaluated by the ball-on-disc test (CSM tribometer) at room temperature conducted at a relative humidity of 40% - 50%. The WC/Co counter ball was 6 mm in diameter and slid on the coating surface in 3 mm radius circles at a velocity of 100 mm/s. The sliding distance was 188 m for 10000 laps. A constant load of 10 N was applied on the counter ball, with the friction coefficient recorded along with the sliding distance. The wear scar profiles were examined by a profilometer (ALTISURF500) with a height resolution of 10 nm. The scanning speed was 15 μ m/s.

In order to assess oxidation resistance, 2 cm \times 1 cm \times 1 mm stainless steel pieces were completely coated and annealed at 800 $^{\circ}$ C for 10 hours in air. XRD patterns of the annealed samples were measured by a Bruker Advance D8 diffractometer in Bragg–Brentano geometry using Cu $K\alpha$ radiation ($\lambda_{av} = 1.54187$ Å). The weight variation after annealing was also recorded.

5.3 Coating structural analysis

5.3.1 X-ray diffraction

XRD of the $Ti_{1-x-y}Al_xY_yN$ coatings with $y = 0, 0.012$ and 0.024 prepared at 5 r.p.m confirm the multilayers possess a rock-salt fcc structure, with substrate and Ti buffer layer reflections also visible (Figure 5.2). Coatings show a pronounced $\langle 111 \rangle$ preferred orientation. As Y increased from 0 to 2.4 at%, the $\langle 111 \rangle$ texture weakens until a (200) reflection appears in $Ti_{0.976-x}Al_xY_{0.024}N$, suggesting Y decreases the crystal size as smaller grains show more rapid $\langle 200 \rangle$

growth. Simultaneously, the (111) reflection shifts to a smaller 2θ as larger Y (2.12 Å) substitute displaces smaller Al (1.21 Å) and Ti (1.76 Å) atoms. The fitted lattice parameter of $\text{Ti}_{0.976-x}\text{Al}_x\text{Y}_{0.024}$ is $a = 4.23(1)$ Å, without the wurtzite phase, commonly observed in Ti-Al-Y-N coatings when Al content is high, below the limits of detection.

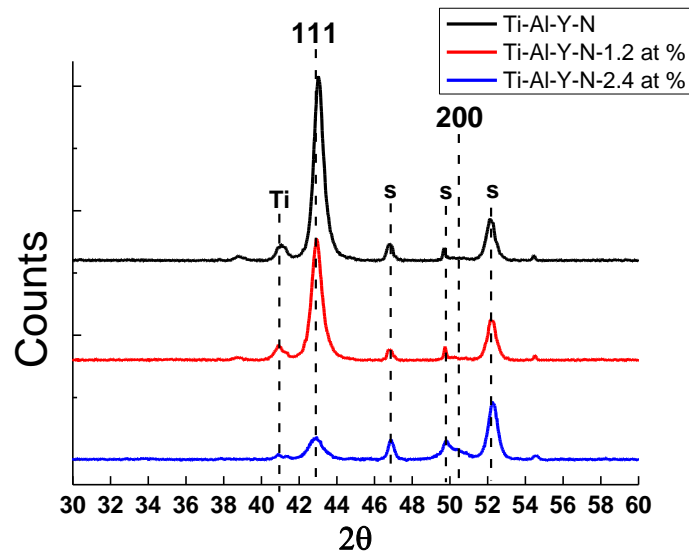


Figure 5.2 XRD patterns of 5 r.p.m Ti-Al-Y-N coatings with 0, 1.2 at% and 2.4 at% Y in rock-salt fcc structure with $\langle 111 \rangle$ texture

$\text{Ti}_{0.976-x}\text{Al}_x\text{Y}_{0.024}$ coatings contain both (111) and (200) reflections whose relative intensity varied as a function of superlattice spacing Λ (Figure 5.3). The rock-salt TiN non-textured powder pattern (ICSD-644780) is presented for comparison and the texture coefficient (T^*) in percentage of $\langle 111 \rangle$ and $\langle 200 \rangle$ is calculated based on reflection integrated intensity. According to the T^* calculation if samples are not textured, then $T^*\%_{(200)} = T^*\%_{(111)} = 50\%$. For coatings deposited at 1 to 5 r.p.m, the corresponding Λ and $T^*\%$ of $\langle 111 \rangle$, $\langle 200 \rangle$ change systematically (Table 5.3), such that as Λ decreases, the texture favours $\langle 111 \rangle$ rather than $\langle 200 \rangle$. The 1 r.p.m ($\Lambda = 24$ nm) and the 2 r.p.m coatings ($\Lambda = 13$ nm) both present strong $\langle 200 \rangle$ texture ($T^*\%_{(200)} > 95\%$) with a trace of the (111) reflection, while the 2 r.p.m coating has wider reflections

compared to the 1 r.p.m coating. The measured (200) reflection full width at half maxima (FWHM) of the 2 r.p.m coating is 1.5° and that of the 1 r.p.m is 1.3° , as a consequence of reduced crystal size. The (200) reflection intensity decreases significantly by increasing rotation speed from 2 to 3 r.p.m ($\Lambda = 8$ nm). In the 3 r.p.m and 4 r.p.m coating ($\Lambda = 7$ nm) patterns preferred orientation is not pronounced although (200) is relatively weaker than (111) ($T^*_{(200)} / T^*_{(111)} \approx 75 / 25$). However, the $\langle 111 \rangle$ texture becomes predominant as the rotation speed was higher than 5 r.p.m (inclusive), namely $\Lambda \leq 5.5$ nm ($T^*_{(200)} / T^*_{(111)} \approx 30 / 70$).

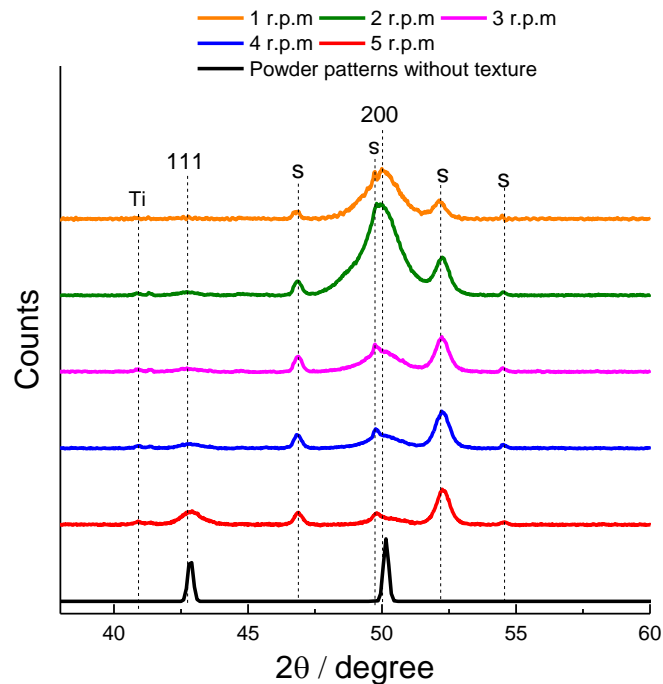


Figure 5.3 XRD patterns of 1 - 5 r.p.m $\text{Ti}_{0.976-x}\text{Al}_x\text{Y}_{0.024}$ coatings and random TiN powder (ICSD-644780) pattern for the (111) and (200) reflection intensity comparison.

Table 5.3 Substrate rotation speed, corresponding Λ and T* % of $\langle 111 \rangle$ and $\langle 200 \rangle$ in $Ti_{0.976-x}Al_xY_{0.024}$ coatings

Substrate rotation speed (r.p.m)	Period (nm)	T* in percentage (%)	
		$\langle 111 \rangle$	$\langle 200 \rangle$
1	24	3	97
2	13	4	96
3	8	28	72
4	7	26	74
5	5.5	68	32

5.3.2 TEM

$Ti_{1-x}Al_xN$, $Ti_{0.988-x}Al_xY_{0.012}N$ and $Ti_{0.976-x}Al_xY_{0.024}N$ coatings deposited at 5 r.p.m have $\Lambda = 5.5$ nm. The dark field TEM (DFTEM) images and corresponding selected area electron diffraction (SAED) patterns of coating cross sections show that with increasing Y content grain morphology becomes less columnar and more acicular, and texture is less evident as systematic rows of reflections merge into diffraction rings (Figure 5.4 and Figure 5.5). The a-cell edge of $Ti_{0.976-x}Al_xY_{0.024}$ was measured to be 4.2 Å from SAED, consistent with the XRD result. The columnar grains of $Ti_{1-x}Al_xN$ are 100 – 200 nm in diameter and preferentially grow in $\langle 111 \rangle$ perpendicular to the substrate surface across entire thickness. With 1.2 at% Y, $Ti_{0.988-x}Al_xY_{0.012}N$ grains reduce to 40 – 80 nm in diameter and $\langle 111 \rangle$ texture is still dominant. However, for 2.4 at% Y addition the grain morphology altered significantly to crossed acicular grains that were 20 – 30 nm in diameter and connected by higher angle grain boundaries. These crossed grains grow along $\langle 111 \rangle$ and $\langle 200 \rangle$ consistent as also observed by XRD.

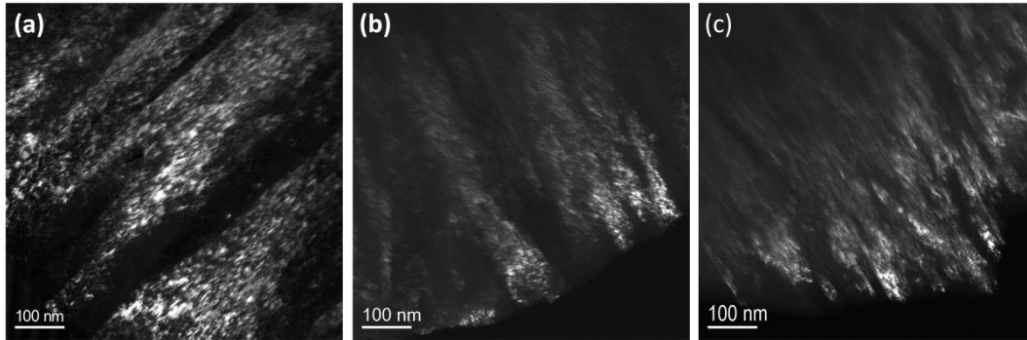


Figure 5.4 Cross-section DFTEM images of 5 r.p.m (a) $\text{Ti}_{1-x}\text{Al}_x\text{N}$, (b) $\text{Ti}_{0.988-x}\text{Al}_x\text{Y}_{0.012}\text{N}$ and (c) $\text{Ti}_{0.976-x}\text{Al}_x\text{Y}_{0.024}\text{N}$ coatings ($\Lambda = 5.5$ nm) of different sizes and grain morphologies

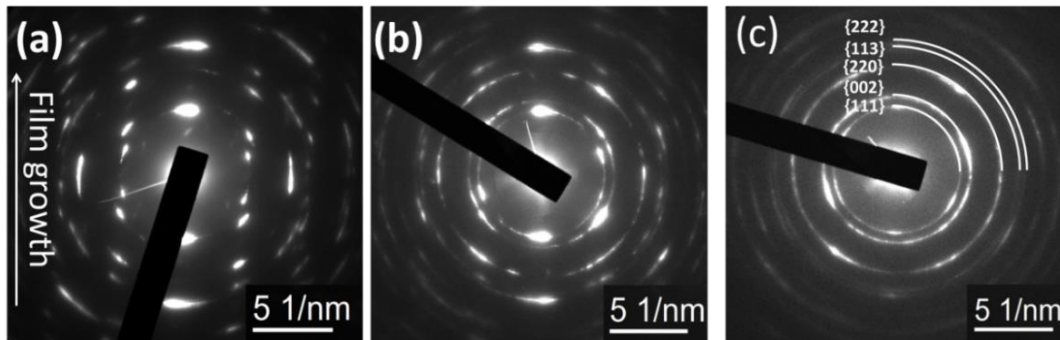


Figure 5.5 Cross-section SAED of 5 r.p.m (a) $\text{Ti}_{1-x}\text{Al}_x\text{N}$, (b) $\text{Ti}_{0.988-x}\text{Al}_x\text{Y}_{0.012}\text{N}$ and (c) $\text{Ti}_{0.976-x}\text{Al}_x\text{Y}_{0.024}\text{N}$ coatings ($\Lambda = 5.5$ nm)

The textural variation with increasing Y can be explained by strain and surface energy theory. According to Pelleg et al. [20], the texture of very thin films is determined by the planes of lowest surface energy, while the texture of thick films develops along the lowest strain energy planes. For example, $\{100\}$ planes of rock-salt fcc TiN are the most close-packed planes and have the lowest surface energy. If the film is extremely thin the grain presents $\langle 100 \rangle$ preferred orientation. By comparison, when the grain is large strain energy becomes a major factor during grain growth. Thus $\langle 111 \rangle$ is the dominant texture as $\{111\}$ planes are of the lowest strain energy. Likewise, in this work, $\text{Ti}_{1-x}\text{Al}_x\text{N}$ with $\Lambda = 5.5$ nm is composed of long columnar grains which tend to grow in the favourable $\langle 111 \rangle$ orientation due to its lower strain energy. The weakened $\langle 111 \rangle$ texture, and the presence of $\langle 200 \rangle$ texture in the 2.4 at% Y

coating, are attributed to the finer grains as immobile Y hindered competitive grain growth in $\langle 111 \rangle$ and initiated massive renucleation.

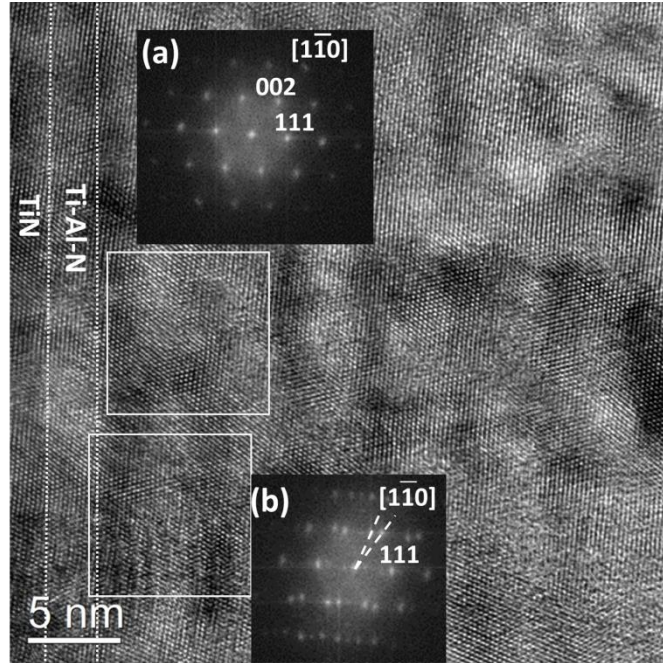


Figure 5.6 $\text{Ti}_{0.988-x}\text{Al}_x\text{Y}_{0.012}\text{N}$ ($\Lambda = 5.5$ nm) coating at high magnification; Crystallite FFT (a) and low-angle grain boundary FFT (b).

Lattice images of $\text{Ti}_{0.988-x}\text{Al}_x\text{Y}_{0.012}\text{N}$ coatings ($\Lambda = 5.5$ nm) (Figure 5.6) by high resolution transmission microscopy (HRTEM) show alternating dark TiN-rich layer and bright Ti-Al-N-rich layer contrast. Layers rich in Y are not visible because of its atomic scale dispersion in TiN and Ti-Al-N. The fast Fourier transformation (FFT) of the upper squared area is consistent with the rock salt fcc structure viewed along $[1-10]$ with layers growing epitaxially along $\langle 111 \rangle$ (Figure 5.6 inset (a)). The lower squared area in the same $[1-10]$ zone axis shows a small misorientation between two patterns (Figure 5.6 (inset (b))) suggesting overlapped crystallites are connected by low-angle grain boundaries.

Yttrium-rich layers were not found in $\text{Ti}_{0.988-x}\text{Al}_x\text{Y}_{0.012}\text{N}$ due to the short Λ ($\Lambda = 5.5$ nm) and slow deposition rate of the DC-powered Y target favoring Y incorporation in the TiN and Ti-Al-N layers (Figure 5.6). The deposition

chamber configuration means the substrate passes in front of targets in the order $\cdots \text{Ti} - \text{Al}_{0.6}\text{Ti}_{0.4} - \text{Y} - \cdots$ and thus it was assumed Y would not diffuse into the layers uniformly. In order to confirm Y incorporation, and its influence on multilayer structure, another area of the $\text{Ti}_{0.988-x}\text{Al}_x\text{Y}_{0.012}\text{N}$ coating was chosen for analysis (Figure 5.7). The area in (a) was transformed by FFT as shown in (b), and after indexing, a superposition of two patterns in a biphasic region where a [11-2] rock-salt crystallite (referred to as r in following context) with $\langle 111 \rangle$ perpendicular to the layer surface, overlays a [311] wurtzite-type structure (referred to as w in the following context). The $(10\bar{3})_w$ reflection overlaps with the $(2\bar{2}0)_r$ reflection, suggesting wurtzite nucleated on the rock-salt $\{220\}$ planes. Insets (c) and (d) were processed images obtained by inverting FFT of the circled reflections and non-circled reflections respectively to differentiate the two phases. In this manner, the lattice in (c) is ascribed to wurtzite while crystal (d) is a rock-salt crystallite with the boundary between the two crystallites highlighted by dashed line in inset (a).

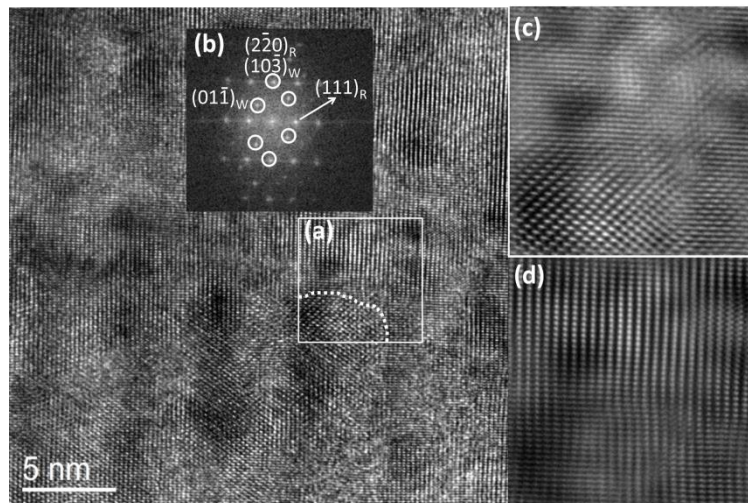


Figure 5.7 Wurtzite crystallite indicated in high resolution TEM of $\text{Ti}_{0.988-x}\text{Al}_x\text{Y}_{0.012}\text{N}$ ($\Lambda = 5.5$ nm); (b) is FFT of selected area (a) including two sets of patterns belong to wurtzite and rock-salt phases; (c) is inversed FFT of circled wurtzite reflection in (b) and (d) is non-circled rock-salt reflections.

The wurtzite crystallite was probably AlN whose separation was promoted by Y addition. TiN processed by PVD is commonly rock-salt ($a = 4.24 \text{ \AA}$) (referred to as TiN_R) [21], while AlN is wurtzite ($a = 3.11 \text{ \AA}$, $c = 4.98 \text{ \AA}$) (referred to as AlN_W) [22]. The bulk, cubic $Ti_{1-x}Al_xN$ (referred to as $Ti-Al-N_R$) forms when $x \leq \sim 0.70$, beyond which AlN_W separates according to experiment [23-25] and first-principles simulations [26]. Yttrium may alter Al distribution, thus the solid solubility of Al in $Ti-Al-N_R$ varies [27]. Incorporating Y into $Ti_{1-x}Al_xN$ promotes AlN_W formation and reduces the solid solubility of Al in TiN_R [28, 29]. This is consistent with Riedl et al. [3] where AlN_W was detected in $Ti_{0.41}Al_{0.57}Y_{0.02}N$ by XRD. In this study, wurtzite was not detected by XRD in $Ti_{1-x-y}Al_xY_yN$ ($y = 0, 0.012$ and 0.024), but deposition by rotating the substrate through successive targets created Y-rich regions next to Ti-Al-N layers where AlN wurtzite crystallites were stabilized by Y segregation (Figure 5.7). In this case, the wurtzite is epitaxial to rock-salt such that $\{1-10\}_R // \{10-3\}_W$, $\langle 11-2 \rangle_R // \langle 311 \rangle_W$. The coalescence of AlN_W and $Ti-Al-N_R$ was also reported by Szekely et al. [15] in $(Ti_{1-x}Al_x)_{1-y}Y_yN$ ($y = 0.02$; $0.72 < Ti/Al < 0.88$) with the $\langle 001 \rangle_W // \langle 111 \rangle_R$ epitaxy. The epitaxial relationship between AlN_W and $Ti-Al-N_R$ accompanied by $Ti-Al-N_R$ renucleation gives rise to crossed acicular grain morphology and smaller crystals as Y content increases. Therefore, it was concluded that $Ti_{0.988-x}Al_xY_{0.012}N$ and $Ti_{0.976-x}Al_xY_{0.024}N$ coatings of 5.5 nm period are primarily rock-salt fcc, but Y decreases the grain size, weakens $\langle 111 \rangle$ epitaxial growth, modifies grain morphology and induce wurtzite crystallisation. In combination, these factors influence mechanical and thermal performance.

As discussed in 5.3.1, if the Y addition was fixed at 2.4 at% and the substrate rotation speed varied from 5 r.p.m to 1 r.p.m the coating texture changed from $\langle 111 \rangle$ to $\langle 200 \rangle$ because the Y-rich region expanded as Λ increased disrupting grain epitaxy (Figure 5.3). Indeed, $\langle 111 \rangle$ texture was absent when Λ increased to 7 nm (4 r.p.m) from 5.5 nm (5 r.p.m) and preferred orientation was not prominent in 4 r.p.m ($\Lambda = 7 \text{ nm}$) and 3 r.p.m ($\Lambda = 8 \text{ nm}$) coatings, but rather

$\langle 200 \rangle$ was evident in 2 r.p.m ($\Lambda = 13$ nm). Figure 5.8 (a) is the DFTEM image of the 3 r.p.m ($\Lambda = 8$ nm) coating with the corresponding SAED inset, where material shows misoriented acicular grains. The grains were weakly $\langle 200 \rangle$ textured resulting in partial electron diffraction rings. By comparison, the 2 r.p.m coating ($\Lambda = 13$ nm) shows equiaxed grains highly textured along $\langle 200 \rangle$ instead of the acicular morphology, which are separated in each period by visible Y-rich layers (Figure 5.8 (b)). Thus the grain length is ~ 12 nm which equals to Λ minus Y-rich layer thickness. Finally, the 1 r.p.m coating ($\Lambda = 24$ nm) is composed principally $\langle 200 \rangle$ textured equiaxed grains, ~ 20 nm in diameter.

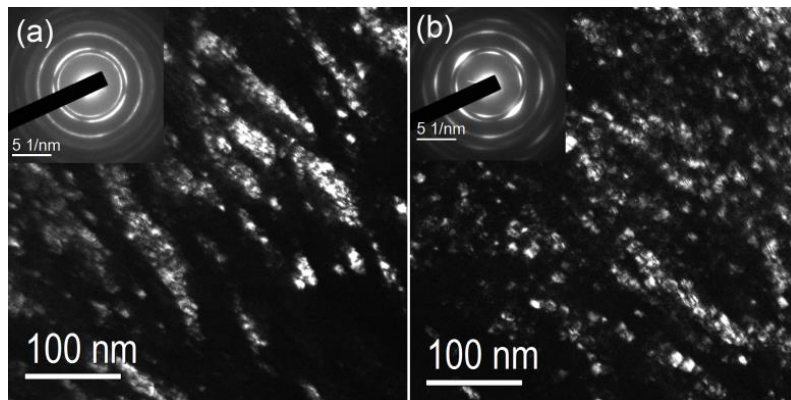


Figure 5.8 DFTEM images and corresponding SAED of (a) 3 r.p.m coating ($\Lambda = 8$ nm) in acicular grain morphology and (b) 2 r.p.m coating ($\Lambda = 13$ nm) in equiaxed grain morphology.

In the 1 r.p.m coating the Y-rich layers were confirmed by HRTEM and EDX mapping (Figure 5.9). At low magnification, TEM shows $\Lambda = 24$ nm and in each period grains nucleate from TiN (dark contrast), then extended to the Ti-Al-N layer (bright contrast), and finally were blocked in the brightest Y-rich layer (Figure 5.9 (b) and (c)). The rock-salt crystallites renucleate adjacent to the Y-rich layers, considered as period boundaries (Figure 5.9 (a) is a higher magnification of the squared area in Figure 5.9 (b)). In the Ti-Al-N layer, the squared area $[001]$ zone axis crystal shows a crystal with $[200]$ perpendicular to the coating surface, while across the Y-rich layer, a new crystallite in the TiN

layer was found in [110] orientation and preserved [200] growth orientation. The $\langle 200 \rangle$ texture has the lowest surface energy as discussed above in fine equiaxed grains. In Y-rich layers, the crystal lattice could not be resolved (Figure 5.9 (a)) while elsewhere wurtzite was found (Figure 5.10). EDX analysis with STEM imaging confirmed Y-rich layers are sandwiched between Ti-Al-N and TiN layers (Figure 5.9 (c)-(e)). In Ti-Al-N layers Ti: Al \approx 40: 60 and Ti is above 90 at% in TiN layers consistent with the target compositions. In the Y-rich layer Ti: Al: Y \approx 45 at%: 45 at%: 10 at% and according to the ternary phase diagram (Figure 2.10) the wurtzite phase Ti-Al-Y-N_w may be expected.

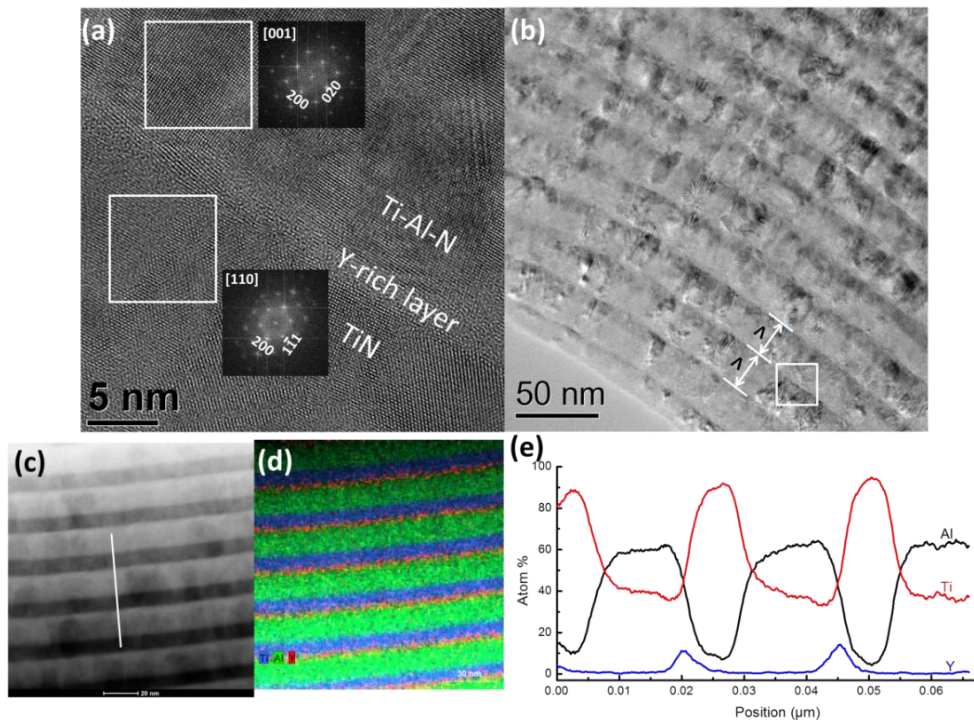


Figure 5.9 (a) Zoomed in HRTEM image of 1 r.p.m coating squared area in (b), considering the Y-rich layer as period boundaries which induce renucleation; STEM bright field image (c) and corresponding EDX element maps (d) indicating multilayer structure; The element profile (e) is along the line in (c) from the bottom up, indicating the layer deposition sequence.

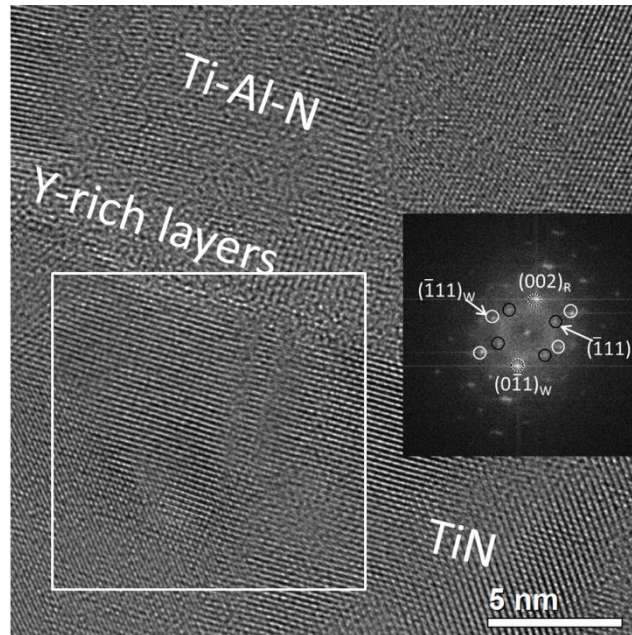


Figure 5.10 The wurtzite phase presence in 1 r.p.m coating proved by HRTEM with FFT diffractions.

5.4 Coating properties

5.4.1 Hardness and Young's modulus

The mechanical properties of the $\text{Ti}_{1-x-y}\text{Al}_x\text{Y}_y\text{N}$ coatings were modified by both Y content and Λ . First, the 5 r.p.m coatings with $\Lambda = 5.5$ nm and Y content 0 at%, 1.2 at% and 2.4 at% gave the Young's modulus 487 ± 115 GPa for $\text{Ti}_{1-x}\text{Al}_x\text{N}$, 521 ± 65 GPa for $\text{Ti}_{0.988-x}\text{Al}_x\text{Y}_{0.012}\text{N}$ and 490 ± 46 GPa for $\text{Ti}_{0.976-x}\text{Al}_x\text{Y}_{0.024}\text{N}$. The absence of evident variation suggests small Y incorporation did not significantly influence the compound intrinsic bonding status (Figure 5.11 (a)). However, the hardness is 29 ± 7 GPa for $\text{Ti}_{1-x}\text{Al}_x\text{N}$, 37 ± 3 GPa for $\text{Ti}_{0.988-x}\text{Al}_x\text{Y}_{0.012}\text{N}$ and 41 ± 3 GPa for $\text{Ti}_{0.976-x}\text{Al}_x\text{Y}_{0.024}\text{N}$, demonstrating an increasing tendency with Y addition. The residual stress was obtained through an iron foil bending measurement after deposition and calculation based on the Stoney's equation (Figure 5.11 (b)). As is common in CAD coatings compressive stress is retained due to the production of point defects by intense

plasma bombardment during deposition. The compressive stress increased from 4.7 GPa to 10.7 GPa as Y content increased from 0 to 1.2 at%, but decreased to 9.3 GPa with 2.4 at% Y addition.

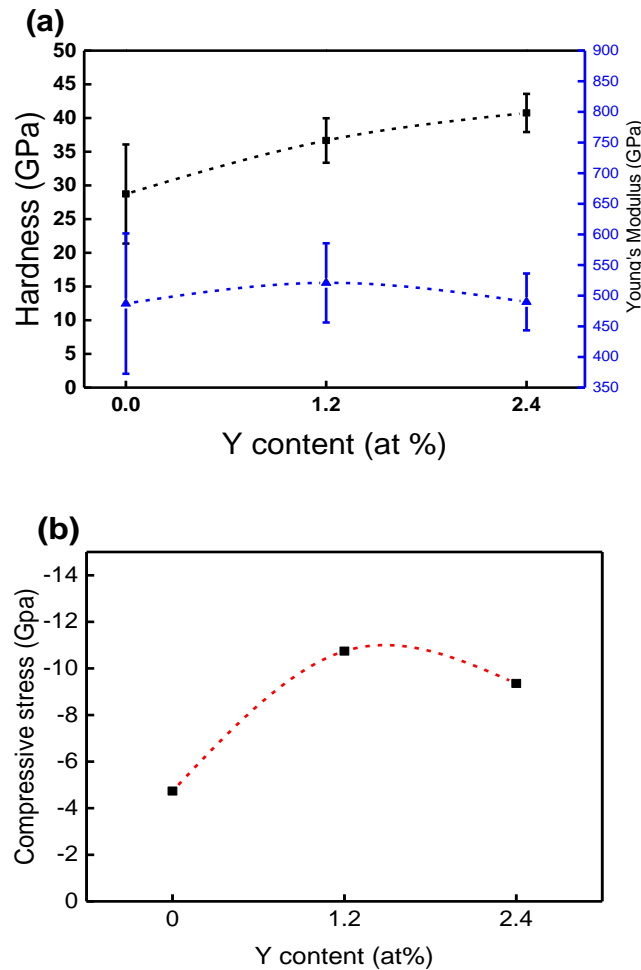


Figure 5.11 With y increasing in 5 r.p.m $Ti_{1-x-y}Al_xY_yN$ coatings ($\Lambda = 5.5$ nm) hardness and Young's modulus variation (a) and compressive stress (b)

Hardness increased together with yttrium concentration because displacing Ti or Al by Y in $Ti-Al-N_R$, hinders dislocation movement through solid solution hardening [30]. Concomitantly, significant grain size reduction also restricts dislocation movement by introducing more grain boundaries [31]. This effect would also trap compressive stress and harden the coating [32]. In this work,

the $\text{Ti}_{1-x-y}\text{Al}_x\text{Y}_y\text{N}$ coating hardness and compressive stress both increase by adding 1.2 at% Y (Figure 5.11). The hardness further improves by increasing Y from 1.2 at% to 2.4 at%, whereas the compressive stress slightly decreased. This inverse correlation between compressive stress and hardness can be attributed to grain size reduction caused by renucleation, which favours hardness enhancement while relaxing point defects and lowering the intrinsic stress through the higher frequency of grain boundaries [33].

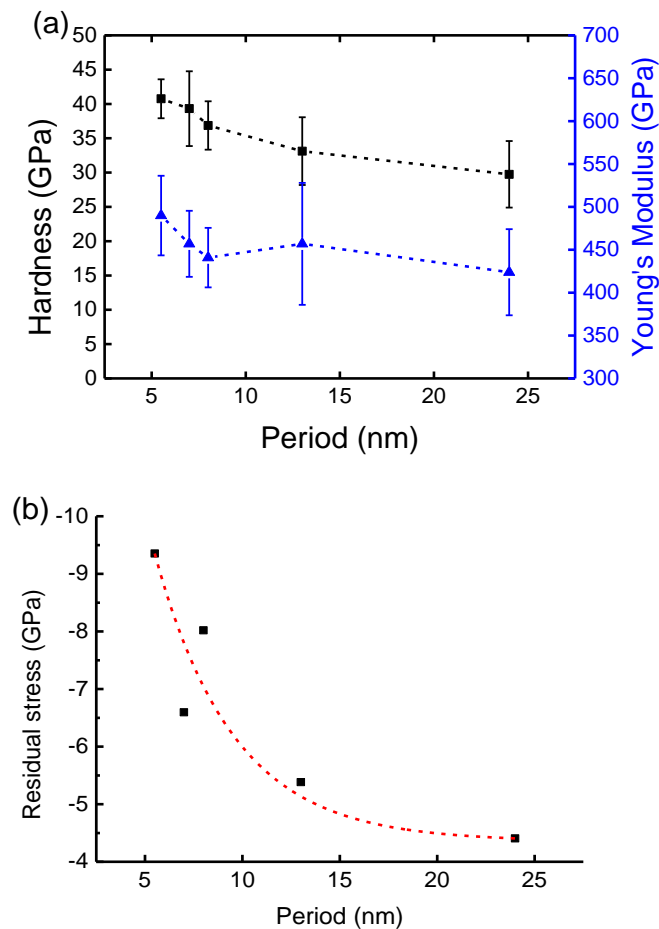


Figure 5.12 Hardness and Young's modulus (a) and compressive stress (b) of $\text{Ti}_{0.976-x}\text{Al}_x\text{Y}_{0.024}\text{N}$ coatings in different period

For $\text{Ti}_{0.976-x}\text{Al}_x\text{Y}_{0.024}\text{N}$ coatings the hardness varies inversely with Λ , such that when Λ increased from 5.5 nm to 24 nm, the hardness decreased from 41 ± 3

GPa to 30 ± 5 GPa and the Young's modulus fell from 490 ± 47 GPa to 424 ± 50 GPa (Figure 5.12 (a)). Simultaneously, the residual stress decreased as Λ increased, implying that hardness degradation correlates with intrinsic compressive stress relaxation, and can be explained by the enlargement of Y-rich layers as Λ increases. The 5 r.p.m coatings ($\Lambda = 5.5$ nm) are more evidentially $\langle 111 \rangle$ textured compared to 4 r.p.m ($\Lambda = 8$ nm) and 3 r.p.m ($\Lambda = 7$ nm) coatings (Figure 5.3). The grains in the 4 r.p.m and 3 r.p.m coatings slide and rotate along semi-coherent grain boundaries more easily under high stress where mechanical failure is initiated and degrades hardness [34]. What is more, for $\Lambda \geq 13$ nm (deposited at 2 r.p.m and 1 r.p.m) there was a visible Y-rich layer in each multilayer period, which significantly blocked epitaxial grain growth across layers and equiaxed grains formed. The Y-rich secondary (semi)crystalline phase separates equiaxed grains via semicoherent or incoherent interfaces, that lowers hardness. Therefore, it is concluded that Y was incorporated more uniformly as Λ decreased, and as its disruption on grain growth weakened, the coating showed improved mechanical properties.

5.4.2 Coating adhesion and wear resistance

Coating adhesion was evaluated by *in-situ* tensile tests. The force was applied horizontally at a strain rate of 0.05 mm / min on the ends of dog-bone shaped substrate covered by 5 r.p.m $\text{Ti}_{1-x-y}\text{Al}_x\text{Y}_y\text{N}$ coatings ($y = 0, 0.012$ and 0.024). These samples experienced several cracking stages recorded by SEM, including crack initiation, crack propagation and cross-linking, and crack opening (Figure 5.13). Surface cracks extended perpendicularly to the tensile stress direction and curved when intersecting with droplets which are common in CAD processed coatings. Moreover, when the strain was more than 10%, cracks were cross-linked by $\sim 65^\circ$ to the horizontal direction as a compressive stress was applied by the necking effect of the ductile stainless steel substrate. The cracking of different Y content coatings at strains of 3% 10% and 27%

followed the same patterns. Nevertheless, the coating adhesion can be compared by estimating the interfacial shear strength using the model of Agrawal and Raj [35]:

$$\tau = \frac{\pi\delta\sigma}{\lambda} \quad (5.2)$$

where τ (Pa) is the interfacial shear strength, δ (mm) is coating thickness, σ (Pa) is the stress starts cracking and λ (mm) is the maximum saturated crack spacing along the tensile axis. The model is applicable for coatings without intrinsic stress, that present traverse cracks during tensile testing. Therefore, τ could not be derived in this work as the coatings were under compressive stress from deposition and cross-linking cracks that formed early. However, a comparison could be made as suggested by the formula, such that under the same thickness the coating with better adhesion shows shorter distances between saturated cracks leading to a higher crack density.

In SEM backscattered electron images (BEI) of different tensile strains, the number of cracks on 10 horizontal lines were counted and averaged so that a plot of crack density (in unit of number per mm) versus strain was obtained (Figure 5.14). A comparison in 0 at%, 1.2 at% and 2.4 at% coatings show that with $< 10\%$ strain the crack density propagated at similar rates, beyond which the rate slowed. The $Ti_{0.988-x}Al_xY_{0.012}N$ coating had the lowest saturated crack density. Therefore, it is concluded that the $Ti_{1-x}Al_xN$ coating was best adhered to the substrate, while the $Ti_{0.988-x}Al_xY_{0.012}N$ showed the worst properties, which may be related to the sudden increase of compressive stress for the 1.2 at% Y addition.

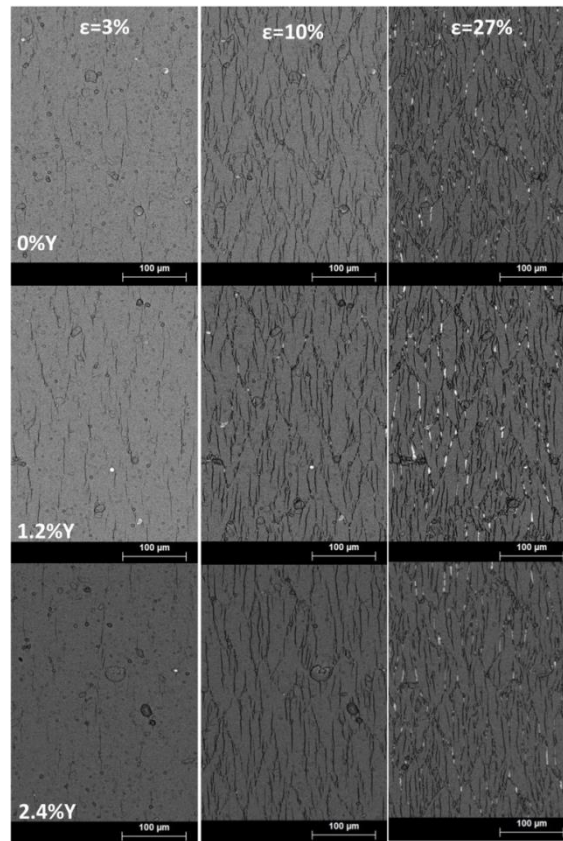


Figure 5.13 *In-situ* SEM BEI of 5 r.p.m $\text{Ti}_{1-x-y}\text{Al}_x\text{Y}_y\text{N}$ coatings ($y = 0, 0.012$ and 0.024) at tensile strain $\epsilon = 3\%$, 10% and 27% , showing the crack inset, propagation and cross-linking, and crack opening stages respectively.

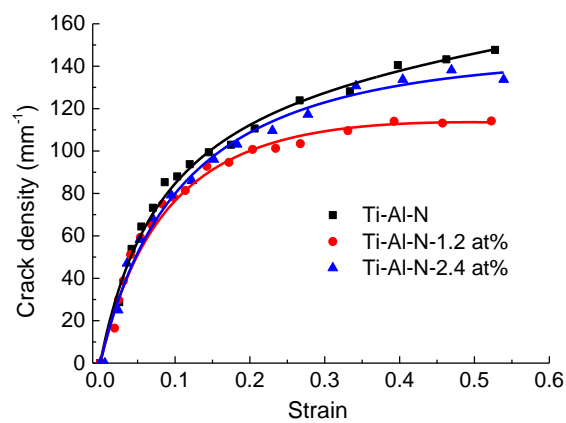


Figure 5.14 Comparison of crack density variation of 5 r.p.m $\text{Ti}_{1-x-y}\text{Al}_x\text{Y}_y\text{N}$ coatings ($y = 0, 0.012$ and 0.024) with the function of strains.

Furthermore, ball-on-disc tribology tests were employed to assess the wear resistance of 5 r.p.m coatings ($\Lambda = 5.5$ nm) of 0 at%, 1.2 at% and 2.4 at% Y. The friction coefficient of the three coatings were comparable (0.7 - 0.8) after a fast transitional period (Figure 5.15 (a)). However, the calculated wear rates differ substantially, such that $\text{Ti}_{1-x}\text{Al}_x\text{N}$ and $\text{Ti}_{0.976-x}\text{Al}_x\text{Y}_{0.024}\text{N}$ are $\sim 6 \times 10^{-15} \text{m}^3/\text{Nm}$ while the $\text{Ti}_{0.988-x}\text{Al}_x\text{Y}_{0.012}\text{N}$ is higher by a factor of 2 to $\sim 13 \times 10^{-15} \text{m}^3/\text{Nm}$.

Compared to $\text{Ti}_{1-x}\text{Al}_x\text{N}$ the lower wear resistance after 1.2 at% Y addition contradicts the improved hardness and H/E value proposed to be an indicator of wear resistance [36]. Therefore, the mechanical properties are not the key factors. Meanwhile, 1.2 at% Y addition significantly increased the compressive stress and decreased adhesion as discussed above, which might be related to the weakened wear resistance. Indeed, according to literature reports wear resistance could be controlled by residual stress, coating compositions or coating adhesion [37, 38]. Frictional heat would rapidly relax the residual stress in highly strained coatings and aggregate crack propagations. On the other hand, Y addition favours enhancing coating tribology behaviour by increasing resistance to frictional tribo-oxidation that commonly occurs in friction at room temperature [39]. Increasing Y content could effectively suppress tribo-oxidation and improve wear resistance by reducing TiO_2 content which has high friction coefficient. Overall, this work suggests adding 1.2 at% Y lead to the poorest wear resistance probably due to the increased compressive resistance, while 2.4 at% Y coating with improved wear behaviour through enhanced oxidation resistance. In summary, $\text{Ti}_{0.988-x}\text{Al}_x\text{Y}_{0.012}\text{N}$ shows degraded adhesion and wear resistance compared to $\text{Ti}_{1-x}\text{Al}_x\text{N}$, while $\text{Ti}_{0.976-x}\text{Al}_x\text{Y}_{0.024}\text{N}$ presents comparable performance to $\text{Ti}_{1-x}\text{Al}_x\text{N}$.

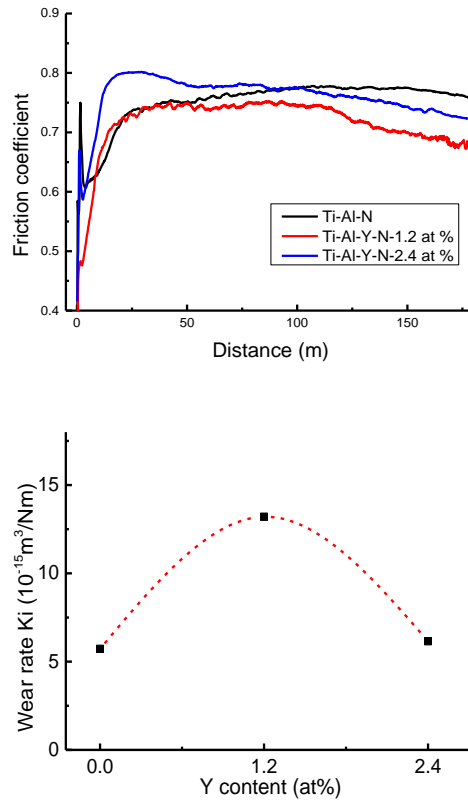


Figure 5.15 Friction coefficient changes versus sliding distance (a) and wear rate comparison (b) of $Ti_{1-x}Al_xN$, $Ti_{0.988-x}Al_xY_{0.012}N$ and $Ti_{0.976-x}Al_xY_{0.024}N$ 5 r.p.m coatings.

5.4.3 Coating oxidation resistance

The coatings on stainless steel substrates including $Ti_{1-x}Al_xN$, $Ti_{0.988-x}Al_xY_{0.012}N$ and $Ti_{0.976-x}Al_xY_{0.024}N$ ($\Lambda = 5.5$ nm) annealed at $800^\circ C$ in air for 10 hours oxidized with a corresponding weight gain (Figure 5.16). $Ti_{1-x}Al_xN$ gained 0.13 mg/cm^2 after annealing, $Ti_{0.988-x}Al_xY_{0.012}N$ gained 0.10 mg/cm^2 and $Ti_{0.976-x}Al_xY_{0.024}N$ gained 0.08 mg/cm^2 , showing an evident benefit of Y addition. Meanwhile, Y incorporation changed the oxide composition in the annealed samples. The retained TiN cubic reflections and the absence of oxidized substrate phases indicate only partial oxidation. The $Ti_{1-x}Al_xN$ coating presents θ -alumina, α -alumina and rutile. The α -alumina is thermodynamically

stable and the θ -alumina is a metastable monoclinic phase that persists after 10-hour treatment at 800°C in air. The $\text{Ti}_{0.988-x}\text{Al}_x\text{Y}_{0.012}\text{N}$ coatings after annealing present similar reflections including θ and α -alumina and rutile. However, the rutile phase is less abundant than in the annealed $\text{Ti}_{1-x}\text{Al}_x\text{N}$. By comparison, the annealed $\text{Ti}_{0.976-x}\text{Al}_x\text{Y}_{0.024}\text{N}$ shows different oxides, such as cubic γ -alumina, Ti_2O_3 and weak reflections of θ -alumina and rutile, with α -alumina below the limit of detection. The phenomenon suggests that 2.4 at% Y getters oxygen and promotes substoichiometric Ti_2O_3 , rather than rutile. Furthermore, 2.4 at% Y effectively retarded the metastable alumina (θ , γ) transformation to α -alumina. Therefore an improved oxidation resistance is obtained.

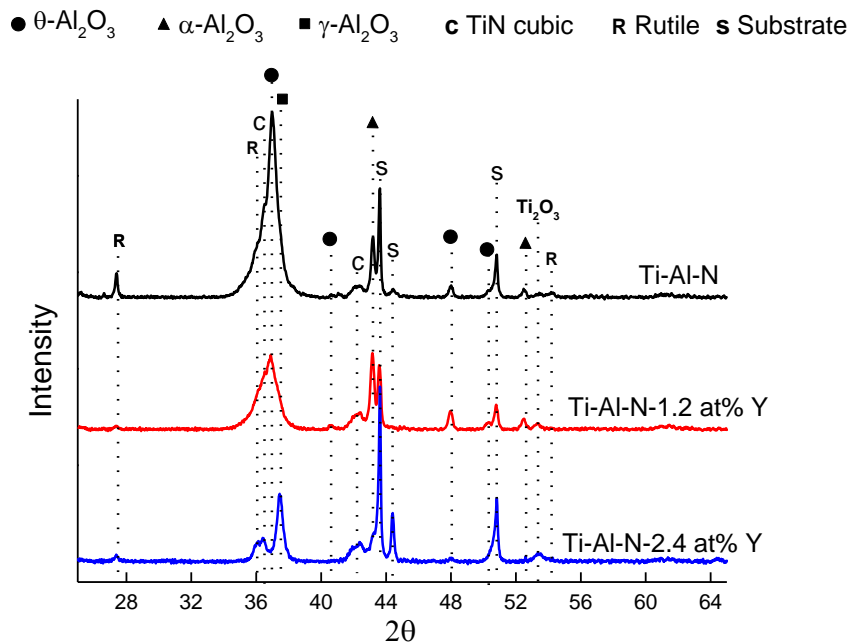


Figure 5.16 XRD patterns of 5 r.p.m $\text{Ti}_{1-x}\text{Al}_x\text{N}$, $\text{Ti}_{0.988-x}\text{Al}_x\text{Y}_{0.012}\text{N}$ and $\text{Ti}_{0.976-x}\text{Al}_x\text{Y}_{0.024}\text{N}$ ($\Lambda = 5.5$ nm) coatings annealed at 800°C in air for 10 hours. The γ and θ -alumina, rutile are identified in annealed $\text{Ti}_{1-x}\text{Al}_x\text{N}$ and $\text{Ti}_{0.988-x}\text{Al}_x\text{Y}_{0.012}\text{N}$ coatings while α -alumina and Ti_2O_3 present in $\text{Ti}_{0.976-x}\text{Al}_x\text{Y}_{0.024}\text{N}$.

The lower oxygen fugacity favouring substoichiometric oxidation of Ti was probably caused by the Y segregation effect. In $\text{Ti}_{1-x}\text{Al}_x\text{N}$ the oxidation is realized through inward oxygen diffusion to the oxide/nitride interface and Al diffusion outward through grain boundaries to the oxide-vapor interface [40].

Furthermore, columnar grains in coatings offer direct pathways between the substrate and vapor-coating interface. However, Y atoms have high surface mobility and affinity to oxygen at elevated temperature and tend to segregate to grain boundaries, forming yttrium oxide that inhibits diffusion [12]. The observation that coatings without Y present mostly θ - and α -alumina, while 2.4 at% Y lead to cubic γ - alumina can be attributed to oxygen vacancy consumption by Y, which is necessary for the transformation of metastable to stable alumina [41, 42]. It has been reported that thermodynamically stable alumina was arranged from unstable alumina at high temperature by annihilating cations and anion vacancies [43], in the stabilization sequence $\gamma \rightarrow \theta \rightarrow \alpha$ -alumina [44]. Thus incorporating excessive Y slows alumina structural rearrangement, which attenuates the entire oxidation process.

5.5 Conclusion

$\text{Ti}_{1-x-y}\text{Al}_x\text{Y}_y\text{N}$ multilayer coatings of varying Λ ($5.5\text{nm} \leq \Lambda \leq 24\text{ nm}$) and composition ($0 \leq y \leq 0.024$) were deposited by the CAD technique with the processing variables being the substrate holder rotation speed and Y target power. All coatings were principally of the rock-salt type fcc structure. The $\text{Ti}_{0.976-x}\text{Al}_x\text{Y}_{0.024}\text{N}$ coating with $\Lambda = 5.5\text{ nm}$ consists of acicular grains growing along a $\langle 111 \rangle$ preferred orientation, but increasing Λ from 5.5 to 24 nm by decreasing substrate rotation speed from 5 r.p.m to 1 r.p.m during deposition weakened this texture. Especially for Λ above 13nm the acicular grains were broken down by Y-rich layers to equiaxed grains highly textured along $\langle 200 \rangle$. Simultaneously, coating hardness and Young's modulus degraded as Λ increased due to the enlarged Y-rich region and strengthened Y disruption on grain growth which could cause semicoherent or incoherent grain boundaries and layer interfaces.

For the $Ti_{1-x}Al_xN$ coatings deposited at 5 r.p.m ($\Lambda = 5.5$ nm), the microstructure consists of $\langle 111 \rangle$ textured columnar grains 100 – 200 nm in diameter while in $Ti_{0.976-x}Al_xY_{0.024}N$ smaller crossed acicular grains appear, caused by the secondary hexagonal wurtzite that grows on the rock-salt lattice epitaxially. The incorporated Y changed coating properties. First, increasing Y from 0 to 1.2 at% increased the compressive stress and at a content of 2.4 at% the compressive stress relaxed slightly. Hardness was enhanced with higher Y content. The changes on compressive stress and hardness are a cooperative effect of the solid solution mechanism and re-nucleation effect resulting from Y addition. Meanwhile, coatings of 2.4 at% Y present comparable adhesion and wear resistance as $Ti_{1-x}Al_xN$ even though 1.2 at% Y coatings were inferior in the tensile and tribology tests. Finally, the oxidation resistance of the coatings with different Y content was examined by annealing samples at elevated temperature in air. It was found coatings with higher Y have better resistance to oxidation as Y could induce Ti_2O_3 formation, rather than TiO_2 , due to the blocking of oxygen diffusion pathways within crystals and along grain boundaries. Yttrium also affected alumina polymorph transformation. In summary, $Ti_{0.976-x}Al_xY_{0.024}N$ has enhanced hardness and oxidation resistance with no detriment to substrate adherence and wear resistance.

References:

- [1] A. Hörling, L. Hultman, M. Odén, J. Sjöln and L. Karlsson, *Surf. Coat. Technol.*, **2005**, 191, 384-392.
- [2] T. Leyendecker, O. Lemmer, S. Esser and J. Ebberink, *Surf. Coat. Technol.*, **1991**, 48, 175-178.
- [3] W. Kalss, A. Reiter, V. Derflinger, C. Gey and J. L. Endrino, *Int. J. Refract. Met. Hard Mater.*, **2006**, 24, 399-404.
- [4] S.-Y. Yoon, J.-K. Kim and K. H. Kim, *Surf. Coat. Technol.*, **2002**, 161, 237-242.

- [5] J. H. Hsieh, C. Liang, C. H. Yu and W. Wu, *Surf. Coat. Technol.*, **1998**, 108–109, 132-137.
- [6] F. R. Weber, F. Fontaine, M. Scheib and W. Bock, *Surf. Coat. Technol.*, **2004**, 177–178, 227-232.
- [7] Y. H. Cheng, T. Browne, B. Heckerman and E. I. Meletis, *Surf. Coat. Technol.*, **2010**, 204, 2123-2129.
- [8] S. K. Kim, P. V. Vinh, J. H. Kim and T. Ngoc, *Surf. Coat. Technol.*, **2005**, 200, 1391-1394.
- [9] Q. Ru, S. Hu, N. Huang, L. Zhao, X. Qiu and X. Hu, *Rare Metals*, **2008**, 27, 251-256.
- [10] W.-D. Münz, *MRS Bull.*, **2003**, 28, 173-179.
- [11] M. Pfeiler-Deutschmann, P. H. Mayrhofer, K. Chladil, M. Penoy, C. Michotte, M. Kathrein and C. Mitterer, *Thin Solid Films*, **2015**, 581, 20-24.
- [12] B. A. Pint, *Oxid. Met.*, **1996**, 45, 1-37.
- [13] L. Zhu, Y. Zhang, W. Ni and Y. Liu, *Surf. Coat. Technol.*, **2013**, 214, 53-58.
- [14] H. Riedl, D. Holec, R. Rachbauer, P. Polcik, R. Hollerweger, J. Paulitsch and P. H. Mayrhofer, *Surf. Coat. Technol.*, **2013**, 235, 174-180.
- [15] L. Székely, G. Sáfrán, V. Kis, Z. E. Horváth, P. H. Mayrhofer, M. Moser, G. Radnóczy, F. Misják and P. B. Barna, *Surf. Coat. Technol.*, **2014**, 257, 3-14.
- [16] C. Ducros, C. Cayron and F. Sanchette, *Surf. Coat. Technol.*, **2006**, 201, 136-142.
- [17] W. C. Oliver and G. M. Pharr, *J. Mater. Res.*, **1992**, 7, 1564-1583.
- [18] H. Bückle, *Metallurgical Reviews*, **1959**, 4, 49-100.
- [19] F. Toscan, L. Antoni, Y. Wouters, M. Dupeux and A. Galerie, 2004.
- [20] J. Pelleg, L. Z. Zevin, S. Lungo and N. Croitoru, *Thin Solid Films*, **1991**, 197, 117-128.
- [21] F. Bannister, *Mineralogical Magazine*, **1941**, 26, 36-44.

- [22] H. Schulz and K. H. Thiemann, *Solid State Commun.*, **1977**, 23, 815-819.
- [23] L. Chen, J. Paulitsch, Y. Du and P. H. Mayrhofer, *Surf. Coat. Technol.*, **2012**, 206, 2954-2960.
- [24] Y. Pinot, M. H. Tuilier, M. J. Pac, C. Rousselot and D. Thiaudiere, *Journal of Synchrotron Radiation*, **2015**, 22, 1440-1449.
- [25] P. Mayrhofer, D. Music and J. Schneider, *J. Appl. Phys.*, **2006**, 100, 094906.
- [26] I. A. Abrikosov, A. Knutsson, B. Alling, F. Tasnádi, H. Lind, L. Hultman and M. Odén, *Materials*, **2011**, 4, 1599.
- [27] P. Mayrhofer, D. Music and J. Schneider, *J. Appl. Phys.*, **2006**, 100, 1-094906.
- [28] R. Rachbauer, A. Blutmager, D. Holec and P. H. Mayrhofer, *Surf. Coat. Technol.*, **2012**, 206, 2667-2672.
- [29] M. Moser and P. H. Mayrhofer, *Scripta Mater.*, **2007**, 57, 357-360.
- [30] Z. T. Wu, Z. B. Qi, F. P. Zhu, B. Liu and Z. C. Wang, *Physics Procedia*, **2013**, 50, 150-155.
- [31] C. Mitterer, P. H. Mayrhofer and J. Musil, *Vacuum*, **2003**, 71, 279-284.
- [32] X. S. Wan, S. S. Zhao, Y. Yang, J. Gong and C. Sun, *Surf. Coat. Technol.*, **2010**, 204, 1800-1810.
- [33] F. Rovere and P. H. Mayrhofer, *J. Vac. Sci. Technol., A*, **2007**, 25, 1336-1340.
- [34] H.-M. Tung, J.-H. Huang, D.-G. Tsai, C.-F. Ai and G.-P. Yu, *Materials Science and Engineering: A*, **2009**, 500, 104-108.
- [35] D. C. Agrawal and R. Raj, *Acta Metall.*, **1989**, 37, 1265-1270.
- [36] A. Leyland and A. Matthews, *Wear*, **2000**, 246, 1-11.
- [37] V. Belous, V. Vasyliiev, A. Luchaninov, V. Marinin, E. Reshetnyak, V. Strel'nitskij, S. Goltvyanytsya and V. Goltvyanytsya, *Surf. Coat. Technol.*, **2013**, 223, 68-74.

- [38] M. Pfeiler, K. Kutschej, M. Penoy, C. Michotte, C. Mitterer and M. Kathrein, *Surf. Coat. Technol.*, **2007**, 202, 1050-1054.
- [39] H. Ju and J. Xu, *Surf. Coat. Technol.*, **2015**, 283, 311-317.
- [40] D. McIntyre, J. E. Greene, G. Håkansson, J. E. Sundgren and W. D. Münz, *J. Appl. Phys.*, **1990**, 67, 1542-1553.
- [41] J. Jedliński, *Oxid. Met.*, **1993**, 39, 55-60.
- [42] F. Rovere, P. Mayrhofer, A. Reinholdt, J. Mayer and J. Schneider, *Surf. Coat. Technol.*, **2008**, 202, 5870-5875.
- [43] P. Burtin, J. P. Brunelle, M. Pijolat and M. Soustelle, *Applied Catalysis*, **1987**, 34, 239-254.
- [44] I. Levin and D. Brandon, *J. Am. Ceram. Soc.*, **1998**, 81, 1995-2012.

Chapter 6

The deposition, structure and properties of nanocomposite TiSiN coatings*

TiSiN nanocomposite coatings were deposited using high power impulse magnetron sputtering (HiPIMS) impacting a Ti target together with DC-pulsed magnetron sputtering on a Si target. The Si content was varied by controlling the Si target current to fabricate coatings with Si / (Si + Ti) atomic percentages ranging from 0.59 – 19.72 at%. X-ray diffraction and transmission electron microscopy were used to characterize coating microstructure as a function of Si incorporation. In general, smaller crystal size was promoted by higher Si concentrations leading to TiN / amorphous (a)-Si₃N₄ nanocomposites. Because the microstructure is modified as a function of Si incorporation, this parameter can be an agent for tailoring mechanical properties, wear resistance and passivating oxidation. Coating performance was validated using nanoindentation and ball-on-disc testing before and after thermal annealing. In this manner, it was shown that Ti_{0.903}Si_{0.097}N was harder than TiN and demonstrated superior resistance to wear and oxidation.

* This Chapter is substantially published as M. Arab Pour Yazdi, F. Lomello, J. Wang, F. Sanchette, Z. Dong, T. White, Y. Wouters, F. Schuster, A. Billard. Properties of TiSiN coatings deposited by hybrid HiPIMS and pulsed-DC magnetron co-sputtering, Vacuum 109 (2014) 43-51.

6.1 Introduction

Nanocomposites containing crystallites smaller than 10 nm connected by amorphous phase grain boundaries show enhanced hardness because sources of dislocation multiplication inside crystallites are removed [1]. One advantage of nanocrystalline/amorphous coatings over nanolayered coatings is that isotropic systems are nearer thermodynamic equilibrium, compared to misfit lattice strained architectures that are highly anisotropic [2]. This leads to the improved wear resistance required for tribological coatings. In practice, the fabrication of nanocomposite films should combine a high rate of nucleation with slow crystal growth. Magnetron sputtering (MS) with low-energy ion bombardment is suitable for nanocomposite films preparation [3-6]. Besides controlling ion bombardment energy, adding elements to promote the amorphous phase segregating to grain boundaries is another way to generate the nanocomposite structure. The large miscibility gap between crystalline TiN and Si₃N₄ predisposes the formation of a binary nanocomposite [7]. Moreover, TiN and amorphous (a-) Si₃N₄ both have a high elastic modulus (calculated Young's modulus of a-Si₃N₄ is 290 GPa [8], TiN was reported in the range of 400 – 650 GPa [9-11]) which promotes enhanced hardness. Additionally, Si₃N₄ could improve the thermal stability and oxidation resistance of crystalline TiN films by blocking oxygen diffusion along grain boundaries [12]. Hence, by controlling the silicon content and physical vapor deposition (PVD) parameters nanocrystallite size and orientation can be designed to enhance mechanical properties and thermal stability.

During reactive magnetron sputtering phase segregation in the TiN/amorphous (a-)Si₃N₄ nanocomposite thin films is promoted by high nitrogen pressures (≥ 0.1 Pa) and deposition temperatures (550 – 650°C) at low deposition rates (~1.8 nm/s) [1]. Conventional low temperature PVD with non-equilibrium ion bombardment cannot assure phase segregation, but will produce a metastable

solid solution phase [13], and generate columnar morphology with large grain size and rough coating surfaces. High power impulse magnetron sputtering (HiPIMS), as a unique low temperature deposition process, could realize the nanocomposites as its low-energy high-flux ion irradiation is advantageous for renucleation, leading to a smooth surface and dense film. The high peak power density in HiPIMS produced by increasing peak current can sputter and ionize large numbers of target atoms and enhance renucleation to suppress columnar grains and promote the formation of featureless nanocrystallites [14]. Therefore, HiPIMS favours phase segregation during TiN/Si₃N₄ nanocomposite deposition [15].

This chapter describes how the TiN/Si₃N₄ nanocomposite structure is modified by adjusting the Si/(Ti+Si) atomic ratio during fabrication using a hybrid technique of HiPIMS and direct current (DC) magnetron sputtering. HiPIMS was used on the Ti target to obtain dense ionization and promote interface adhesion of the thin film to substrate, while DC magnetron sputtering on a Si target controlled composition. The microstructures and microchemistry of the coatings were correlated with mechanical, tribological properties and oxidation resistance.

6.2 Experimental methods

6.2.1 Sample deposition

The deposition was performed in a Balzers 640 R unit equipped with 128 × 254 mm² Ti and Si targets of 99.9% purity mounted on a rotating substrate holder (Figure 6.1). The Ti target was powered by HiPIMS (Hutterer 4002) while Si was powered by pulsed-DC magnetron sputtering (Pinnacle Plus). The bias applied to the substrate holder was – 50 V and its rotation speed was 20 r.p.m. The deposition temperature was < 200°C and the deposition duration 180 min.

The Ar flow was 200 sccm and N₂ flow was 5 sccm. On the Ti target the HiPIMS peak voltage was - 700 V and pulse-on-time was 28 μ s. The frequency was 500 Hz and the average target current \sim 2 A. For the Si target the current varied from 0 to 0.9 A, with a frequency of 50 kHz and power-off time of 5 μ s. The drawing distance from the Ti and Si targets were 50 mm and 140 mm respectively. In this manner, materials of fixed Ti concentration, but variable Si contents, were obtained. The substrates were M2 HSS cylinders 30 mm in diameter, that were polished to a mirror finish. The detailed processing parameters are collected in Table 6.1.

6.2.2 Sample characterization

Cross section fracture surfaces were observed with a field emission scanning electron microscope (FESEM) by secondary electron imaging (SEI) (JEOL JSM-7800F) and the microstructure examined by a transmission electron microscope (TEM) (JEOL 2100F) operated at 200 kV. Energy dispersive X-ray spectroscopy (EDX) coupled with FESEM was used to determine Si content and distribution. X-ray diffraction (XRD) ($\lambda_{\text{Co}} = 0.1788970$ nm) in $\theta - 2\theta$ mode was employed for phase analysis of the as-deposited and annealed samples using a Bruker D8 device. Pawley fitting [16] and the Debye-Scherrer method [17] were used to derive lattice parameters and crystal size respectively.

Nanoindentation with a Berkovich diamond tip (NHT CSM) was used to measure and calculate hardness and Young's modulus by the Oliver and Pharr method [18] with results averaged over 40 replicates and with the depth $<$ 10% of the coating thickness to avoid substrate artefacts. The coating wear resistance was evaluated by ball-on-disc tests (CSM tribometer) performed at 19-22°C and a relative humidity of 33 - 39 %. The counter ball material was WC/Co with a constant 10 N load on the ball, and the wear track on sample surface was 6 mm diameter. The sliding speed was 100 mm/s and the entire sliding distance

was 600 m. The tribology scars were examined by a profilometer with height resolution of 10 nm. The sample was annealed in air at 700°C for 2 hours with a heating rate of 2°C / min and the cooling rate of 3°C / min.

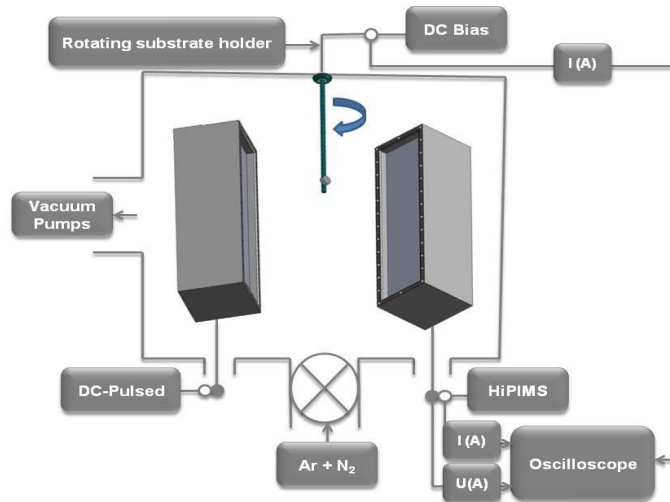


Figure 6.1 Schematic of the hybrid of DC-pulsed magnetron sputtering and HiPIMS deposition system

Table 6.1 TiN/Si₃N₄ nanocomposite coating deposition parameters

	Target parameters		Chamber Parameters	
	Titanium Target	Silicon target		
Generator	HiPIMS Hüttinger 4002	Pulsed-DC MS Pinnacle Plus, Advanced Energy	Total Pressure	~0.5 Pa
Maximum power	Peak Voltage: - 700 V Peak current: ~ 142 A	< 200 W	Ar flow	200 sccm
Average Target Current	≤ 2A	0→0.9 A	N ₂ flow	5 sccm
Pulse time T _{on}	0.14 μs	15 μs	Deposition time	180 min
Frequency	500 Hz	50 kHz	Deposition temperature	< 200 °C
Distance to substrate	50 mm	140 mm	Rotation speed	≈ 20 r.p.m.
			Bias voltage	- 50 V

6.3 Composition and structure analysis

Si content was confirmed by EDX analysis and increased linearly with power supplied to the Si target (0 to 0.9 A) while the power supply on Ti target was fixed, such that the cation ratio ranged from 0 to 20 at%.

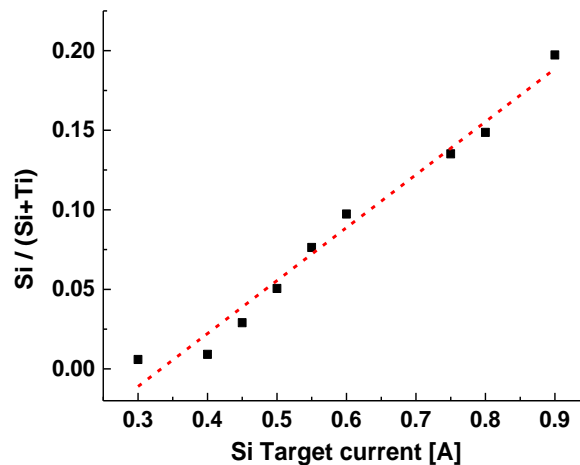


Figure 6.2 The Si to (Si+Ti) cation ratio versus the current applied on Si target

6.3.1 Coating texture and crystal size

XRD shows that from TiN to $(\text{Ti}_{0.8028}, \text{Si}_{0.1972})\text{N}$ the structure evolves progressively (Figure 6.3), especially the coating texture (Figure 6.4). Rock-salt fcc TiN shows preferential $\langle 111 \rangle$ crystal growth perpendicular to the substrate surface. A Le Bail fit yielded the lattice parameter $a = 4.296(3) \text{ \AA}$. As Si content was raised from 0 to 2.89 at% the coating preserved the $\langle 111 \rangle$ texture (texture coefficient $T^*_{\langle 111 \rangle} \sim 98\%$), however, beyond 2.89 at% the $\langle 111 \rangle$ coefficient decreased significantly, while $\langle 200 \rangle$ became the predominant orientation, e.g. in $\text{Ti}_{0.9404}\text{Si}_{0.0506}\text{N}$ and $\text{Ti}_{0.9236}\text{Si}_{0.0764}\text{N}$, $T^*_{\langle 111 \rangle} / T^*_{\langle 200 \rangle} = 14/86$. (The coating with 2.89 at% Si shows additional unidentified reflections thus the pattern was not amenable to texture and crystal size analysis). The texture transformation from $\langle 111 \rangle$ to $\langle 200 \rangle$ is driven by the changing dominance of

strain energy to surface energy. As more Si was added into the coating, the grain growth was interrupted and renucleation occurred with TiN and Si₃N₄ segregating. Smaller crystals formed where surface energy minimization is dominant for crystal growth, rather than strain energy. Hence, grains tend to grow along the close-packed planes {200} planes of rock-salt TiN [19]. The texture transformation was also consistent with a smaller crystal size. As Si increased to 9.72 at% the (200) peak broadened due to reduced coherent crystal domains, and grains were less textured ($T^*_{\langle 111 \rangle} / T^*_{\langle 200 \rangle} = 26/74$). Adding ≥ 13.51 at% Si removes the $\langle 200 \rangle$ and $\langle 111 \rangle$ reflections, indicating the formation of an X-ray amorphous phase.

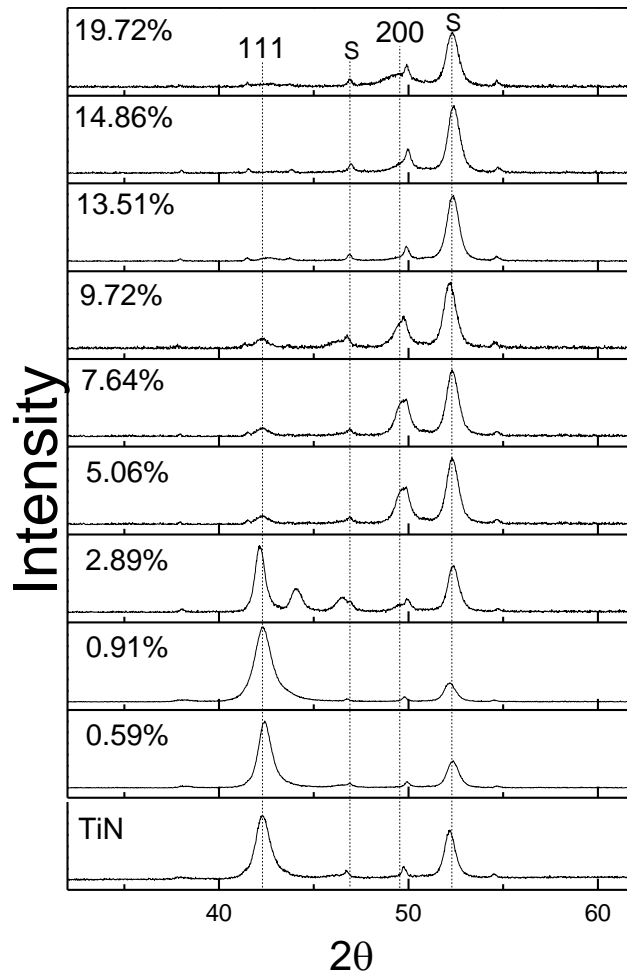


Figure 6.3 XRD patterns of Ti_{1-x}Si_xN coatings containing Si content from 0 to 19.72 at%

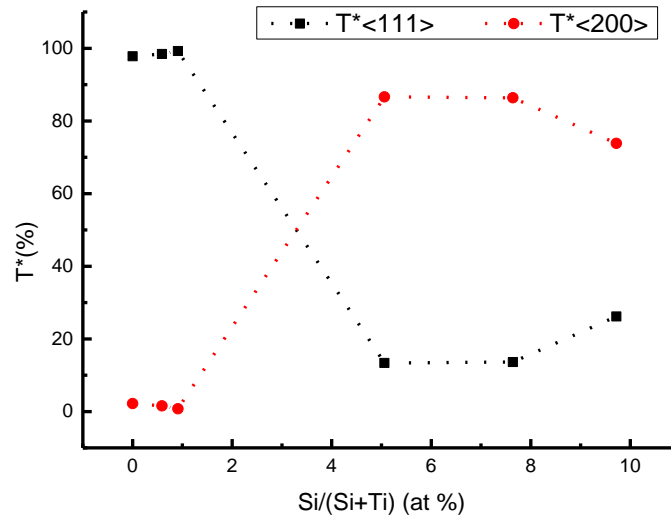


Figure 6.4 The T^* percentage of $\langle 111 \rangle$ and $\langle 200 \rangle$ texture versus Si content; Coatings with Si content ≥ 13.51 at% which are not included as no obvious reflections were observed.

Crystal sizes fitted according to the Debye-Scherrer method [17] as implemented in using Topas V3 varied with Si content (Figure 6.5). The $\text{Ti}_{0.9941}\text{Si}_{0.0059}\text{N}$ coating has a crystal size of $45 \text{ nm} \pm 3 \text{ nm}$. As Si content increased, the crystal size development proceeded through three stages. In the first stage with $0 \leq \text{Si} \leq 3$ at% the crystal size diminished with the texture transferring from $\langle 111 \rangle$ to $\langle 200 \rangle$. Due to the immiscibility of TiN and Si_3N_4 [20], additional Si facilitates phase segregation through spinodal decomposition (see in section 2.3.2, Chapter 2) [21]. Si_3N_4 promoted the break down of larger TiN grains to crystallites $\sim 15 \text{ nm}$ in extent, with preferential growth on $\{200\}$ to minimize surface energy. Elsewhere, it was reported that a TiSiN solid solution exists at low Si content [22]. According to Veprek [20] the metastable TiSiN solid solution was caused by impurities, especially oxygen, which would hinder phase segregation by strongly bonding with Si_xN to form clusters with low diffusivity. A solid solution would detract from mechanical properties and thermal stability, but further validation is required. For the second stage with $3 \leq \text{Si} \leq 10$ at%, the $\langle 200 \rangle$ texture weakened, and crystal size diminished and

stabilized around 10 nm. For these compositions the Si_3N_4 tended to encapsulate entire randomly oriented TiN crystallites [23, 24]. Finally, for $\text{Si} > 10$ at% the crystal size was < 10 nm, separated by a larger volume of X-ray amorphous Si_3N_4 with only substrate reflections appearing in XRD patterns. It gives a visual comparison among samples of 1, 10 and 20 at% by HRTEM in Figure 6.7 (b)-(d).

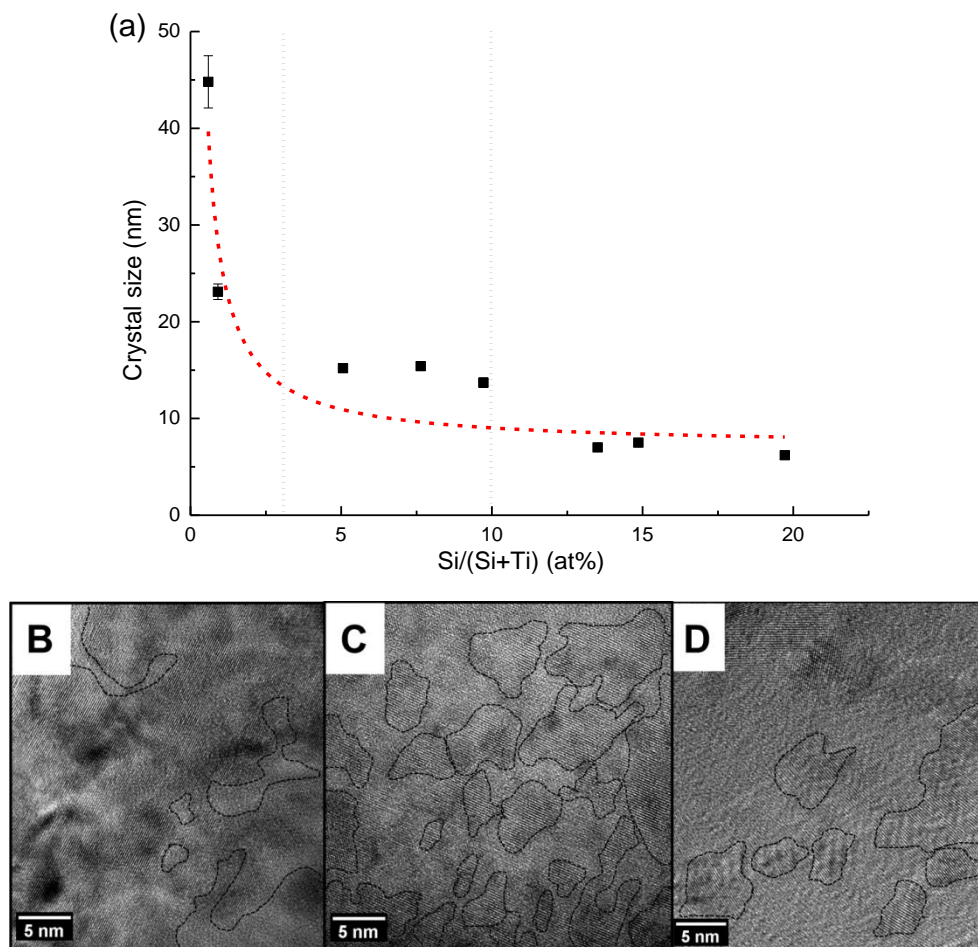


Figure 6.5 (a) $\text{Ti}_{1-x}\text{Si}_x\text{N}$ coatings crystal size calculated from XRD patterns versus Si content; And HR-TEM micrographs of the $\text{Ti}_{1-x}\text{Si}_x\text{N}$ sample cross-sections with $x =$ (b) 1, (c) 10 & (d) 20 at. %.

6.3.2 Microstructure and morphology

The cross sections of TiN and $\text{Ti}_{0.903}\text{Si}_{0.097}\text{N}$ directly deposited on the substrate at a rate of $\sim 0.76 \mu\text{m} / \text{h}$ to a total thickness of $\sim 2.3 \mu\text{m}$ present a dense and

smooth morphology (Figure 6.6). The microstructure is typical of HiPIMS processing that favors renucleation and suppression of columnar grains.

Moreover, $\text{Ti}_{0.994}\text{Si}_{0.006}\text{N}$ and $\text{Ti}_{0.903}\text{Si}_{0.097}\text{N}$ thinned by focused ion beam (FIB) milling reveal that the coating with 0.6 at% Si consists of grains connected by high angle boundaries crossing the entire coating thickness with strong $\langle 111 \rangle$ texture (Figure 6.7). By comparison, crystals in 9.7% Si coatings were much smaller. Meanwhile, the SAED of $\text{Ti}_{0.903}\text{Si}_{0.097}\text{N}$ contains a near continuous diffraction ring instead of the discrete reflections of $\text{Ti}_{0.994}\text{Si}_{0.006}\text{N}$. This suggests that Si destroys long range crystal order and accentuates grain boundaries. Some texture is apparent which is at variance with modelling [23] that predicts fully segregated phases with randomly distributed crystallites.

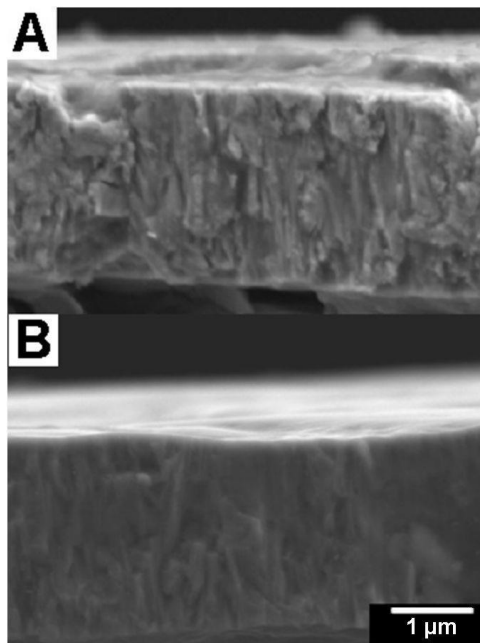


Figure 6.6 SEM Cross sections of (a) TiN and (b) $\text{Ti}_{0.903}\text{Si}_{0.097}\text{N}$

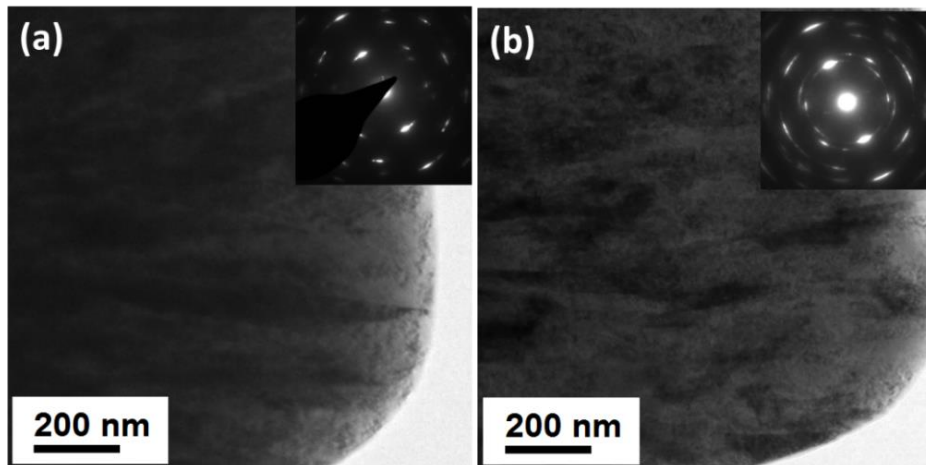


Figure 6.7 TEM Cross sections of (a) $\text{Ti}_{0.994}\text{Si}_{0.006}\text{N}$ and (b) $\text{Ti}_{0.903}\text{Si}_{0.097}\text{N}$ with SAED insets

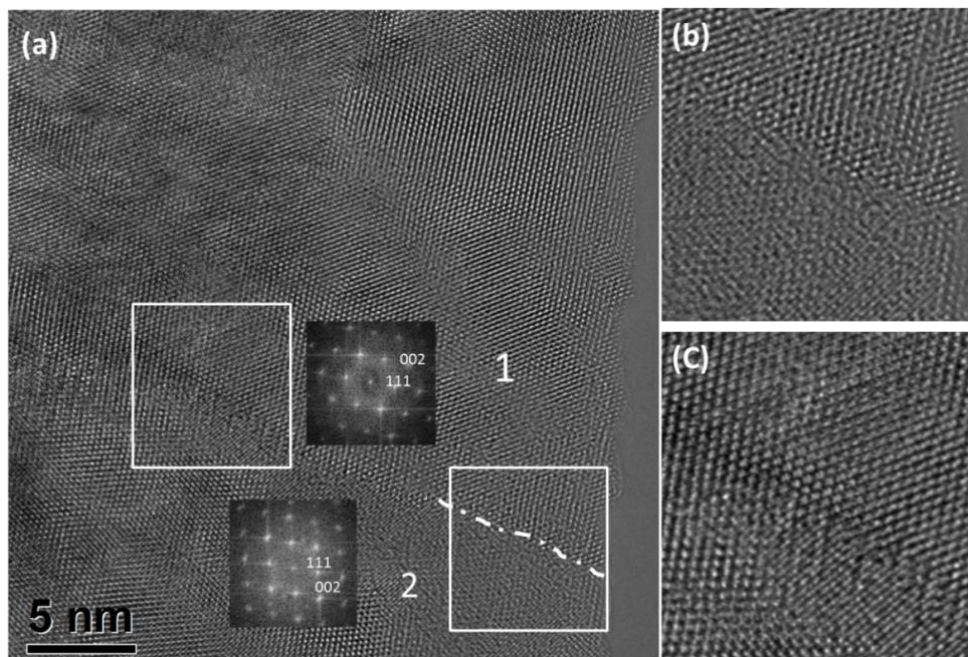


Figure 6.8 The HRTEM image in $[1-10]$ zone axis showing boundary of $\text{Ti}_{0.903}\text{Si}_{0.097}\text{N}$ between a pair of twin grains. The insets are belonging to grain 1 and grain 2 respectively. The squared area on right is enlarged in (b) showing an intergranular region while the squared area on left enlarged in (c) does not show such region.

Crystals of $\text{Ti}_{0.903}\text{Si}_{0.097}\text{N}$ are often twinned on (111) (Figure 6.8). The intergranular region is probably occupied by X-ray amorphous Si_3N_4 , as

reported theoretically and experimentally [25, 26]. According to Vepřek and Reiprich [2], the high hardness (> 50 GPa) arises from a nanocomposite architecture where TiN nanocrystals terminated at (hkl) interfaces and are attached to co-incident interfaces ($h'k'l'$) of other TiN nanocrystals through a strong and sharp Si_3N_4 monolayer coherently. The presence of twin crystals implies grain growth was interrupted by silicon but the intergranular region does not fully encapsulate the TiN crystallites (Figure 6.8 (c)). In $\text{Ti}_{0.903}\text{Si}_{0.097}\text{N}$, the Si_3N_4 did not disrupt the TiN crystals to a randomly orientated collection of nanocrystallites, as residual $\langle 200 \rangle$ texture was evident in XRD (Figure 6.7).

6.4 Ti-Si-N properties

6.4.1 Hardness and Young's modulus

The hardness of TiN is 22 ± 4 GPa and with the addition of 2.89 at% Si significantly improves the hardness to 36 ± 2 GPa while Young's modulus increases from 340 ± 60 GPa to 476 ± 38 GPa (Figure 6.9). At lower concentrations, Si probably substitutes directly for Ti to form a solid solution that creates chemical point defects that disrupt dislocation movement. In addition, the large immiscibility between TiN and Si_3N_4 also promotes a systematic reduction in crystal size that contributes to hardness enhancement. At ~ 10 at% Si, the crystal size stabilized around 10 nm (Figure 6.4), and a maximum hardness of 41 ± 3 GPa is attained. Beyond this level, Si decreases hardness, possibly as a consequence of wide disordered Si_3N_4 layers that weaken grain boundaries.

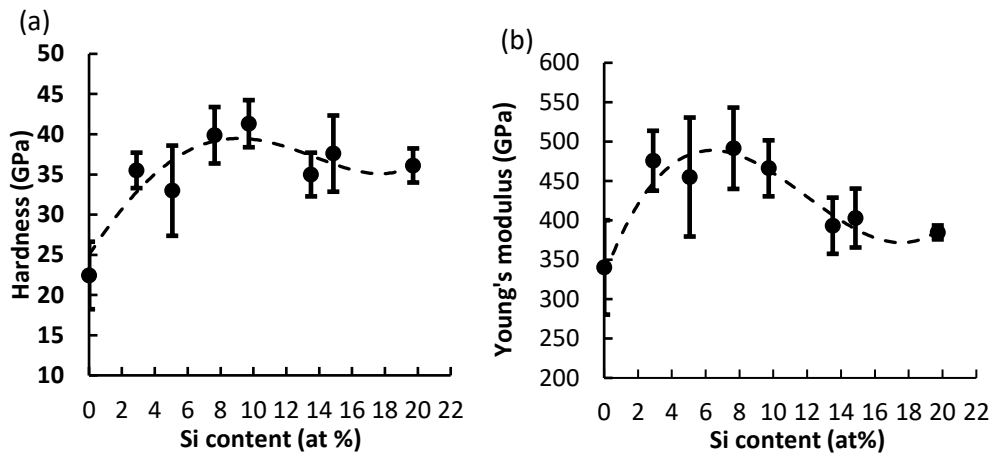


Figure 6.9 (a) Coating hardness versus Si content; (b) Young's modulus versus Si content

Nanocomposite TiN/ Si_3N_4 has been widely studied in recent decades to understand its hardening mechanism. Smaller crystals improve mechanical properties by limiting dislocation generation and increasing the prevalence of grain boundaries that introduce dislocation pile-up and stress fields. However, should the crystals reduce below a critical value, local sliding at grain and phase boundaries will promote mechanical failure [27, 28]. The nanosize effect could double the hardness at a crystal size to ~ 10 nm [29]. In Ti-Si-N the large immiscibility between TiN and Si_3N_4 favours nanosized structures and moreover, a proposed model of 3-4 nm random orientated crystallites separated by 1 monolayer thick (0.3-0.4 nm) Si_3N_4 could improve the hardness further by a factor of 4 – 5 (Figure 6.10) [30]. In this content, it is noted that Si_3N_4 is not conventionally amorphous with atomic disorder, but refers to an X-ray amorphous phase of 1 – 2 monolayer thickness. Dislocations will not appear in 3 – 4 nm crystals thus the weak link in nanocomposite Ti-Si-N will be the TiN/ Si_3N_4 interfaces. Based on the calculations of Hao et al. [26], a single monolayer of Si_3N_4 is strongest as the valence charge force is transferred from TiN resulting in hard boundaries [31], while thicker grain boundaries ($> 1.3\text{nm}$) would degrade mechanical properties and thermal stability. In this study, the hybrid of PVD HiPIMS and DC magnetron sputtering techniques were used to

deposit self-organized nano-scale Ti-Si-N composites. Consistent with Bendavid et al. [24], the hardness was enhanced by adding 10 at% Si and deteriorated beyond that content. However, the partially $\langle 200 \rangle$ textured $\text{Ti}_{0.903}\text{Si}_{0.097}\text{N}$ coating suggested that the crystallites were incompletely encapsulated by Si_3N_4 , explaining the relatively low hardness (41 ± 3 GPa) compared to the CVD Ti-Si-N with hardness > 50 GPa [32]. Therefore, further examination of the microstructure including the distribution of Si and texture is required. Veprek [20] suggests that oxygen impurities can bond with intergranular SiN_x to form $-\text{Si-N}_x\text{O}-$ clusters, which not only weaken the nearby Ti-N bonds leading to a soft interfaces, but hinder phase segregation to form the nanocomposite structure with their low diffusivity. Currently, it is impossible to offer insight into the presence or absence of oxygen due to the inadequate lower limit detection of EDX. Further chemical analysis using wavelength dispersive X-ray microanalysis or solid state nuclear magnetic resonance (NMR) spectroscopy could be informative in this regard.

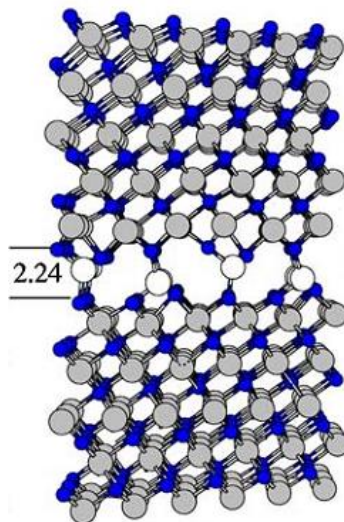


Figure 6.10 The strong one-monolayer Si_3N_4 interface between two TiN (111) slabs. The small blue circle is N atom, the white circle is Si and the large grey circle is Ti.*

*Reprinted figure with permission from [27] as follows: S. Hao, B. Delley and C. Stampfl, *Physical Review B*, **2006**, 74, 035402. Copyright (2016) by the American Physical Society.

6.4.2 Tribology

Tribology behaviour is largely controlled by the counter material and environment. Here ball-on-disk tests compared the wear resistance of the TiN and $\text{Ti}_{0.903}\text{Si}_{0.097}\text{N}$ coatings to yield friction coefficients from 0.5 to 0.8 (Figure 6.11 (a)). Coatings with Si shows slightly lower values ascribed to self-lubricating layers of SiO_2 or $\text{Si}(\text{OH})_2$ as reported previously [33]. The friction coefficient stabilized during testing but debris accumulation caused fluctuations for sliding distances > 500 m. Nonetheless, Si clearly decreases the wear rate in $\text{Ti}_{0.903}\text{Si}_{0.097}\text{N}$ relative to TiN (Figure 6.11(b)). This enhanced performance is because lubricant SiO_2 avoids tribo-oxidation while TiO_2 generated in the TiN coating causes embrittlement and cracking. Moreover, Leyland and Matthews [34] found wear resistance is not only related to H, but also toughness. $\text{Ti}_{0.903}\text{Si}_{0.097}\text{N}$ has better toughness with H/E of 0.088 ± 0.0001 , higher than TiN with H/E 0.065 ± 0.0014 . It is also reported that the improved toughness is attributable to the dense featureless microstructure with coherent TiN/ Si_3N_4 interfaces under force [12].

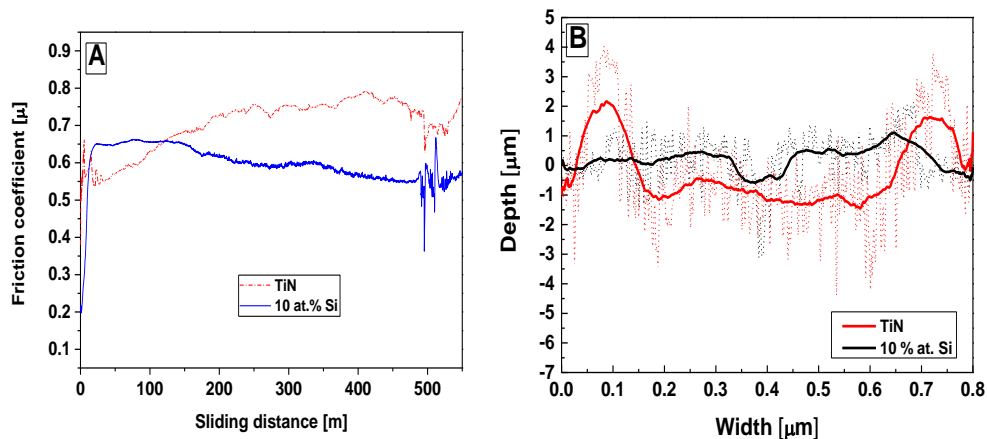


Figure 6.11 (a) Recorded friction coefficient against sliding distance of TiN and $\text{Ti}_{0.903}\text{Si}_{0.097}\text{N}$; and (b) their scar profiles

6.4.3 Oxidation resistance

The oxidation resistance of Ti-Si-N coatings was examined by XRD after soaking at 700°C for 2 hours in air. These conditions generate TiO₂ rutile in TiN but oxidation is passivated when Si addition exceeds 10 at% (Figure 6.12). Moreover, the coating hardness deteriorated after annealing due to the presence of less hard titania (Figure 6.13), and possibly crystal growth. Si addition improves annealed coating hardness, suggesting higher Si content in Ti-Si-N can preserve the hardness and enhance thermal stability.

Si-free TiN coatings decomposed and released nitrogen, especially along grain boundaries, as these were vulnerable to oxidation, and provide diffusion pathways for inward migration of oxygen and outward percolation of cations. Columnar TiN shows the poorest oxidation resistance because the grain boundaries provide direct routes from surface to substrate migration which weakens coating adherence [12]. However, when α -Si₃N₄ is dispersed among TiN crystallite it acts as barrier to oxygen diffusion. It is possible that annealing oxidizes Si₃N₄ to create a thin silica passivation shell around crystallites [35].

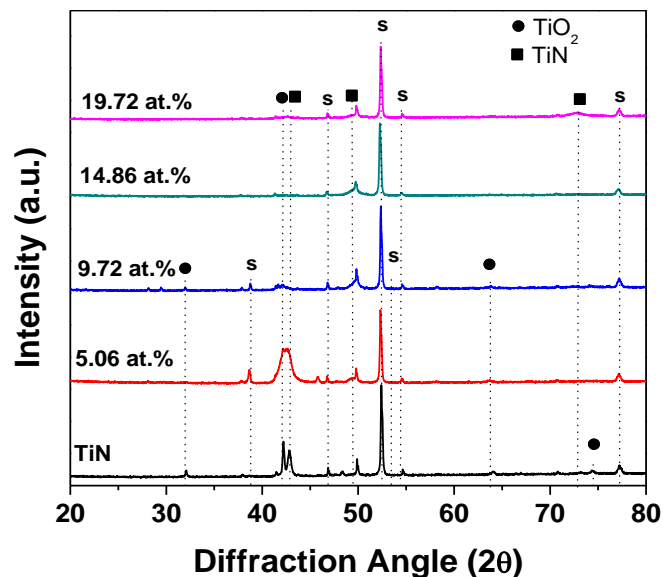


Figure 6.12 XRD of annealed samples of varied Si content (Annealing condition: 700°C for 2 h in air)

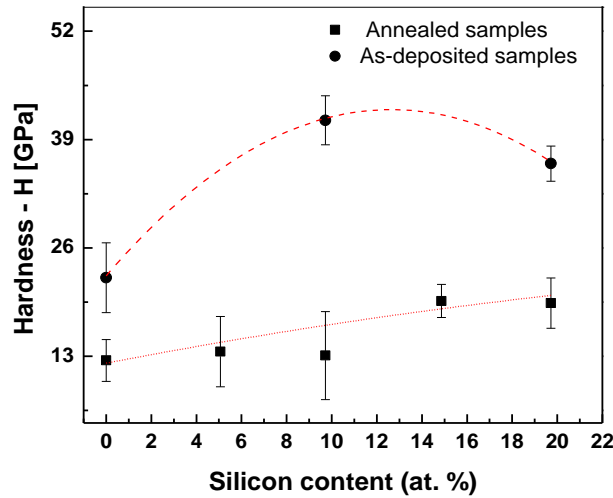


Figure 6.13 Coating hardness versus Si content before and after annealing

6.5 Conclusion

In this chapter, Ti-Si-N coatings with variable Si content were deposited by a combination of HiPIMS (Ti target) and DC-pulsed magnetron sputtering (Si target). HiPIMS ensured the fabrication of droplet-free, dense and smooth coatings, where the composition was well-controlled and the Si to (Si + Ti) ratio varied linearly with the applied current on the Si target.

Tailoring Si content was used to control the Ti-Si-N nanocomposite microstructure, that in turn determined mechanical and oxidation resistance. At higher Si content, the coating texture evolved from $\langle 111 \rangle$ ($0 < \text{Si} < 3$ at%) to $\langle 200 \rangle$ ($3 < \text{Si} < 10$ at%) and finally removes preferred orientation ($\text{Si} > 10$ at%). The crystal size diminished with increasing Si content, consistent with the removal of texture. At ~ 10 at% Si the coating nanocomposite structure yielded the maximum hardness, 41 ± 3 GPa. Tribological performance showed a proportional relationship with $\text{Ti}_{0.903}\text{Si}_{0.097}\text{N}$ demonstrating superior wear resistance compared to TiN. The nanocomposite $\text{TiN/a-Si}_3\text{N}_4$ provides enhanced oxidation resistance as Si_3N_4 partially encapsulates TiN and acts as a

barrier to oxygen diffusion even at elevated temperature (700°C) in air. Simultaneously, passivating silica hinders crystal growth and preserves the nanocomposite microstructure. Further work is required to establish whether the TiN crystallites are completely encapsulated by α -Si₃N₄ intergranular films.

References:

- [1] A. D. Pogrebnyak, A. P. Shpak, N. A. Azarenkov and V. M. Beresnev, *Physics-USpekhi*, **2009**, 52, 29-54.
- [2] S. Vepřek and S. Reiprich, *Thin Solid Films*, **1995**, 268, 64-71.
- [3] J. Musil and H. Hrubý, *Thin Solid Films*, **2000**, 365, 104-109.
- [4] J. Musil and J. Vlček, *Surf. Coat. Technol.*, **2001**, 142–144, 557-566.
- [5] M. Stüber, H. Leiste, S. Ulrich, H. Holleck and D. Schild, *Surf. Coat. Technol.*, **2002**, 150, 218-226.
- [6] J. Musil, P. Baroch, J. Vlček, K. H. Nam and J. G. Han, *Thin Solid Films*, **2005**, 475, 208-218.
- [7] S. Sambasivan and W. Petuskey, *J. Mater. Res.*, **1994**, 9, 2362-2369.
- [8] P. Walsh, A. Omeltchenko, R. K. Kalia, A. Nakano, P. Vashishta and S. Saini, *Appl. Phys. Lett.*, **2003**, 82, 118-120.
- [9] E. Török, A. Perry, L. Chollet and W. Sproul, *Thin Solid Films*, **1987**, 153, 37-43.
- [10] D. S. Stone, K. B. Yoder and W. D. Sproul, *J. Vac. Sci. Technol., A*, **1991**, 9, 2543-2547.
- [11] M. E. O'Hern, R. H. Parrish and W. C. Oliver, *Thin Solid Films*, **1989**, 181, 357-363.
- [12] J. Musil, *Surf. Coat. Technol.*, **2012**, 207, 50-65.
- [13] F. Vaz, L. Rebouta, P. Goudeau, T. Girardeau, J. Pacaud, J. P. Rivière and A. Traverse, *Surf. Coat. Technol.*, **2001**, 146–147, 274-279.
- [14] K. Sarakinos, J. Alami and S. Konstantinidis, *Surf. Coat. Technol.*, **2010**, 204, 1661-1684.

- [15] J. Alami, K. Sarakinos, G. Mark and M. Wuttig, *Appl. Phys. Lett.*, **2006**, 89, 154104.
- [16] G. Pawley, *J. Appl. Crystallogr.*, **1981**, 14, 357-361.
- [17] S. Zhang, X. L. Bui, J. Jiang and X. Li, *Surf. Coat. Technol.*, **2005**, 198, 206-211.
- [18] W. C. Oliver and G. M. Pharr, *J. Mater. Res.*, **1992**, 7, 1564-1583.
- [19] J. Pelleg, L. Z. Zevin, S. Lungo and N. Croitoru, *Thin Solid Films*, **1991**, 197, 117-128.
- [20] S. Veprek, *Journal of Nanoscience and Nanotechnology*, **2011**, 11, 14-35.
- [21] R. F. Zhang and S. Veprek, *Materials Science and Engineering: A*, **2006**, 424, 128-137.
- [22] A. Flink, M. Beckers, J. Sjöln, T. Larsson, S. Braun, L. Karlsson and L. Hultman, *J. Mater. Res.*, **2009**, 24, 2483-2498.
- [23] J. Patscheider, T. Zehnder and M. Diserens, *Surf. Coat. Technol.*, **2001**, 146, 201-208.
- [24] A. Bendavid, P. J. Martin, J. Cairney, M. Hoffman and A. C. Fischer-Cripps, *Appl. Phys. A*, **2005**, 81, 151-158.
- [25] C. Iwamoto and S. i. Tanaka, *J. Am. Ceram. Soc.*, **1998**, 81, 363-368.
- [26] S. Hao, B. Delley and C. Stampfl, *Physical Review B*, **2006**, 74, 035402.
- [27] A. S. Argon and S. Yip, *Philos. Mag. Lett.*, **2006**, 86, 713-720.
- [28] S. Yip, *Nat Mater*, **2004**, 3, 11-12.
- [29] R. W. Siegel and G. E. Fougere, *Nanostruct. Mater.*, **1995**, 6, 205-216.
- [30] S. Veprek, R. F. Zhang, M. G. J. Veprek-Heijman, S. H. Sheng and A. S. Argon, *Surf. Coat. Technol.*, **2010**, 204, 1898-1906.
- [31] R. Zhang, A. Argon and S. Veprek, *Phys. Rev. Lett.*, **2009**, 102, 015503.
- [32] S. Vepřek, S. Reiprich and L. Shizhi, *Appl. Phys. Lett.*, **1995**, 66, 2640-2642.
- [33] S. H. Kim, J. W. Jang, S. S. Kang and K. H. Kim, *J. Mater. Process. Technol.*, **2002**, 130, 283-288.

- [34] A. Leyland and A. Matthews, *Wear*, **2000**, 246, 1-11.
- [35] M. Diserens, J. Patscheider and F. Lévy, *Surf. Coat. Technol.*, **1999**, 120–121, 158-165.

Chapter 7

Conclusions and future work

The outcomes of this thesis are summarized and discussed together with a strategy to complete examinations of the three studied hard coating systems. For the TiN/Ti_xAl_{1-x}N and yttrium-incorporated Ti_{1-x-y}Al_xY_yN multilayer architectures, further characterization of layer interfaces, toughness, high-temperature wear resistance and oxidation degradation are required. For the Ti-Si-N nanocrystalline/amorphous composite system, processing enhancement will be necessary to fabricate hard Si₃N₄ at grain boundaries. Nonetheless, the outcomes demonstrate the potential to accelerate the development of protective coatings for industry by tailoring chemical and topological designs through systematic configuration of processing techniques that deliver enhanced performance.

7.1 Conclusions and discussion

In this thesis, three TiN-based hard coating systems were explored from the standpoint of nanostructure and chemical modulation. In every case, materials were deposited by physical vapor deposition (PVD) techniques with functionality tuned by systematic modification of the principle processing parameters. A performance matrix was constructed by comprehensive structure and property characterization that was correlated with the processing methods.

7.1.1 TiN/Ti_xAl_{1-x}N multilayer coatings

Multilayer TiN/Ti_xAl_{1-x}N coatings were deposited by cathodic arc deposition (CAD) where the layer period (Λ) was the principle processing parameter responsible for structure and property evolution. For $7 \text{ nm} \leq \Lambda \leq 45 \text{ nm}$, Λ varied inversely with substrate rotation speed. The coatings showed $\langle 111 \rangle$ textured columnar grains and no secondary phases or voids in the grain boundaries. As Λ decreased a superlattice appeared in tandem with a more pronounced texture. Simultaneously, the hardness first increased before deteriorating, reaching a maximum at $\Lambda = 13 \text{ nm}$, while the best wear resistance was shown for $\Lambda = 7 \text{ nm}$. The maximum hardness ($\sim 38 \text{ GPa}$) is superior to both bulk TiN and Ti_xAl_{1-x}N coatings. The major outcome of these experiments was defining the correlation between Λ , substrate rotation speed and the superior hardness for an optimized superlattice period Λ .

The TiN/Ti_xAl_{1-x}N coatings show that superlattices enhance hardness but this phenomenon is complex with several factors in play. Proposed models [1-4] include an image effect arising from shear modulus differences and coherency strain from misfit lattice parameters. For example, it was reported that V_{0.6}Nb_{0.4}N/NbN with similar shear modulus and 3.5% lattice mismatch did not show improved hardness [5]. The lattice parameter mismatch shown in Chapter

4 between TiN and $Ti_xAl_{1-x}N$ is only 2% indicating the coherency strain effect is minor. In this instance, the coating hardness enhancement is ascribed to the image effect. However, direct shear modulus values of TiN and $Ti_xAl_{1-x}N$ individual coatings are unavailable to support the image effect model. It was found the hardness peaked at $\Lambda = 13$ nm, implying the existence of two contradictory effects as Λ varies. These observations are in agreement with the model of Chu and Barnett [1] who found the greatest hardness appears at a certain Λ , because dislocations can easily migrate within layers at large Λ (~ 100 nm) and across layers at small Λ (~ 1 to 10 nm). Energy dispersive X-ray analysis (EDX) revealed that as Λ decreased, the interface width ratio to Λ was lower, and chemical contrast was coarser. Consequently, hardness is inferior for low contrast interfaces as dislocations easily cross interfaces. At large Λ dislocation movement within layers prevails and hardness degrades. Further study of these phenomena as a confirmation of the Chu and Barnett model to correlate hardness and structure is required.

The multilayer coating better resisted wear as Λ decreased, but H/E ratio was not primarily responsible [6]. More probably, the greater interface frequency contributes to crack energy scattering and friction crack extension parallel to the surface, rather than direct penetration inside substrate. It remains to be demonstrated if better tribological performance will be maintained at elevated temperatures.

7.1.2 Yttrium incorporated TiN/ $Ti_xAl_{1-x}N$ multilayer coatings

In Chapter 5, a hybrid PVD technique of magnetron sputtering (MS) and cathodic arc deposition (CAD) was employed to deposit Ti-Al-Y-N multilayer coatings. Yttrium was incorporated from a pure Y target. Two processing parameters, substrate holder rotation speed and Y target power, influence coating structure, chemical composition and performance. First, by maintaining

a substrate rotation speed of 5 revolutions per minute (r.p.m) and increasing Y target power, the overall Y content increased from 0 to 2.4 at% accompanied by smaller crystal size, higher-angle grain boundaries and the appearance of <200> texture. Simultaneously, coating hardness was enhanced by 41% from ~29 GPa to ~ 41 GPa while Young's modulus was unchanged. Yttrium incorporation improved oxidation resistance without compromising the adhesion and wear resistance. The second processing parameter, substrate rotation speed while Y content = 2.4 at%, allowed Λ to increase from 5.5 nm to 24 nm when 5 r.p.m decreased to 1 r.p.m. The texture transferred from <111> to <200> and grain morphology also changed from acicular to equiaxed grains with visible Y layers. The hardness and Young's modulus decreased substantially with increasing Λ .

The TiN/Ti_xAl_{1-x}N coatings deposited at 5 r.p.m showed superlattice features. Incorporating an Y metal target into the deposition system improved hardness while the residual stress peaked at 1.2 at% Y, due to several factors including residual stress originating from ion bombardment during deposition [7, 8], a solid solution hardening effect [9] and a grain size effect [10]. For example, in the coating with 2.4 at% Y the hardness was enhanced not only by residual strain compared to 1.2 at% Y coatings, but the smaller grain size according to the Hall-Petch effect [11] as observed by transmission electron microscopy (TEM). These smaller acicular grains are possibly induced by a secondary phase. However, solid solution hardening could not be confirmed even though atomic scale chemical mixing was observed by X-ray diffraction (XRD). Increasing the substrate rotation speed from 1 r.p.m to 5 r.p.m results in an Y redistribution. For smaller periods, grains penetrate the layer interfaces and become acicular with coherent layer interfaces and grain boundaries. Therefore, dislocations do not easily cross interfaces or grain boundaries leading to enhanced hardness.

The Y content effect on adhesion and wear resistance was demonstrated. Incorporating 1.2 at% Y lowers both adhesion and wear resistance due to the high residual strain. In fact, adding 2.4 at% Y increased coating toughness compared to the 1.2 at% Y, but the toughness could not be readily quantified. Further, Y additions change the oxidation mechanism at elevated temperatures. To explain the composition of the oxidized sample composition two mechanisms were postulated. First, poorer inward diffusion of oxygen as Y segregates to grain boundary blocked diffusion pathways, and second, the oxidation process is retarded as Y occupies the vacancies that stabilize the oxide. These reported phenomena [12-14] could not be directly validated. In conclusion, the coating deposited at 5 r.p.m with 2.4 at% Y is the best option among those tested for high speed machining applications.

7.1.3 Nanocomposite Ti-Si-N coatings

The Ti-Si-N nanocomposite was tailored by varying silicon content. The first outcome is that the incorporated Si could be controlled by adjusting the power on the Si target. Meanwhile, the microstructure changed with Si content as shown by XRD in Chapter 6. When Si increased from 0 to 10 at% the texture transferred from $\langle 111 \rangle$ to $\langle 200 \rangle$, but for Si > 10 at% the $\langle 200 \rangle$ texture was removed. This change in texture was accompanied by the reduction of crystal size and an improvement in hardness and Young's modulus increasing to ~ 10 at% Si, beyond which the properties degraded. Moreover, oxidation resistance and hardness at elevated temperatures are enhanced by Si addition.

According to calculations [15, 16], a nanocomposite consisting of randomly oriented 3-4 nm TiN crystallites encapsulated by 1-2 monolayers of amorphous (a-) Si_3N_4 should enhance hardness by a factor of 4 to 5. In this thesis, Ti-Si-N hardness doubled when Si content was ~ 10 at%, which was far below the prediction. It was found that $\text{Ti}_{0.9}\text{Si}_{0.1}\text{N}$ gave the highest hardness (~ 41 GPa)

and consisted of columnar grains with $\langle 200 \rangle$ textures. As the size of the textured crystals was around 10 nm, the desired nanocomposite structure with randomly oriented nanocrystallites and hard interfaces was not generated. In this instance, the hardness was probably enhanced only due to the nanosize effect [17], that inhibits dislocation generation and/or motion due to the higher grain boundary frequency. However, without hard interfaces the predicted hardness was not achieved. A contributing factor to the non-ideal nanocomposite will be the presence of impurity oxygen that hinders crystalline and amorphous phase segregation, but preferentially stabilizes a Ti-Si-N solid solution in column grains, that degrades mechanical properties [18, 19]. This could be clarified using electron energy loss spectroscopy (EELS) to detect oxygen and X-ray photoelectron spectroscopy (XPS) to detect local bonding states. A deeper understanding of the role of oxygen may guide further modification of deposition parameters to restrict oxygen ingress. Alternatively, improper deposition parameters may have been selected. It is supposed that the addition of Si causes the nanocomposite structure via self-organized spinodal decomposition that is favoured by higher N_2 pressure or temperature. Thus the columnar grains deposited by PVD might be a consequence of low deposition temperature, high bias voltage, or inadequate N_2 flow limiting the kinetic diffusion required for phase segregation.

TEM observations show that adding 10 at% Si to the Ti-Si-N coating maintains the column grain morphology, but removes long range crystal order to some extent. Therefore, comprehensive mapping of the Si distribution could reveal coating process shortcomings, and be critical to the further definition of structure and processing correlation. According to the nanocomposite model Si should be uniformly distributed around the nanocrystallites (Figure 7.1). Aberration corrected TEM accompanied by simulation would allow quantitative atomic scale analysis to better describe the atomic arrangement of interfaces.

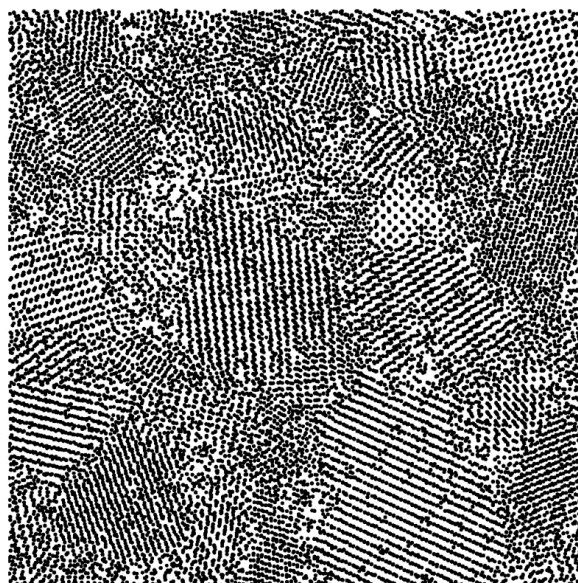


Figure 7.1 The thermodynamically preferred structure of $\text{Ti}_{43}\text{Si}_7\text{N}_{50}$ ($13.7 \times 13.7 \text{ nm} \times 1 \text{ nm}$ slice) based on molecular dynamics simulations, showing crystallites in same size range but various orientations.*

It is apparent that higher Si contents create coatings that are harder and more resistant to oxidation. A reasonable explanation would be that the accumulation of Si at grain boundaries acts as a barrier to inward oxygen diffusion. It was reported that crystalline coatings exhibit a lower oxidation resistance, compared to X-ray amorphous coatings, as grain boundaries in crystalline materials provide fast diffusion pathways from the atmosphere to the substrate/coating interfaces [20]. In this thesis, while the correlation between oxidation resistance and Si content was established further structural information is required to fully validate this supposition. To this end, the Si distribution within the as-deposited sample and the structural alteration promoted at elevated temperature require further study.

* Reprinted from Surface and Coatings Technology, Vol 203, J. Houska, J.E. Klemberg-Sapieha, L. Martinu, Atomistic simulations of the characteristics of TiSiN nanocomposites of various compositions, Pages No. 3352., Copyright (2016), with permission from Elsevier.

7.2 Future work

Additional experiments and simulations are required to confirm and design hard multilayer coating systems:

1. For multilayer TiN/Ti_xAl_{1-x}N coatings:
 - a. Elastic modulus measurements of TiN and Ti_xAl_{1-x}N individual coatings would demonstrate if the superlattice hardening is a consequence of shear modulus differences;
 - b. Dislocation density evaluation and comparisons inside each layer by weak-beam dark field transmission electron microscopy (DFTEM) [21] could confirm that as Λ decreases there are fewer dislocations generated inside each layer;
 - c. Ball-on-disc tribology tests on coatings at elevated temperature (above 600 °C) would validate coating wear resistance under conditions closer to industrial applications.
 - d. Aberration corrected TEM coupled with EDX could be adopted to analyze the micro-chemical compositions of layers to clarify the composition modulation influences on coating properties.
2. For Y incorporated in TiN/Ti_xAl_{1-x}N multilayer coatings:
 - a. Solid solution formation could be validated through investigation of the local bonding of Y established by X-ray photoelectron spectroscopy (XPS).
 - b. Experimental methods could be designed to quantify the coating toughness improved by Y incorporation, e.g. scratch test [22].
 - c. Oxidation mechanisms could be differentiated by thermal gravimetric analysis (TGA), and the oxidized samples, especially Y distribution could be studied by scanning electron microscopy (SEM), electron probe micro-analyzer or TEM. Yttrium oxidation state could be confirmed by XPS, corresponding to XRD results.

- d. Examination of coating performance and structure could be extended by increasing Y content beyond 2.4 at% and examining properties modification.

The poor mechanical performance of the Ti-Si-N nanocomposite compared to modeling means further modification of the coating processing is required, coupled with further characterization of existing samples to reveal process shortcomings. The entry point is the Si distribution in crystallites and grain boundaries, which can be realized by aberration corrected TEM. This requires very thin sections to avoid grain overlap, which could be realized by nanomilling of Ti-Si-N laminars. In addition to TEM, pulsed laser atom probe tomography (PLAPT) would allow construction of 3-dimensional compositional maps, even for less conductive materials, at resolutions close to atomic scale. This technique has already been employed for discerning Ti-Si-N grains by highlighting the Ti associated iso-density areas [23].

It is possible that a solid solution can be generated due to incomplete phase segregation that is stabilized by impurities. A commonly applied approach to drive phase segregation is to increase the deposition temperature or N_2 pressure but this is uneconomic and limits the coating application range (as high speed steel softens above $550^\circ C$). Otherwise, unambiguous detection of discrete amorphous Si_3N_4 at grain boundaries is required. Light element detection using electron energy loss spectroscopy (EELS) could clarify if carbon and oxygen “trap” Si within crystals, and so direct effort towards fabricating purer coatings. In turn, chemically pure coatings could decrease the deposition temperature.

Another possible variant in Ti-Si-N coatings is where TiN:Si two-phase crystallites are separated by SiN_x defect clusters. Such an outcome could be linked to plasma properties defined by the relative target and substrate positions

or the Si target power configuration. In this case, parameters could be modified to avoid this microchemistry.

7.3 Implications and outstanding questions

This work focused on superlattice hardening and nanocrystalline/amorphous composite hardening to design TiN-based coating systems and deposit them by controlling a range of processing parameters. Comprehensive characterization revealed coating structures were correlated with processing parameters and mechanical properties, as a precursor to reproducible industrial production. Yttrium addition is a promising and efficient option to enhance hardness and toughness simultaneously. Therefore, a key outcome of this work is deploying comprehensive correlation of processing and performance as basis to develop novel hard coating systems and PVD processes. The extensive structural characterization of large-scale coatings provides confidence that the evaluations are of practical relevance. Moreover, the integrated performance tests under high temperature, high speed friction and plastic deformation, suggest the designed system may be viable for high speed industrial machining. However, the mechanisms by which processing variants deliver structural and performance modification requires further simulation and experimental work. The goal would be to create a process to deposit super ($80 \text{ GPa} \geq H \geq 40 \text{ GPa}$), or even ultra-hard ($H \geq 80 \text{ GPa}$) coatings, especially Ti-Si-N nanocomposites consisting of nanocrystallites and hard grain interfaces. There is much room for improvement as the best performing materials produced in these studies delivered $H \sim 41 \text{ GPa}$ for $\text{Ti}_{0.903}\text{Si}_{0.097}\text{N}$.

References:

- [1] X. Chu and S. A. Barnett, *J. Appl. Phys.*, **1995**, 77, 4403-4411.
- [2] J. Koehler, *Physical review B*, **1970**, 2, 547.
- [3] P. Anderson and C. Li, *Nanostruct. Mater.*, **1995**, 5, 349-362.

- [4] M. Kato, T. Mori and L. H. Schwartz, *Acta Metall.*, **1980**, 28, 285-290.
- [5] M. Shinn and S. Barnett, *Appl. Phys. Lett.*, **1994**, 64, 61-63.
- [6] A. Leyland and A. Matthews, *Wear*, **2000**, 246, 1-11.
- [7] J. Musil, S. Kadlec, J. Vyskočil and V. Valvoda, *Thin Solid Films*, **1988**, 167, 107-120.
- [8] W. Herr and E. Broszeit, *Surf. Coat. Technol.*, **1997**, 97, 335-340.
- [9] O. Knotek, M. Böhmer and T. Leyendecker, *J. Vac. Sci. Technol., A*, **1986**, 4, 2695-2700.
- [10] N. Dubrovinskaia, V. L. Solozhenko, N. Miyajima, V. Dmitriev, O. O. Kurakevych and L. Dubrovinsky, *Appl. Phys. Lett.*, **2007**, 90, 101912.
- [11] Y. H. Yoo, D. P. Le, J. G. Kim, S. K. Kim and P. Van Vinh, *Thin Solid Films*, **2008**, 516, 3544-3548.
- [12] F. Rovere, P. Mayrhofer, A. Reinholdt, J. Mayer and J. Schneider, *Surf. Coat. Technol.*, **2008**, 202, 5870-5875.
- [13] L. Zhu, Y. Zhang, W. Ni and Y. Liu, *Surf. Coat. Technol.*, **2013**, 214, 53-58.
- [14] L. Donohue, D. Lewis, W. Münz, M. Stack, S. Lyon, H. Wang and D. Rafaja, *Vacuum*, **1999**, 55, 109-114.
- [15] R. F. Zhang, A. S. Argon and S. Veprek, *Phys. Rev. Lett.*, **2009**, 102, 015503.
- [16] S. Veprek, R. F. Zhang, M. G. J. Veprek-Heijman, S. H. Sheng and A. S. Argon, *Surf. Coat. Technol.*, **2010**, 204, 1898-1906.
- [17] S. Yip, *Nature*, **1998**, 391, 532-533.
- [18] S. Veprek and M. G. J. Veprek-Heijman, *Thin Solid Films*, **2012**, 522, 274-282.
- [19] S. Veprek, *Journal of nanoscience and nanotechnology*, **2011**, 11, 14-35.
- [20] J. Musil, *Surf. Coat. Technol.*, **2012**, 207, 50-65.
- [21] L. Hultman, G. Håkansson, U. Wahlström, J.-E. Sundgren, I. Petrov, F. Adibi and J. Greene, *Thin Solid Films*, **1991**, 205, 153-164.

- [22] S. Zhang, D. Sun, Y. Fu and H. Du, *Surf. Coat. Technol.*, **2005**, 198, 74-84.
- [23] F. Tang, B. Gault, S. P. Ringer, P. Martin, A. Bendavid and J. M. Cairney, *Scripta Mater.*, **2010**, 63, 192-195.

List of Publications

1. **Wang, J.**; Wei, F.; Lim, S. M.; Liu, E.; Guet, C.; White, T.; Dong, Z., Synthesis and Crystal Structure Characterization of Oxysilicate Apatites for Stabilization of Sr and Rare-Earth Elements. *Journal of the American Ceramic Society* 2016, 99 (5), 1761-1768.
2. Gaw, S. L.; **Wang, J.**; Sun, S.; Dong, Z.; Reches, M.; Lee, P. S.; Xu, Z. J., Electrochemical Cycling Induced Surface Segregation of AuPt Nanoparticles in HClO₄ and H₂SO₄. *Journal of The Electrochemical Society* 2016, 163 (7), F752-F760.
3. Fan, Z.; Xiao, J.; **Wang, J.**; Zhang, L.; Deng, J.; Liu, Z.; Dong, Z.; Wang, J.; Chen, J., Ferroelectricity and ferroelectric resistive switching in sputtered Hf_{0.5}Zr_{0.5}O₂ thin films. *Applied Physics Letters* 2016, 108 (23), 232905.
4. Fan, Z.; Deng, J.; **Wang, J.**; Liu, Z.; Yang, P.; Xiao, J.; Yan, X.; Dong, Z.; Wang, J.; Chen, J., Ferroelectricity emerging in strained (111)-textured ZrO₂ thin films. *Applied Physics Letters* 2016, 108 (1), 012906.
5. Bulanov, E. N.; **Wang, J.**; Knyazev, A. V.; White, T.; Manyakina, M. E.; Baikie, T.; Lapshin, A. N.; Dong, Z., Structure and Thermal Expansion of Calcium–Thorium Apatite, [Ca₄]F[Ca₂Th₄]T[(SiO₄)₆]O₂. *Inorganic Chemistry* 2015, 54 (23), 11356-11361.
6. Arab Pour Yazdi, M.; Lomello, F.; **Wang, J.**; Sanchette, F.; Dong, Z.; White, T.; Wouters, Y.; Schuster, F.; Billard, A., Properties of TiSiN coatings deposited by hybrid HiPIMS and pulsed-DC magnetron co-sputtering. *Vacuum* 2014, 109, 43-51.
7. Liu, X.; Sorescu, M.; **Wang, J.**; Schoenthal, W.; Dong, Z.; Ramanujan, R. V.; Laughlin, D. E.; McHenry, M. E., Structural and Magnetic Properties of xFe₂TiO₄(1-x)Fe₃O₄(0.75<x<1). *IEEE Transactions on Magnetics* 2014, 50 (11), 1-4.
8. Lu, F.; Yao, T.; Xu, J.; **Wang, J.**; Scott, S.; Dong, Z.; Ewing, R. C.; Lian, J., Facile low temperature solid state synthesis of iodoapatite by high-energy ball milling. *RSC Advances* 2014, 4 (73), 38718-38725.
9. Lu, X.; Utama, M. I. B.; Lin, J.; Gong, X.; Zhang, J.; Zhao, Y.; Pantelides, S. T.; **Wang, J.**; Dong, Z.; Liu, Z.; Zhou, W.; Xiong, Q., Large-Area Synthesis of Monolayer and Few-Layer MoSe₂ Films on SiO₂ Substrates. *Nano Letters* 2014, 14 (5), 2419-2425.
10. **Wang, J.**; Arab Pour Yazdi, M.; Lomello, F.; Billard, A.; Kovács, A.; Schuster, F.; Guet C.; White T. J.; Sanchette F., Microstructure influences on mechanical properties and tribology behaviors of TiN/Ti_xAl_{1-x}N multilayer coatings. *Surface and Coatings Technology* 2016, **Accepted: SURFCOAT-D-16-02119.**

Conference:

- 8th International Conference on Technological Advances of Thin Films & Surface Coatings, 12nd -15th July 2016, Singapore,

Poster Presentation: Microstructure and properties of cathodic arc deposited TiN/Ti_xAl_{1-x}N multilayer coatings. **J. Wang**, M. Arab Pour Yazdi, F. Lomello, F. Sanchette, T. White, F. Schuster, A. Billard, Z. Dong.

- 42nd International Conference on Metallurgical Coatings and Thin Films, 20th-24th April 2015, San Diego, US,

Poster Presentation: Mechanical Properties of Nanolayered TiN/TiAlN Coatings Processed by Cathodic Arc Deposition. **J. Wang**, M. Arab Pour Yazdi, F. Lomello, F. Sanchette, Z. Dong, T. White, C. Pascal, Y. Wouters, F. Schuster, A. Billard

- 41st International Conference on Metallurgical Coatings and Thin Films, 28th Apr-2nd May 2014, San Diego, US,

Poster Presentation: nc-TiN/a-SiN_x thin films prepared by means of High-Power Impulse and Pulsed-DC Magnetron co-Sputtering. M. Arab Pour Yazdi, F. Lomello, **J. Wang**, F. Sanchette, Z. Dong, T. White, Y. Wouters, F. Schuster, A. Billard